PROMPT GAMMA ANALYSIS OF HYDROGEN, CARBON, OXYGEN AND NITROGEN IN BULK SAMPLES

BY

FARIS AHMED AL-MATOUQ

A Thesis Presented to the
DEANSHIP OF GRADUATE STUDIES

KING FAHD UNIVERSITY OF PETROLEUM & MINERALS
DHAHRAN, SAUDI ARABIA

In Partial Fulfillment of the
Requirements for the Degree of

MASTER OF SCIENCE

In

PHYSICS

December 2013

KING FAHD UNIVERSITY OF PETROLEUM & MINERALS
DHAHRAN- 31261, SAUDI ARABIA

DEANSHIP OF GRADUATE STUDIES

This thesis, written by **FARIS AHMED ALMATOUQ** under the direction his thesis advisor and approved by his thesis committee, has been presented and accepted by the Dean of Graduate Studies, in partial fulfillment of the requirements for the degree of **MASTER OF SCIENCE IN PHYSICS.**

Prof. Akhtar.A.Naqvi
(Advisor)

Dr. Abdulaziz Al-Jalal
Department Chairman

FZ Khiari

Dr. Fatah Z. Khiari
(Member)

Dr. Salam A. Zummo
Dean of Graduate Studies

Dr. Ayman S. El-Said
(Member)

6/1/14

Date

Dedication

Dedicated with love to my parents and to my best friend *H.S.*

ACKNOWLEDGMENTS

All thanks and praise is to almighty ALLAH, the source of every success, who gave me patience and strength to accomplish this work.

My utmost appreciation and gratitude goes to my adviser Prof. Akhtar A. Naqvi for his fatherhood continuous guidance and endless motivation and endless encouragement from the beginning of my project until the final stages. I consider myself fortunate to have been his student.

I am grateful to my committee member Dr. Fatah Z. Khiari for his kindness in reviewing my thesis and for his guidance and cooperation during this work. I consider myself very privileged for that.

Also, I am thankful to my committee member Dr. Ayman S. El-Said for providing me with his invaluable comments and support. I am also thankful to the Physics Department Chairman, Dr. Abdulaziz Al-Jalal, and other faculty members for their support. Acknowledgment is also owed to King Fahd University of Petroleum & minerals for supporting this work.

My genuine special thanks to my family, my father the continuous source of inspiration and encouragement, my mother the endless source of love and faithful prayers and to my brilliant brothers and sisters.

Lastly, but not the least, very special thanks are due to my source of cheerfulness, optimism and enthusiasm, my best friend Hassan Sharrofna for his persistent efforts and continuous encouragement during the past years until now.

TABLE OF CONTENTS

LIST OF TABLES

LIST OF FIGURES

LIST OF ABBREVIATIONS

PGNAA : Prompt Gamma-ray Neutron Activation Analysis

NIS : Neutron Inelastic Scattering

TNC : Thermal Neutron Capture

ABSTRACT

Full Name : [Faris Ahmed AL-Matouq]

Thesis Title : [Prompt Gamma Analysis of Hydrogen, Carbon, Oxygen and Nitrogen in Bulk Samples]

Major Field : [Physics]

Date of Degree : [December 2013]

In this study, a PGNAA setup was developed using KFUPM 350 keV accelerator to detect H, C and O via inelastic scattering of neutrons in bulk samples of proxy materials of explosives and narcotics. Due to the interference of oxygen prompt gamma rays in NIS, nitrogen concentration was measured in bulk samples through Thermal Neutron Capture (TNC) using 350 keV accelerator-based PGNAA setup, as well as MP320 portable neutron generator-based PGNAA setup. Monte Carlo simulations were carried out to calculate optimum geometry of the setups including experimental geometry, moderator size and detector as well as accelerator shielding.

For prompt gamma rays detection, lanthanum halide ($LaBr_3$:Ce or $LaCl_3$:Ce) and BGO detectors were tested for gamma ray detection. Best performance was observed for the $LaBr_3$: Ce detector. While the $LaCl_3$:Ce detector response was sensitive to neutron moderation effects in bulk sample. This enhanced chlorine prompt gamma ray background from $LaCl_3$:Ce detector for sample with increasing hydrogen contents. Due to the interference of prompt gamma ray from chlorine in $LaCl_3$:Ce detector and oxygen in bulk sample, $LaCl_3$:Ce detector is not suitable for oxygen determination from bulk hydrogenous samples.

Finally, the PGNAA setups were tested by determining C, O, N, and H concentrations in proxy material samples for explosives and narcotics using $LaBr_3$:Ce detector. Excellent agreement was observed in experimental results and results of the Monte Carlo simulations.

ملخص الرسالة

الاسم: فارس أحمد المعتوق

عنوان الرسالة: استخدام أشعة غاما الفورية لدراسة محتوى الهيدروجين و الكربون والأكسجين في العينات الكبيرة

التخصص: فيزياء

تاريخ الدرجة العلمية: ديسمبر ٢٠١٣

في هذه الدراسة، تم تطوير استخدام أشعة غاما الناتجة من تحفيز النيوترونات لرصد الهيدروجين والكربون والأكسجين عن طريق الاستطارة اللامرنة للنيوترونات من العينات الشبيهة بالمواد المتفجرة والمخدرات. ونظرا لتداخل أشعة غاما الفورية من الأكسجين بتلك التي من النيتروجين باستخدام الاستطارة اللامرنة للنيوترونات، فقد تم قياس نسبة النيتروجين في العينات عن طريق اصطياد النيوترونات الحرارية باستخدام المسارع وباستخدام مولّد النيوترونات المحمول. وقد تم استخدام طريقة "مونتي كارلو" للمحاكاة لحساب الأبعاد المُثلى للعينات ولكاشف أشعة غاما.

تم اختبار ثلاثة أنواع على حِدة من كواشف أشعة غاما؛ "لنثانوم بروমايد" و "لنثانوم كلورايد" و "بزموث جرمانيت"، وقد لوحظ أن أفضل أداء لكواشف أشعة غاما التي استخدمت في هذه الدراسة كان أداء الكاشف "لنثانوم برومايد"، فقد كان أداء "لنثانوم كلورايد" متأثرا بنسب الهيدروجين الموجودة في العينات حيث كلما زادت نسبة الهيدروجين في العينة كلما زادت أشعة غاما الفورية الناتجة من الكلورين الموجود في الكاشف التي بدورها تتداخل مع أشعة غاما الفورية الناتجة من الأكسجين في العينات، لذا لم يكن الكاشف "لنثانوم كلورايد" مناسباً لهذه الدراسة.

وأخيرا، تم اختبار الطريقة لتحديد نسب الهيدروجين والنيتروجين والكربون والأكسجين من العينات الشبيهة بالمواد المتفجرة والمخدرات، وقد توافقت النتائج المخبرية مع النتائج النظرية المحسوبة بطريقة "مونتي كارلو" للمحاكاة.

CHAPTER 1

INTRODUCTION

Elemental analysis of materials has a broad range of applications, from quality control tasks in mining and manufacturing industries [1, 2] to content monitoring of cargo containers for Homeland Security [3]. It is also used in building construction industries to monitor elemental concentrations in concrete [4, 5], and it is used in environmental and health sciences for monitoring water and soil contaminations. Several techniques have been developed for the elemental analysis of bulk samples [6-19]. Some of the important ones include nuclear (neutrons) techniques [7-12], X-ray and gamma ray techniques [14], micro-wave techniques [15, 16], Quadruple Resonance [17], and Dielectrometry [18]. X-ray and neutron techniques are commonly used to screen the luggage but X-ray technique has some serious limitations due to small absorption in, and incoherent scattering of x-rays from the low Z elements present in most explosives and illicit drugs. The other disadvantage of X-ray inspections is due to its reliance on shape recognition technique.

Prompt Gamma-Ray Neutron Activation Analysis (PGNAA) technique

Nuclear techniques, in particular **P**rompt **G**amma-Ray **N**eutron **A**ctivation **A**nalysis (PGNAA) technique, are non-destructive and rapid material characterization techniques [1-10]. Furthermore, these techniques are non-intrusive due to highly penetrating nature of neutrons and associated prompt gamma rays. In Prompt Gamma Ray Neutron Activation Analysis (PGNAA) technique, the material is irradiated with neutrons and prompt γ-rays are produced either through neutron inelastic scattering (n, n′γ) or thermal neutron capture (n_{th}, γ). The PGNAA technique based upon **N**eutron (N) **I**nelastic (I) **S**cattering (S) is called **NIS** technique while that based upon **T**hermal (T) **N**eutron (N) **C**apture (C) is called **TNC** technique. The elemental concentrations of the sample can then be determined from a measurement of the intensities of respective prompt γ-rays. Additionally, elemental concentrations are also measured using other neutron techniques such as fast neutron scattering [11, 12], and fast neutron absorption [9, 10] to detect explosives and narcotics through C, N and O measurements.

In the PGNAA technique, a material is typically irradiated with fast neutrons. Some of the fast neutrons are moderated in an external moderator. These neutrons interact with the material through neutron inelastic scattering (n, n′γ) or thermal neutron capture (n_{th},γ) to produce prompt γ-rays. The elemental concentrations in the sample can then be determined from the intensity of prompt γ-rays produced, either through neutron inelastic scattering (n, n′γ) or thermal neutron capture (n_{th},γ), or both. The interaction between neutron and sample is illustrated in Figure 1.1. Figure 1.2 shows prompt gamma rays energies due to inelastic scattering of neutrons from C, N and O elements. There are some advantages in choosing the prompt γ-rays produced by thermal neutron capture for elemental analysis because prompt γ-rays from neutron inelastic scattering can originate from several sources, such as beam line components and structural materials of the experimental setup, while the prompt γ-rays from the thermal capture are localized and mainly restricted to the space surrounded by the thermal neutron region. This localized region of the prompt γ-rays allows improving the shielding against the background γ-rays.

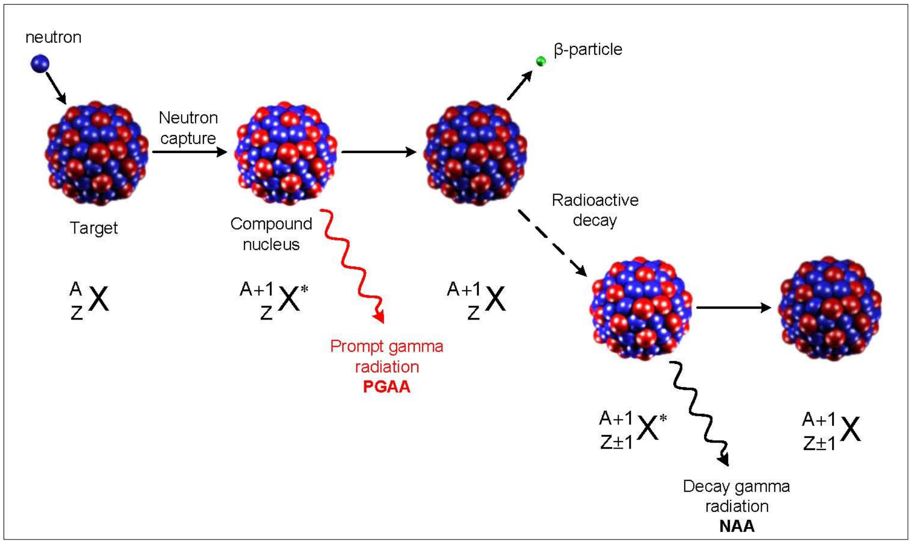

Figure 1.1 Schematic diagram demonstrating neutron capture process & the nuclear decay products [20]

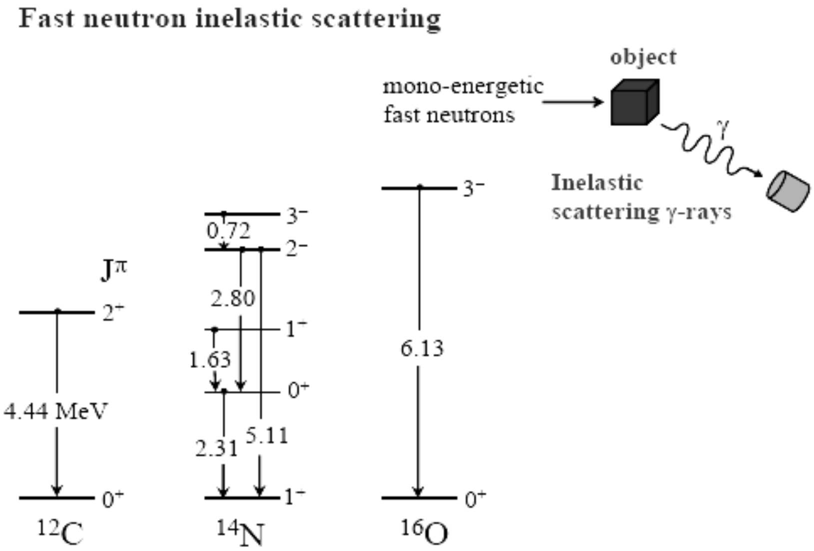

Figure 1.2 Gamma Ray decay scheme from inelastic scattering of neutrons from C, N and O

PGNAA Application in Contraband Detection

Particularly, N, C, H and O element concentration measurements can be used in cargo and luggage screening to check transport of explosive, narcotics and other contraband material concealed in transport containers across the borders [3, 6, 7]. As shown in Figure 1.3 [6] most of the explosives and illicit drugs contain H, C, N and O elements in different concentration than those in innocuous materials.

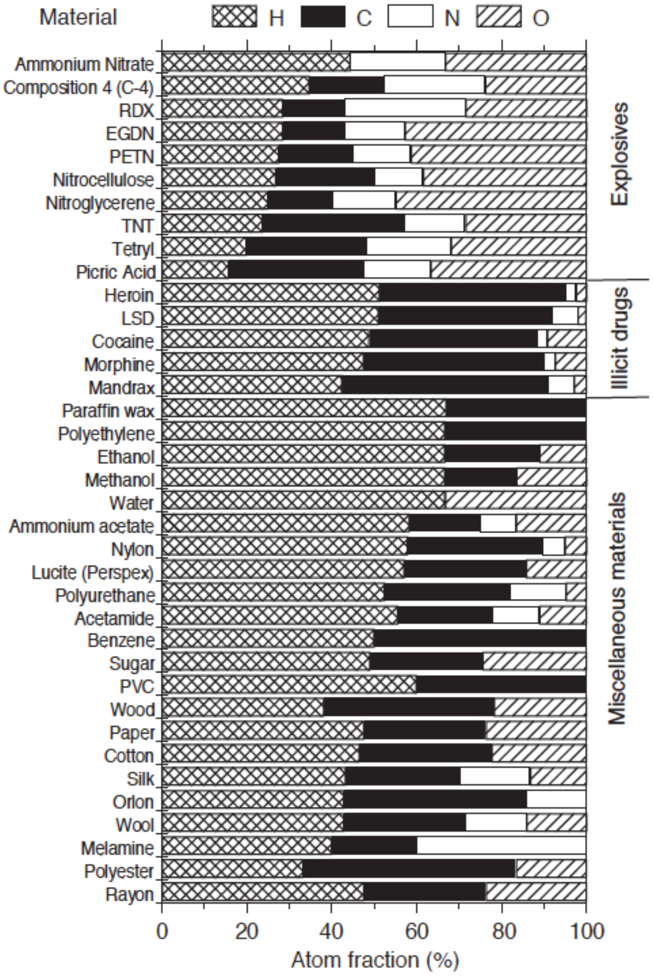

Figure 1.3 Bar chart showing the elemental concentrations in low Z materials [6]

Figure1.3 shows H, C, N and O elements concentrations in various materials. Explosives contain relatively high concentrations of oxygen and nitrogen and relatively low concentrations of carbon and hydrogen. On the other hand, illicit drugs have large concentrations of hydrogen and carbon and small concentrations of nitrogen and oxygen. Moreover, most of the explosives have densities that range from 1.2 to 2.0 g cm^{-3} which are generally larger than most of innocuous HCNO substances. These features can be used to differentiate contraband from innocuous materials concealed in cargo containers. Explosive can be molded or packed into any form and this makes their detection through shape recognition very difficult [14]. These difficulties have been overcome in neutron-based techniques.

The objective of this study is to design and test a T(d,n)- and a D(d,n)-reaction based PGNAA setups with an external moderator for measurement of C, N, O and H concentrations in low Z organic materials. Detection limits of the facility are obtained through prompt gamma analysis of C, O, N and H in the samples. Monte Carlo simulation are carried out in order to determine the optimum experimental geometry including sample size, moderator size, detector and accelerator shielding of the proposed setups. Finally theoretical yield of C, N, O and H prompt gamma rays are calculated from the sample specimens. The experimental results are compared with the theoretical results. The results of this study can be utilized to design a PGNAA setup to measure C, O, N and H concentrations in cargos for explosives and narcotics detection.

CHAPTER 2

DESIGN CALCULATIONS USING MCNP CODE

In this study, design of the PGNAA NIS- and TNC-based setups were obtained through Monte Carlo simulations. The MCNP code (**M**onte **C**arlo **N**-**P**articles code) is used to transport neutral particles. It can be used in several transport modes; neutron only, photon only, electron only or combined neutron/photon transport where neutron interactions produce photons. The code can be used to duplicate a statistical process such as the interaction of nuclear particles with materials. It is particularly useful for complex problems that cannot be modeled by computer codes that use deterministic methods. The individual probabilistic events that comprise a process are simulated sequentially. The probability distributions governing these events are statistically sampled to describe the entire process. In general, the simulation is performed on a digital computer since the number of trials necessary to effectively describe the phenomenon is usually quite large. The statistical sampling process is based on the selection of random numbers. Monte Carlo technique is preeminently realistic (a theoretical experiment). It consists of actually following each of many particles from a source throughout its life to its death in some terminal category (absorption, escape, etc.). Probability distributions are randomly sampled using transport data to determine the outcome at each step of its life [22]. During the transport process the code specifically transports the predetermined particles and reaction channels. Generally, neutrons and gamma rays are the common neutral particles to be transported in the design of low energy nuclear physics experiments. Common nuclear interactions encountered by the neutral particles in such experiments are: capture, elastic and inelastic scattering etc… In the following brief, descriptions of these processes relevant to MCNP code are given.

2.1 Neutron Interactions

A neutron can interact with the nucleus in many ways. It can be one of two main types, either scattering (including elastic and inelastic) or absorption. When a neutron is absorbed by a nucleus, several reaction channels are opened such as (n, γ), (n, f), (n, α) etc… The MCNP code with built-in theoretical basis takes care of the transport of the respective particle for the required reaction. The PGNAA setups design calculations of this study mainly needed elastic and inelastic scattering as well as capture processes of the particles.

Inelastic Scattering

The treatment of inelastic scattering depends upon the particular inelastic reaction chosen. Inelastic reactions are defined as (n, ***y***) reactions such as in which ***y*** includes at least one neutron. For many inelastic reactions, such as (n, 2n), more than one neutron can be emitted for each incident neutron. The weight of each exiting particle is always the same as the weight of the incident particle minus any implicit capture. Various scattering laws that are sampled independently from the cross-section files for each exiting particle govern the energy of exiting particles. Which law is used is prescribed by the particular cross-section evaluation used. In fact, more than one law can be specified, and the particular one used at a particular time is decided with a random number.

The exiting particle energy and direction in the target -at rest- (laboratory) coordinate system are related to the center of mass energy and direction as follows [22]:

$$E' = E'_{cm} + \left[\frac{E + 2\mu_{cm}(A+1)\sqrt{EE'_{cm}}}{(A+1)^2} \right] \text{, and } \mu_{lab} = \mu_{cm}\sqrt{\frac{E'_{cm}}{E'}} + \frac{1}{A+1}\sqrt{\frac{E}{E'}} \qquad (2.1)$$

Where:

E' = Exiting particle energy (laboratory)

E'_{cm} = Exiting particle energy (center of mass)

E= Incident particle energy (laboratory)

μ_{cm} = Cosine of center of mass scattering angle

μ_{lab} = Cosine of laboratory scattering angle

A = Atomic weight ratio (mass of nucleus divided by mass of incident particle.)

Neutron Capture

MCNP treats neutron capture in one of two ways: analog or implicit. Either way, the incident incoming neutron energy does not include the relative velocity of the target nucleus from the free gas thermal treatment because non-elastic reaction-cross sections are assumed to be nearly independent of temperature. In MCNP, "absorption" and "capture" are used interchangeably, σ_c and σ_a are used interchangeably also [22].

a. **Analog Capture**: In analog capture, the particle is killed with probability σ_a / σ_T where σ_a and σ_T are the absorption and total cross sections of the collision nuclide at the incoming neutron energy respectively. The absorption cross section is specially defined for MCNP as the sum of all (n, x) cross sections, where ***x*** is anything except neutrons. Thus σ_a is the sum of $\sigma_{n,\gamma}$, $\sigma_{n,\alpha}$, $\sigma_{n,d}$ . . . etc. For all particles killed by analog capture, the entire particle energy and weight are deposited in the collision cell.

b. **Implicit Capture:** For implicit capture, the neutron weight W_n is reduced to $W_n^{'}$ such that $W_n^{'} = [1-(\sigma_a / \sigma_T)]W_n$, the fraction (σ_a / σ_T) of the incident particle weight and energy is deposited in the collision cell corresponding to that portion of the particle that was captured. Implicit capture is the default method of neutron capture in MCNP.

2.2 Photon Interactions

Photons interact with mater via three different ways: photoelectric effect, pair production and scattering.

Photoelectric Effect

The photoelectric effect consists of the absorption of the incident photon of energy ***E***, with the consequent emission of several fluorescent photons and the ejection (or excitation) of an orbital electron of binding energy ***e* < *E***, giving the electron a kinetic energy of ***E* - *e***. Zero, one, or two fluorescent photons are emitted. The description of those three cases is as follows [22]:

(1) Zero photons greater than 1 keV are emitted. In this event, the cascade of electrons that fills up the orbital vacancy left by the photoelectric ejection produces electrons and low-energy photons. These particles can be followed in

Mode P E problems, or be treated with the TTB (Thick-Target Bremsstrahlung) approximation, or be assumed to deposit energy locally. Because no photons are emitted by florescence (some may be produced by electron transport or the TTB model), the photon track is terminated. This photoelectric "capture" of the photon is scored like analog capture in the summary table of the output file. Implicit capture is not possible.

(2) One fluorescent photon of energy greater than 1 keV is emitted. The photon energy E' is the difference in incident photon energy ***E***, less than the ejected electron kinetic energy ***E - e***, and less than the residual excitation energy e' that is ultimately dissipated by further Auger processes. This dissipation leads to additional electrons or photons of still lower energy. The ejected electron and any Auger electrons can be transported or treated with the TTB approximation. In general, $E' = E - (E - e) - e' = e - e'$

(3) Two fluorescence photons can occur if the residual excitation e' of process (2) exceeds 1 keV. An electron of binding energy e'' can fill the orbit of binding energy e', emitting a second fluorescent photon of energy $E'' = e' - e''$. As before, the residual excitation e'' is dissipated by further Auger events and electron production that can be modeled with electron transport in Mode P E calculations, approximated with the TTB model, or assumed to deposit all energy locally. These secondary transitions come from all upper shells and go to **L** shells.

Pair Production

This process is considered only in the field of a nucleus. The threshold is $2mc^2 = [1+(m/M)] \cong 1.022\ \text{MeV}$, where ***M*** is the nuclear mass and ***m*** is the mass of the electron. There are three cases [22]:

(1) In the case of electron transport (Mode P E), the electron and positron are created and banked and the photon track terminates.

(2) For Mode P problems with the TTB approximation, both an electron and positron are produced but not transported. Both particles can make TTB approximation photons. If the positron is below the electron energy cutoff, then it is not created and a photon pair is created as in the following case.

(3) For Mode P problems when positrons are not created by the TTB approximation, the incident photon of energy ***E*** vanishes. The kinetic energy of the created positron/electron pair, assumed to be $E-2mc^2$, is deposited locally at the collision point. The positron is considered to be annihilated with an electron at the point of collision, resulting in a pair of photons, each with the incoming photon weight, and each with energy of $2mc^2 = 0.511\ \text{MeV}$. The first photon is emitted isotropically, and the second is emitted in the opposite direction. The very rare single-annihilation photon of 1.022 MeV is omitted.

Incoherent (Compton) Scattering

To model Compton scattering it is necessary to determine the angle θ of scattering from the incident line of flight (and thus the new direction), the new energy E' of the photon, and the recoil kinetic energy of the electron, $E-E'$. The recoil kinetic energy can be deposited locally, and can be transported in Mode P E problems, or can be treated with the TTB approximation. Incoherent scattering is assumed to have the differential cross section $\sigma_1(Z,\alpha,\mu)d\mu = I(Z,v)K(\alpha,\mu)$ where $I(Z,v)$ is an appropriate scattering factor modifying the Klein-Nishina cross section in Equation (2.3).

The differential cross section for the process is given by the Klein-Nishina formula:

$$K(\alpha,\mu)d\mu = \pi r_o^2 \left(\frac{\alpha'}{\alpha}\right)^2 \left[\frac{\alpha'}{\alpha} + \frac{\alpha}{\alpha'} + \mu^2 - 1\right] d\mu \qquad (2.3)$$

Where $\boldsymbol{r_o}$ is the classical electron radius 2.817938 x 10^{-13}cm, α and α' are the incident and final photon energies in units of 0.511 MeV [$\alpha = E/(mc^2)$, where $\boldsymbol{m}$ is the mass of the electron and $\boldsymbol{c}$ is the speed of light], and $\alpha' = \alpha/[1+\alpha(1-\mu)]$ [22].

Coherent (Thomson) Scattering

Thomson scattering involves no energy loss, and thus is the only photon process that cannot produce electrons for further transport and that cannot use the TTB approximation. Only the scattering angle θ is computed, and then the transport of the photon continues. The differential cross section is $\sigma_2(Z,\alpha,\mu)d\mu = C^2(Z,v)T(\mu)d\mu$ where $C(Z,v)$ is a form factor modifying the energy-independent Thomson cross-section $T(\mu) = \pi r_o^2(1+\mu^2)d\mu$ [22].

2.3 MCNP Features

Various features, concepts, and capabilities of MCNP are summarized in this section. Files created in MCNP contains the information to describe the various parts of the setup design including: **a)** Geometry specification, **b)** Materials and cross-section evaluations, **c)** The neutron, photon, or electron source location and characteristics, **d)** The desired type of answers or tallies, **e)** Variance reduction techniques used to improve the efficiency [22].

Experimental Geometry Specification

MCNP geometry treats an arbitrary three-dimensional configuration of user-defined materials in geometric cells bounded by first- and second-degree surfaces and fourth-degree elliptical tori. The cells are defined by the intersection, unions, and complements of the regions bounded by the surfaces. Surfaces are defined by supplying coefficients to the analytic surface equations or, for certain types of surfaces, known points on the surfaces. MCNP has a more general geometry than is available in most combinatorial geometry codes. Instead of combining several predefined geometrical bodies as in a combinatorial geometry scheme, MCNP gives the user the flexibility of defining geometrical regions from all the first and second degree surfaces of analytical geometry and elliptical tori and then of combining them with Boolean operators. The code does extensive internal checking to find input errors. Additionally, the geometry-plotting capability in MCNP helps the user check for geometry errors [22].

Material and Nuclear Cross-Section Data Library

MCNP code uses continuous-energy nuclear and atomic data libraries. Over 500 neutron interaction tables are available for approximately 100 different isotopes and elements.

Multiple tables for a single isotope are provided primarily because data have been derived from different evaluations, but also because of different temperature regimes and different processing tolerances. Photon interaction tables including coherent and incoherent scattering, photoelectric absorption exist for all element from $Z=1$ through $Z=94$. Cross sections for nearly 2000 dosimetry or activation reactions involving over 400 target nuclei in ground states are part of the MCNP data package. Users may select specific data tables through unique identifiers for each table.

Neutron and Gamma Source Specification

In MCNP the user is allowed to specify a wide variety of source conditions without making code modifications. Independent probability distributions may be specified for the source variables of energy, time, position and direction, and for other parameters such as starting cell(s) or surface(s). Information about the geometrical extent of the source can also be given. The source selection list in the input file is symbolized by SDEF, which is followed by some source parameter, such as position, energy, radiation type…etc. [22].

Tallies and Output

Tallies represent the digital record of the random events from neutron interaction with the sample elements. MCNP can be instructed to make various tallies related to particle current, particle flux, and energy deposition. MCNP tallies are normalized to be per starting particle except for a few special cases with criticality sources. Currents can be tallied as a function of direction across any set of surfaces, surface segments, or sum of surfaces in the problem. Charge can be tallied for electrons and positrons. Fluxes across any set of surfaces, surface segments, sum of surfaces, and in cells, cell segments, or sum of cells are also available. Similarly, the fluxes at designated detectors are standard tallies [22].

Estimation of Monte Carlo Errors

MCNP tallies are normalized to be per starting particle and are printed in the output accompanied by a second number ***R***, which is the estimated relative error defined to be one estimated standard deviation of the mean $S_{\bar{x}}$ divided by the estimated mean $\bar{x}$ $(R = S_{\bar{x}} / \bar{x})$. In MCNP, the quantities required for this error estimate are computed after each complete Monte Carlo history, which accounts for the fact that the various contributions to a tally from the same history are correlated. For a well-behaved tally, ***R*** will be proportional to $1/\sqrt{N}$ where ***N*** is the number of histories. Thus, we must increase the total number of histories fourfold in order to halve ***R***. For a poorly behaved tally, ***R*** may increase as the number of histories increases. The quantity ***R*** should be less than 0.10 to produce generally reliable confidence intervals. For a given MCNP run, the computer consumed time ***T*** proportional to ***N***. Thus:

$R = C\big/\sqrt{T}$, where ***C*** is a positive constant. There are two ways to reduce ***R*** (estimated relative error); by increasing ***T*** and / or decreasing ***C***. Computer budgets often limit the utility of the first approach. For example, if it has taken 2 hours to obtain $R = 0.10$, then 200 hours will be required to obtain $R = 0.01$. For this reason MCNP has special variance reduction techniques for decreasing ***C***, the constant ***C*** depends on the tally choice and / or the sampling choices [22].

CHAPTER 3

DESIGN AND TESTS OF ACCELERATOR-BASED PGNAA SETUPS

In this part, the performance tests of a D-D reaction based portable pulsed neutron generator model MP320 for PGNAA are discussed. The optimum operating beam energy and beam current of the MP320 generator were determined through prompt gamma-ray yield measurements from iron.

The performance of 3 in x 3 in (diameter x height) lanthanide-halides ($LaBr_3$:Ce and $LaCl_3$:Ce) gamma-ray detectors was evaluated by analyzing Boron and Cadmium-contaminated water samples. Also, a 5 in x 5 in (diameter x height) bismuth germinate (BGO) gamma ray detector was tested by analyzing Hg-contaminated water samples. Finally, the chlorine prompt gamma ray yield was measured from saline water samples containing 1.0 to 4.0 wt. % chlorine to test the suitability of the PGNAA setup for sample analysis.

3.1 Monte Carlo Design Calculations of PGNAA Setup

The PGNAA setup was designed using MCNP4B2 code [22]. This code is used to transport neutral radiation like gamma rays and neutrons through a predefined geometrical setup.

As shown in Figure 3.1, the PGNAA setup consists of a cylindrical sample placed in a cylindrical cavity drilled inside a cylindrical high density polyethylene moderator. A cylindrical gamma-ray detector is used with its longitudinal axis aligned along the sample's longitudinal axis. The neutron beam axis is at right angle with respect to the longitudinal axis of the cylindrical specimen. In order to prevent undesired gamma-rays and neutrons from reaching the detector, 3 mm thick lead shielding and 50 mm thick neutron shielding are used to surround the gamma-ray detector. The neutron shielding is made of a mixture of paraffin and lithium carbonate mixed in equal weight proportions.

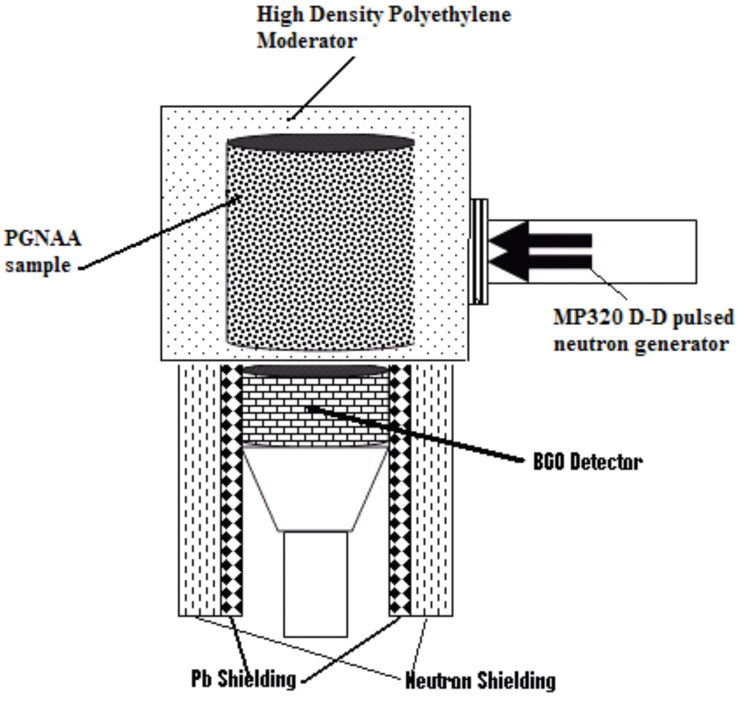

Figure 3.1 Schematic of MP320 portable neutron generator based PGNAA setup.

The optimum values of the sample radius and length that can produce maximum yield of the prompt gamma-rays at the detector location were determined from Monte Carlo simulations [24, 25]. They were obtained through prompt gamma-ray yield calculations from an iron sample as a function of the sample radius and length for the moderator with 200-350 mm outer diameter. The iron sample was chosen because it has high energy prompt gamma-rays that can be easily discriminated from the low energy room-scattered inelastic gamma rays. The energies and production cross-sections of prompt gamma rays of iron are given in Table 3.1 [23]. The design calculations of the PGNAA set up were carried out utilizing a PC based workstation. The moderators and sample cells were divided into sub-cells of 1 cm thickness. This allowed study of the transport of the neutrons of appropriate statistical weight to the next adjacent cell, without any loss. A mono-energetic neutron source was simulated and energy deposition tally was used to simulate the gamma ray detector.

Element	**Gamma-ray energy (MeV)**	**$\sigma_\gamma^Z(E_\gamma)$-barns**
Fe	5.920	0.225
	6.018	0.227
	7.278	0.137
	7.631	0.653
	7.645	0.549

Table 3.1 Energies and partial elemental cross section $\sigma_\gamma^Z(E_\gamma)$ of prominent capture gamma rays of iron [23].

Figure 3.2 shows the 7.6 MeV prompt gamma-ray yield from an iron sample as a function of sample radius for three moderators with 200, 250 and 300 mm radii. For 250 mm diameter moderator, the gamma-ray yield increases with the sample radius, reaches a maximum value for sample with 40 mm radius and then decreases with a further increase in the sample radius. The initial increase in the intensity of prompt gamma-rays with specimen radius is due to an increase in the sample size and the sharp decrease in the prompt gamma-ray yield for sample radii in excess of 40 mm may be due to the insufficient wall thickness of the moderator to moderate and reflect the neutrons. A similar behavior has been observed for prompt gamma-ray yield from the other two moderators with 200 and 300 mm radii but with lesser intensity of maximum prompt gamma-ray yield for optimum sample radii.

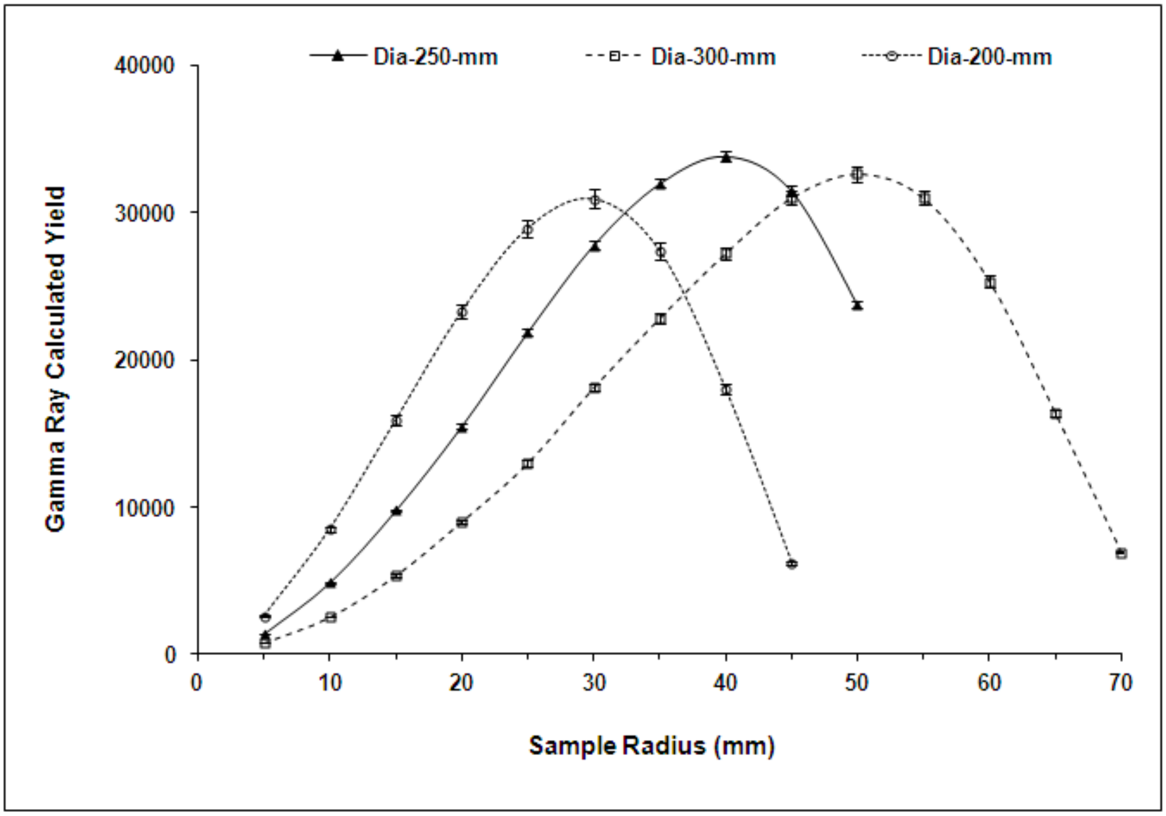

Figure 3.2 Calculated prompt gamma-ray yield plotted as a function of sample radius for moderators with 200, 250 and 300 mm diameter.

For moderators with 200 and 300 mm external diameter, the optimum radii of the sample to produce maximum yield of gamma-rays were observed to be about 30 and 50 mm, respectively. For the three moderators the wall thickness of the moderator to produce maximum thermal neutron flux varies between six and seven cm. With increasing moderator diameter, the corresponding maximum intensity of the prompt gamma-rays drops due to increasing distance of the cylinder center from the neutron source. Results of the calculations for the three moderator diameters shows that the optimum gamma ray yield is obtained with a 40 mm sample radius for a moderator with 250 mm outer diameter. Plastic cylindrical containers of 90 mm diameter were commercially available and were used as sample containers. Therefore, a 45 mm sample radius was used in further calculations. The gamma ray yield does not change significantly by increasing the sample radius from 40 mm to 45 mm, and finally, the sample length was varied to obtain the maximum prompt gamma-ray yield. Figure 3.3 shows the prompt gamma-ray yield for iron as a function of the sample length for a 45 mm radius sample and a moderator with 250 mm outer diameter.

The prompt gamma-ray yield initially increases with sample length up to 120 mm, saturates over a sample length of 120-130 mm, and drops off with further increase in sample length. The initial increase in the yield is due to increasing sample size while the yield saturation may be due to a balance between gamma-ray production and attenuation over the length of the sample. The final drop in the yield is due to dominating gamma-ray attenuation effects over the length of sample. Due to the availability of 90 mm diameter and 140 mm long plastic containers, a sample with 90 mm diameter and 140 mm length was selected. Extension from an optimum sample length of 120-130 mm to 140 mm may result in a gamma ray yield loss of only 2-3%, which can be compensated by increasing the neutron flux.

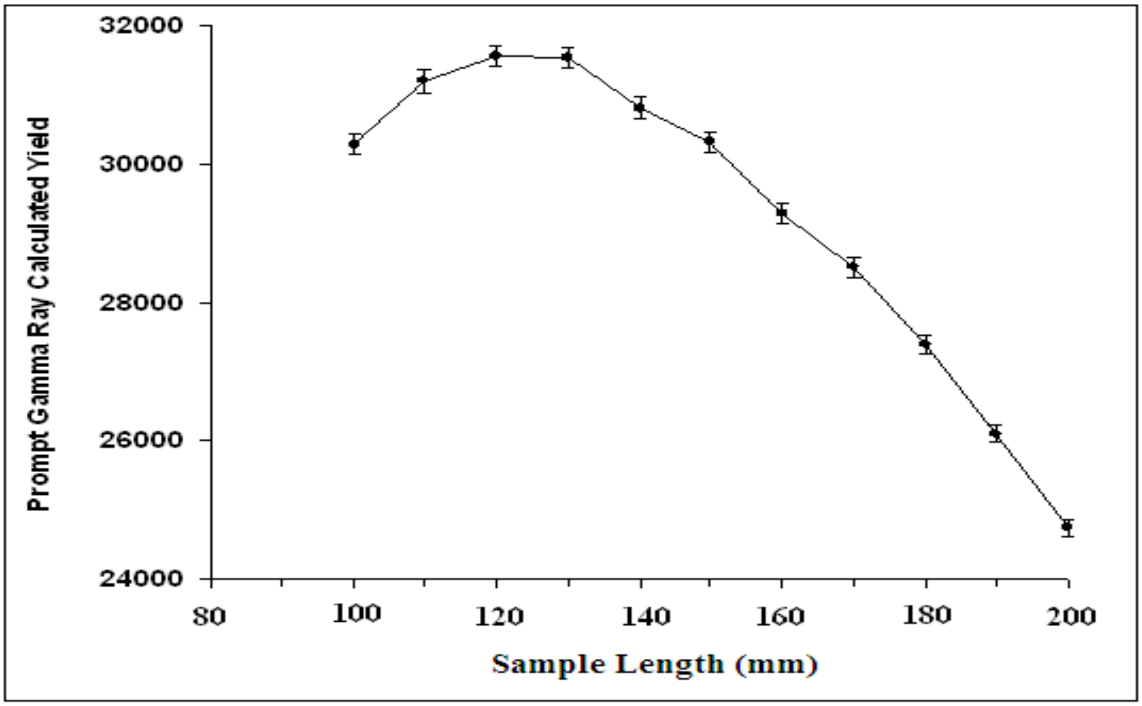

Figure 3.3 Calculated prompt gamma-ray yield plotted as a function of sample length for 250 mm diameter moderator and 45 mm sample radius.

3.2 Portable Neutron Generator Tests

Portable neutron generators are widely used in neutron activation field measurements. KFUPM has acquired a ThermoScientific® MP320 D(d,n) reaction based 2.5 MeV portable neutron generator for its prompt gamma analysis program. It is lightweight, about 10 kg, and is suited for field or laboratory applications. Table 3.2 shows some of the MP320 specifications [21].

MP320 Parameters	**Values**
Maximum neutron yield, n/s	2x 10^6
Rated neutron yield,* n/s	>1x 10^6
Time @ rated yield, hours	600
Pulse frequency range,	Hz 100–20,000
Pulse duty cycle range	5–100%
Pulse rise time, μs	Variable <1
Pulse fall time, μs	<1, <1
Minimum pulse width, μs	5
Operating high voltage, kV	45-75
Beam current, μA	25-80
Operating temperature range, °C	–25 to +50
Input power requirements	120/220 VAC (50–60 Hz)
Total system weight, kg	12
Neutron generator weight, kg	10
Neutron generator physical dimension (Diameter x Length)	12.1 cm x 57.2 cm

Table 3.2 MP320 Neutron generator specifications sheet [21]

*** Rated yield for D-D neutron MP320 generator**

Neutrons with 2.5 MeV energy are produced in the MP320 generator using a 30-80 μA deuteron beam current accelerated through an accelerator voltage of 45-75 kV. The neutron flux produced by the accelerator depends upon the deuteron beam current and energy, taking into account beam energy loss in the neutron-producing target. In order to lengthen the useful life of the neutron-producing target of the generator, one needs to determine the optimum operating voltage of the accelerator to produce the maximum neutron flux.

The optimum beam voltage and current of the MP320 neutron generator were determined from prompt gamma-ray yield measurement from an iron sample as a function of the generator beam voltage and current. The cylindrical iron sample, with 90 mm x 140 mm (diameter x height) dimensions, was enclosed in the moderator with 250 mm diameter and was irradiated with a 2.5 MeV pulsed neutron beam from the portable neutron generator.

The portable neutron generator can deliver continuous (dc) or pulsed neutrons. In dc mode, the gamma ray background is continuously produced due to the interaction of thermal and fast neutrons with the detector, shielding material and material of the beam lines. In pulsed mode, the average beam associated gamma ray background is less. Therefore pulsed beam gamma ray spectra have improved signal-to-background ratio as compared to dc beam experiments. The neutron generator was operated in pulsed mode at 250 Hz frequency with 5 % duty cycle. The deuteron pulse had a width of 200 μs. The typical beam voltage and current of the generator were 70 kV and 70 μA. The prompt gamma-rays produced in the iron samples were detected by a cylindrical 125 mm by 125 mm (diameter x length) bismuth germinate (BGO) detector. The BGO detector was chosen because of its higher resistance to neutron radiation damage [26].

The prompt gamma-ray yield data from the iron sample were acquired as a function of deuteron beam energy and deuteron beam current. The prompt gamma-ray yield data was taken for deuteron beam energies of 45, 50, 55, 60, 65, 70 and 75 keV and for 30, 40, 50, 60 and 70 μA. Figure 3.4 shows a prompt gamma-ray experimental pulse height spectrum from an iron sample with a 50 keV deuteron beam and 70 μA beam current showing different prompt gamma rays peaks over 0.68 MeV to 9.86 MeV energy range. Also superimposed on the spectrum is the background gamma ray spectrum taken without the sample using a 45 keV deuteron beam with 70 μA beam current. The background spectrum will be used to extract net peak counts.

There are several prompt gamma-rays emitted due to thermal neutron capture in the iron sample, BGO detector material, hydrogen moderator material as well as lead shielding, as shown in Figure 3.4. The main prompt gamma-rays are emitted by iron at 5.902, 6.018, 7.278, 7.631 and 7.645 MeV. Due to the poor energy resolution of the BGO detector (about 11 % energy resolution for 662 keV gamma rays from ^{137}Cs source), the gamma-rays of energies 5.902 and 6.018 MeV could not be resolved, neither could the gamma-rays at 7.631 and 7.645 MeV. The relative cross sections of theses gamma-rays are given in Table 3.1 [23].

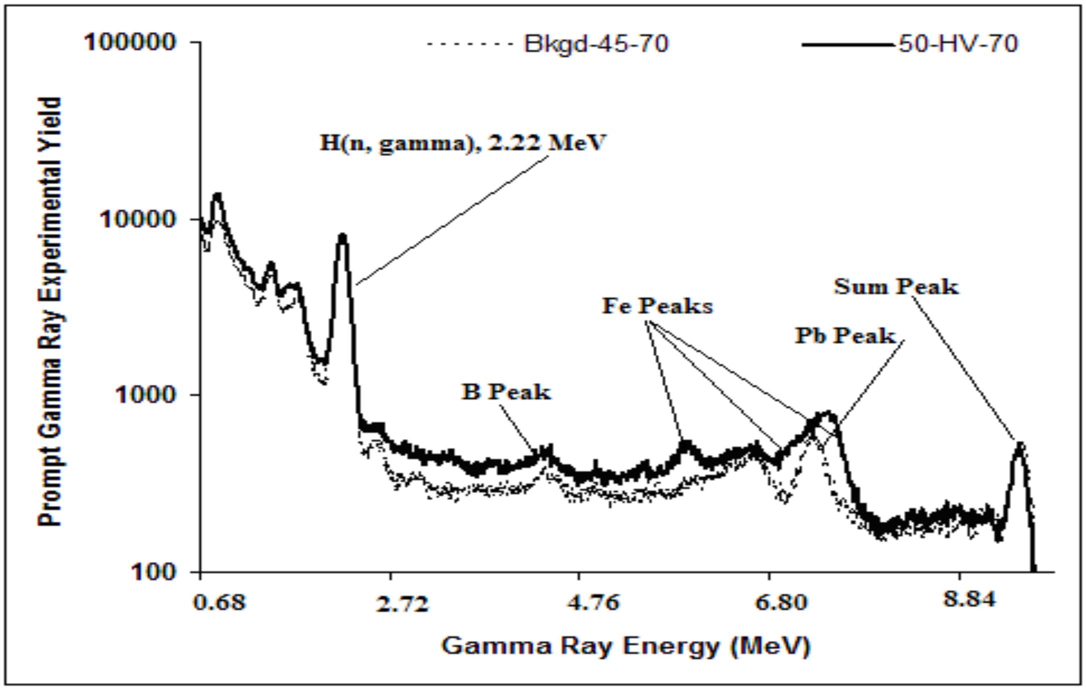

Figure 3.4 Prompt gamma-ray experimental pulse height spectrum from an iron sample with 50 keV deuteron beam and 70 μA beam current showing different prompt gamma rays peaks. Also superimposed on the spectrum is background gamma ray spectrum without the sample taken with 45 keV deuteron beam and 70 μA beam current

Figure 3.5 shows the pulse height spectra of gamma-rays over 2.72-9.86 MeV energy range from the iron sample taken at 50 kV accelerator operating voltage with 70 μA beam current along with the gamma-ray background spectrum taken without sample at 50 kV operating voltage and 70 μA beam current.

The main features of Figure 3.5 are the significant increase in intensity of iron peaks at 5.902 - 6.018 MeV against the background spectrum, the interference of iron gamma ray doublet at 7.631- 7.645 MeV with the prompt gamma-ray peak from ^{207}Pb at 7.367 MeV present in the background spectrum, and the interference of the full energy peak at 7.278 MeV from iron with the single escape peaks of the iron doublet at 7.631- 7.645 MeV as well as single escape peak of 7.367 MeV from ^{207}Pb.

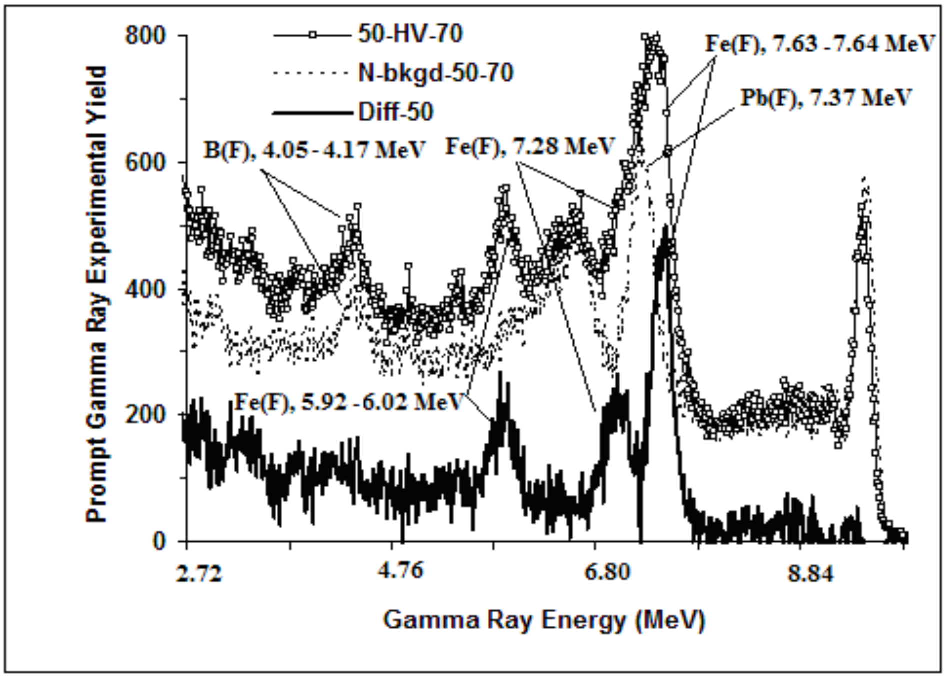

Figure 3.5 Prompt gamma-ray experimental pulse height spectra over 2.72-9.86 MeV from an iron sample taken with 50 keV beam voltage and 70 μA beam current of the accelerator along with background gamma-ray spectrum. Also superimposed is the difference spectrum.

The prompt gamma ray peaks due to capture of thermal neutrons in Bi present in the BGO detector appear at 4.054 and 4.171 MeV in sample and background spectra. Also superimposed in Figure 3.5 is the difference spectrum, which was obtained by subtracting the background spectrum from the iron sample spectrum. The difference spectrum clearly shows the 5.902-6.018 MeV, 7.278 MeV, and the 7.63-7.64 MeV iron gamma ray peaks sitting on an almost constant background.

Figure 3.6 shows the pulse height gamma-ray spectra over 2.72-9.86 MeV energy range from an iron sample taken at 45-75 kV accelerator operating voltage in 5 keV steps with fixed 70 μA beam current. Also, superimposed in Figure 3.6 is a prompt gamma-ray pulse height background spectrum taken without sample at 45 kV operating voltage and 70 μA beam current.

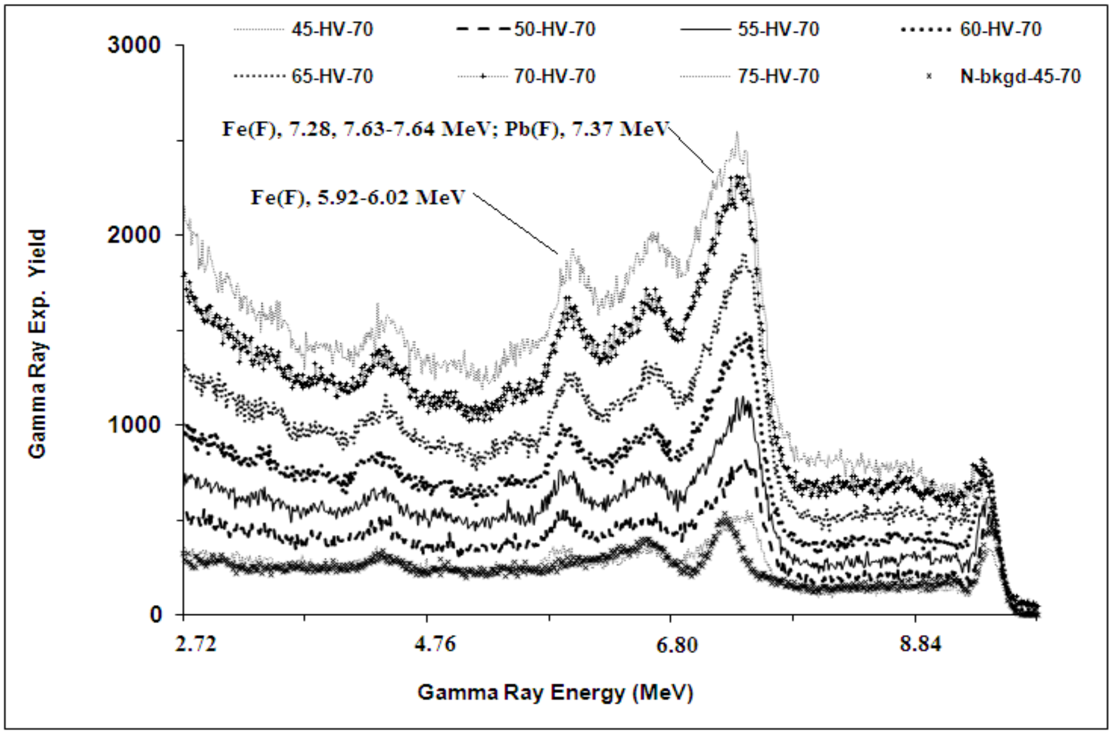

Figure 3.6 Prompt gamma-ray experimental pulse height spectra from an iron sample over 2.72-9.86 MeV taken with 45, 50, 55, 60, 65, 70 and 75 keV deuteron beam with 70 μA beam current. Also superimposed on the spectrum is background gamma-ray spectrum.

The main feature of Figure 3.6 is the increasing intensity of 5.92-6.02 MeV, 7.28 MeV, and 7.63-7.64 MeV iron prompt gamma ray peaks with increasing operating voltage of the accelerator (hence increasing neutron flux). In order to obtain the prompt gamma-ray yield as a function of beam voltage, the background spectra were subtracted from the iron spectra shown in Figure 3.6.

Figure 3.7 shows the difference spectra of prompt gamma-rays from the iron sample spectra shown in Figure 3.6 after subtracting the background. Prominent prompt gamma-ray peaks at 5.92-6.02 MeV, 7.28 MeV and 7.63-7.64 MeV from iron are clearly visible.

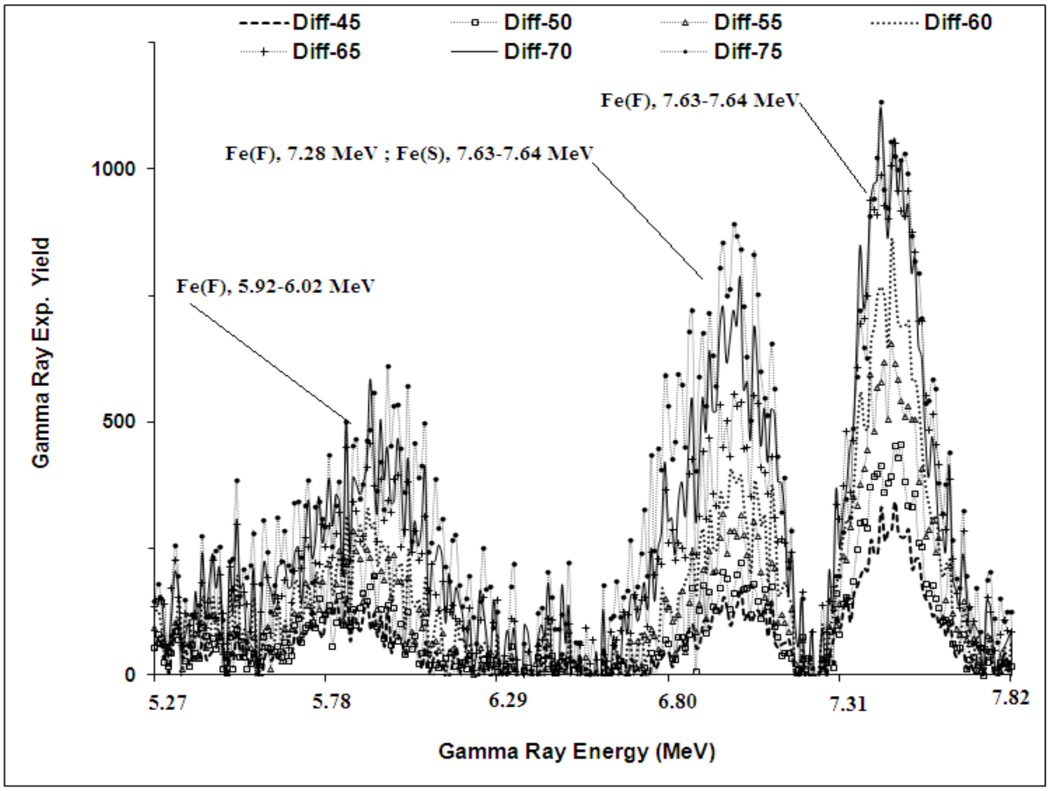

Figure 3.7 Prompt gamma-ray pulse height difference spectra from an iron sample over 2.72-9.86 MeV for 45, 50, 55, 60, 65, 70 and 75 keV deuteron beam at 70 μA beam current.

Finally, the counts under each peak were integrated and normalized to the same amount of measurement time. Figure 3.8 shows the normalized experimental yield of 7.63-7.64 MeV prompt gamma-rays from iron plotted as a function of deuteron beam current for 45, 50, 55, 60, 65, and 70 keV deuteron beams. Lines are drawn through the points to show the data trend. The yield of 7.63-7.64 MeV prompt gamma-rays increases with increasing beam current as well as beam voltage. The optimum operating parameters of the MP320 neutron generator to produce maximum yield of prompt gamma-ray yield were observed to be 60 keV deuteron beam energy with 60 µA beam current.

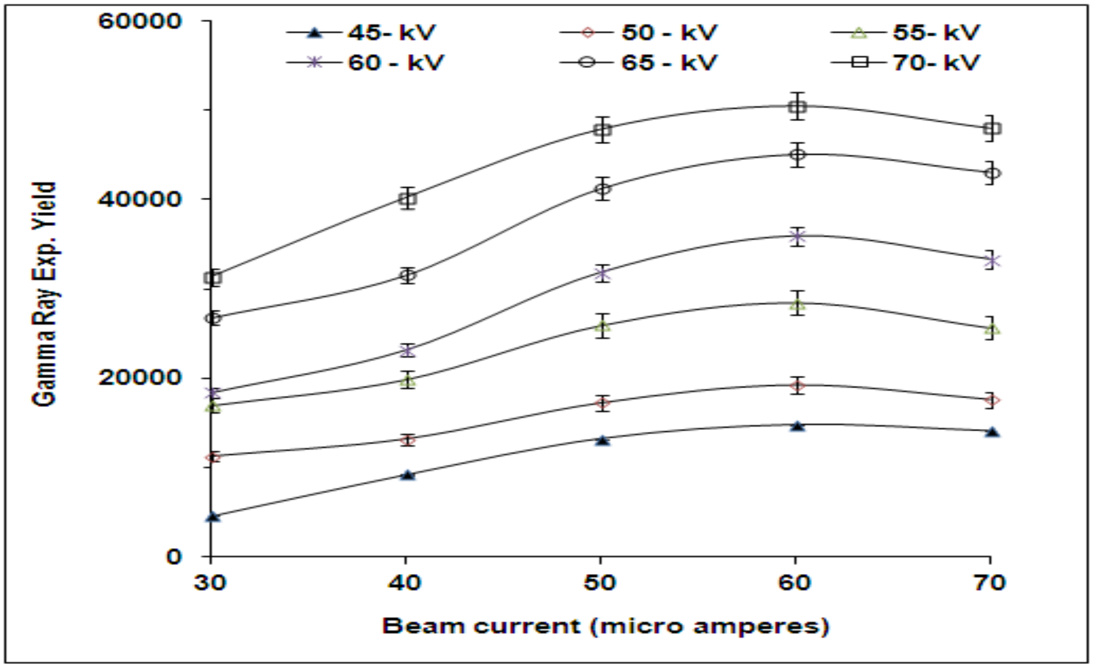

Figure 3.8 Experimental integrated yield of 7.6 MeV prompt gamma-rays from iron plotted as a function of 30, 40, 50, 60 and 70 µA beam current for 45, 50, 55, 60, 65, and 70 keV deuteron beam energies. Lines are drawn through the points to show the data trend.

3.3 Gamma Ray Detectors Tests

In order to obtain the maximum yield of detected gamma rays, the performance of 3 in x 3 in lanthanide-halides ($LaBr_3$:Ce and $LaCl_3$:Ce) gamma-ray detectors was evaluated by performing analysis of Boron and Cadmium contaminated water samples. Also, a 5 inches x 5 inches (diameter x height) bismuth germinate (BGO) gamma ray detector was evaluated by performing analysis of Hg-contaminated water samples.

Experimental Setup

For the 3 in x 3 in lanthanide-halides ($LaBr_3$:Ce and $LaCl_3$:Ce) gamma-ray detectors a common setup was used, it consists of a cylindrical sample placed inside a cylindrical moderator made of high density polyethylene, as shown in Figure 3.9. A gamma-ray detector was placed with its longitudinal axis aligned along the major axis of the moderator. The Longitudinal axis of the sample was at right angle to the neutron beam axis. Lead shielding of 3 mm and paraffin shielding of 50 mm were provided around the detector in order to minimize unwanted gamma-rays and neutrons at the detector. Neutron shielding was made up of a mixture of paraffin and lithium carbonate mixed in equal weight proportions.

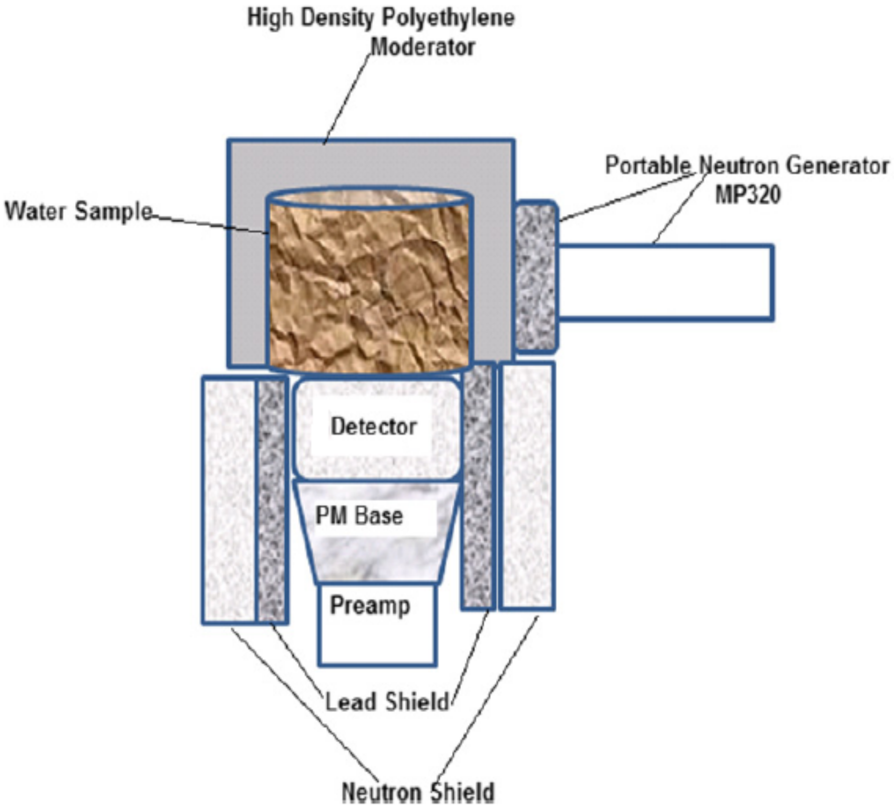

Figure 3.9 Schematic representation of the MP320 portable neutron generator used to measure the prompt gamma-ray yield from boron & cadmium samples.

The results of the Monte Carlo simulations showed that the optimum dimensions for radius and length were 90 and 145 mm, respectively, for a moderator of 25 cm outer diameter. Boron- and Cadmium-contaminated water samples were prepared by mixing B and Cd compounds with water. The Boron samples were prepared by mixing 0.031, 0.125, 0.250 and 0.5 wt% B with a known volume of water [27, 28]. The Cadmium samples were prepared with 0.0625, 0.125, 0.250 and 0.500 wt% Cd, mixed with a known volume of water.

Samples are put in cylindrical plastic bottles of 14 cm length and 9 cm internal diameter. They were then irradiated using a pulsed beam of 2.5 MeV neutrons with 70 keV voltage and a current of 70 μA. The prompt gamma-ray data from B- and Cd-contaminated water samples was acquired for 25 min.

Detectors signals were acquired using standard NIM electronics modules. For each detector, the signal that was routed through a preamplifier was processed through a spectroscopy amplifier with shaping time of 1 μs. A Logical gate signal was generated for each signal processed by the amplifier using single channel analyzer and gate and delay generator modules. For dead time correction, one of the outputs of the gate and delay generator was used to gate the Multichannel Buffer, while another output was used to calculate the dead time correction.

Dead time correction (DTC) was calculated at the end of each experimental run from the integrated count in the stored spectrum N_{tot} and total gate signals N_{gates}, counted independently through the relation [27, 28, 29]:

$$DTC = \frac{N_{gates} - N_{tot}}{N_{gates}} \tag{3.1}$$

The dead time corrected counts under a peak $Y_{DTC\text{-}Corr}$ were then obtained from the experimental counts under the peak Y_{exp} using the relation:

$$Y_{DTC-Corr} = Y_{\exp}(1 + DTC) \tag{3.2}$$

The dead time correction depends upon the sample as can be seen in the following section.

3.3.1 LaBr$_3$:Ce Detector Tests

Figure 3.10 shows the pulse height spectrum of the LaBr$_3$:Ce detector taken with a ^{137}Cs source. This figure shows the Cs peak along with the intrinsic activity lines due to the decay of ^{138}La isotope. The detector has 3.3% energy resolution for 662 keV gamma-rays from ^{137}Cs. Three intrinsically produced photon peaks from the decay of La are generally observed at 32 keV, 789 keV and 1436 keV [30]. The 32 keV X-ray peak is produced by 32.2 keV K shell X-ray fluorescence of Br; where Br is produced due to the electron capture of La. The 789 keV and 1436 keV gamma lines originate from the beta decay and electron capture branches, respectively, of La [30].

In Figure 3.10, only 789 keV gamma line (sitting on the beta continuum) and 1468 keV gamma-ray peak (sum line of 32 keV X-ray fluorescence peak and 1436 keV gamma line) are shown. This is in agreement with that observed in reference 30]. The abnormal width of the sum line of 32 keV X-ray fluorescence peak and 1436 keV gamma line may be due to the overlapping of 1436 keV gamma line from La with 1460 keV line of ^{40}K, originating from the glass of the photomultiplier tube [30].

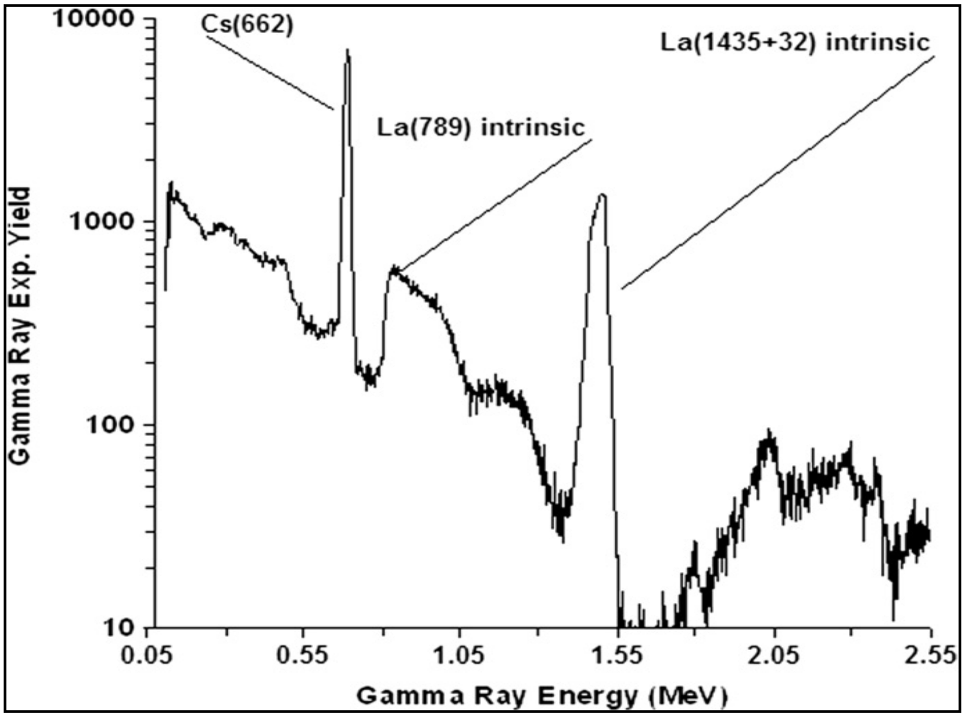

Figure 3.10 LaBr$_3$:Ce pulse height spectrum taken with ^{137}Cs source exhibiting ^{137}Cs peak along with detector intrinsic activity peaks due to ^{138}La.

During sample irradiation, the LaBr$_3$:Ce detector, although shielded, is exposed to thermal neutrons and it registers the prompt gamma-rays due to capture of thermal neutrons in La, Br and Ce elements present in LaBr$_3$:Ce detector. This activation spectrum of the detector also contains additional peaks due to the intrinsic activity from Lanthanum present in the detector. Energies and intensities of prominent prompt gamma-rays due to capture of thermal neutrons in Lanthanum, Cerium and Bromine are listed in Table 3.3 [23]. All these peaks are present in the sample activation spectra taken with the detector and need to be subtracted as beam associated background.

The detector was exposed to fast as well as thermal neutrons and the prompt gamma-ray spectrum was recorded from the detector without sample using a pulsed beam of 2.5 MeV neutrons with 70 μA beam of 70 keV deuterons. The deuteron pulse had a width of 5 ns and a frequency of 250 Hz. Figure 3.11 shows beam associated background spectrum of the $LaBr_3$:Ce detector taken during a 20 min run. Due to short irradiation time, the delayed gamma-rays from ^{140}La (half life = 40.3 h) could not be observed. Figure 3.11 shows the intrinsic activity line along with prompt gamma-ray peaks due to activation of La, Br and Ce elements in the detector. Also shown in the spectrum is the 2.22 MeV capture peak from hydrogen in the moderator and neutron shielding of the detector. The aluminum (Al) prompt gamma peak originates from aluminum used in the detector. All of the prompt gamma-ray lines of lanthanum, cerium and bromine listed in Table 3.3 have been identified in Figure 3.11.

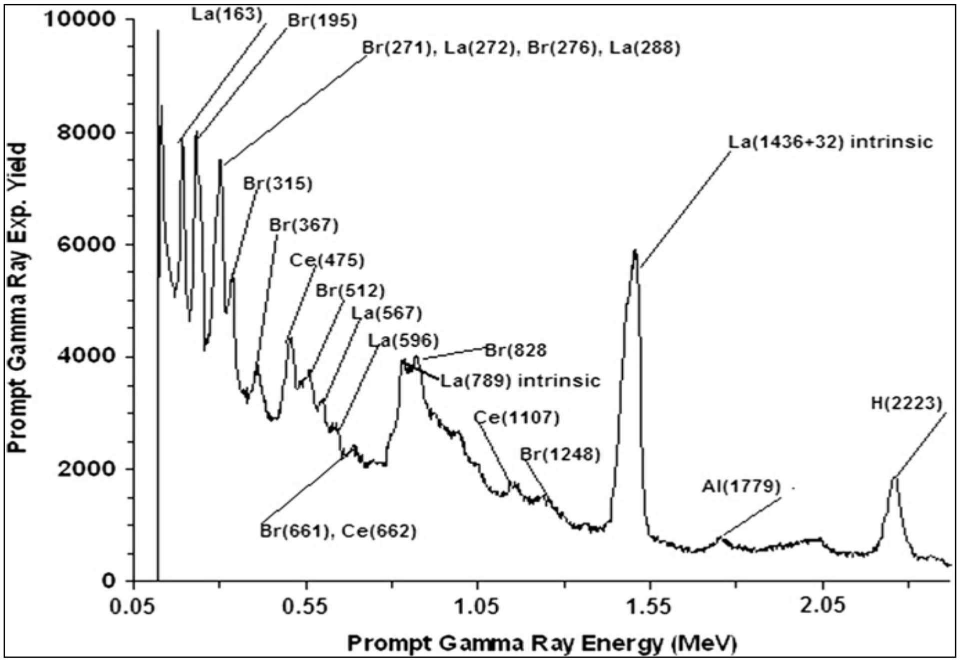

Figure 3.11 Prompt gamma-ray spectrum due to activation of the $LaBr_3$:Ce detector caused by capture of thermal neutrons in La, Br and Ce elements present in $LaBr_3$:Ce detector

Element	Gamma-ray energy (keV)	$\sigma_\gamma^z(E_\gamma)$ barns
B(n,α)	478	716
Br	196	0.434
	271	0.462
	275	0.158
	315	0.460
	367	0.223
	513	0.210
	661	0.082
	828	0.285
	1248	0.0527
Cd	245	247
	558	1860
	651	359
Ce	475	0.082
	662	0.241
	1107	0.040
La	163	0.489
	272	0.502
	288	0.730
	567	0.335
	595	0.103
	789	intrinsic
	1436	intrinsic

Table 3.3 Energies and partial elemental cross section $\sigma_\gamma^z(E_\gamma)$-barns of prominent capture gamma-rays of boron, bromine, cerium and lanthanum [23].

Prompt Gamma-Ray Measurements of Boron and Cadmium in Water Samples

The prompt gamma-ray analysis of boron and cadmium contaminated water samples was carried out using the $LaBr_3$:Ce detector. The boron and cadmium contaminated water samples were prepared by mixing boron and cadmium compounds with water. The boron and cadmium were thoroughly mixed with pure water and thereafter poured in cylindrical plastic bottles with 145 mm length and 90 mm internal diameter. Four cadmium samples with 0.0625, 0.125, 0.25 and 0.50 wt% cadmium concentration and four boron samples with 0.031, 0.125, 0.250 and 0.50 wt% boron concentration were prepared. The concentration of boron and cadmium in water samples was independently measured using Atomic Absorption Spectrometry Laboratory in the Chemistry department of King Fahd University of Petroleum and Minerals. The water samples were then irradiated in the newly designed PGNAA setup built around the MP320 neutron generator. Pulsed neutrons were produced using the pulsed deuteron beam with specifications given earlier. The pulsed neutron beam improves the signal to background ratio in the PGNAA studies. The prompt gamma-ray data from boron and cadmium contaminated water samples were acquired for a preset time using a Multichannel Buffer based data acquisition system. The dead time correction was calculated for prompt gamma-ray spectra of boron and cadmium water samples using Equations (3.1) and (3.2). As expected, the dead time was small for low concentrations and increased with increasing concentration. For the four boron samples with 0.031, 0.125, 0.250 and 0.50 wt%, the dead time correction was calculated to be: 3.8, 5.0, 8.8 and 25%, respectively. Since the capture cross-section of cadmium is almost 2.5 times that of (n, α) cross-section of boron, we operated the neutron generator in cadmium runs with half of the beam current as compared to boron runs. For the four cadmium samples with 0.0625, 0.125, 0.25 and 0.50 wt% cadmium the dead time correction was measured to be: 2.5, 5.0, 8.8 and 21%, respectively.

The neutron flux during each run was monitored using a cylindrical 3 in. × 3 in. (height × diameter) NE213 detector with pulse shape discrimination. The NE213 detector was placed at a distance of 1.0 m from the neutron generator. The neutron detector signals were acquired through a single channel analyzer whose lower level was set at half-Cs pulse height bias electronically set by taking Compton edge spectrum of ^{137}Cs gamma ray source with the NE213 detector. The neutron monitor spectrum was recorded for each concentration of boron and cadmium and was used for neutron flux normalization during data analysis.

Figure 3.12 shows pulse height spectra of prompt gamma-rays from water samples containing 0.031, 0.125, 0.250 and 0.5 wt% boron superimposed upon each other along with background spectrum taken without sample. In order to show the effect of increasing concentration of boron on the pulse height spectrum, pulse height spectra for different boron concentrations are plotted with a constant vertical offset. The 478 keV boron gamma-ray peak along with the intrinsic 1436 keV intrinsic activity peak and the 2223 keV hydrogen capture peak from the moderator are quite prominent. Figure 3.13 shows the 478 keV boron peak on an enlarged scale to show its interference with the 475 keV peak from activation of cerium in $LaBr_3$:Ce detector. Since the boron peaks contain a contribution from the Ce(475) peak, difference spectra of boron peaks for 0.031, 0.125, 0.250 and 0.500 wt% concentration were generated by subtracting the background spectrum from each of them.

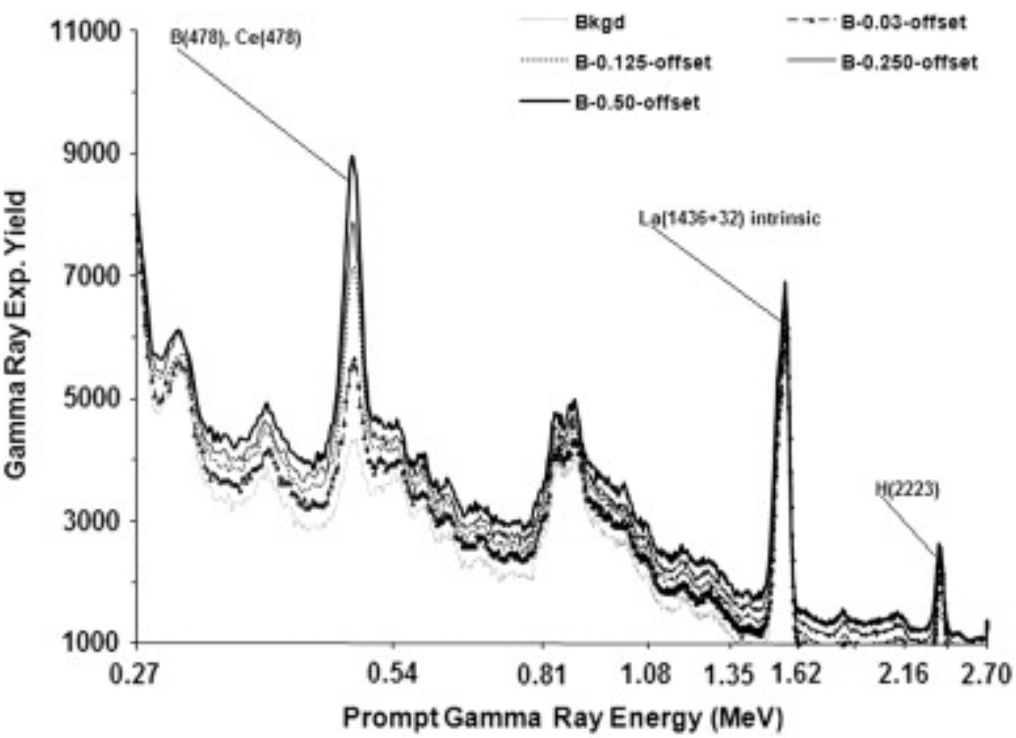

Figure 3.12 Prompt gamma-rays pulse height spectra of four boron-contaminated water samples obtained by LaBr$_3$:Ce detector.

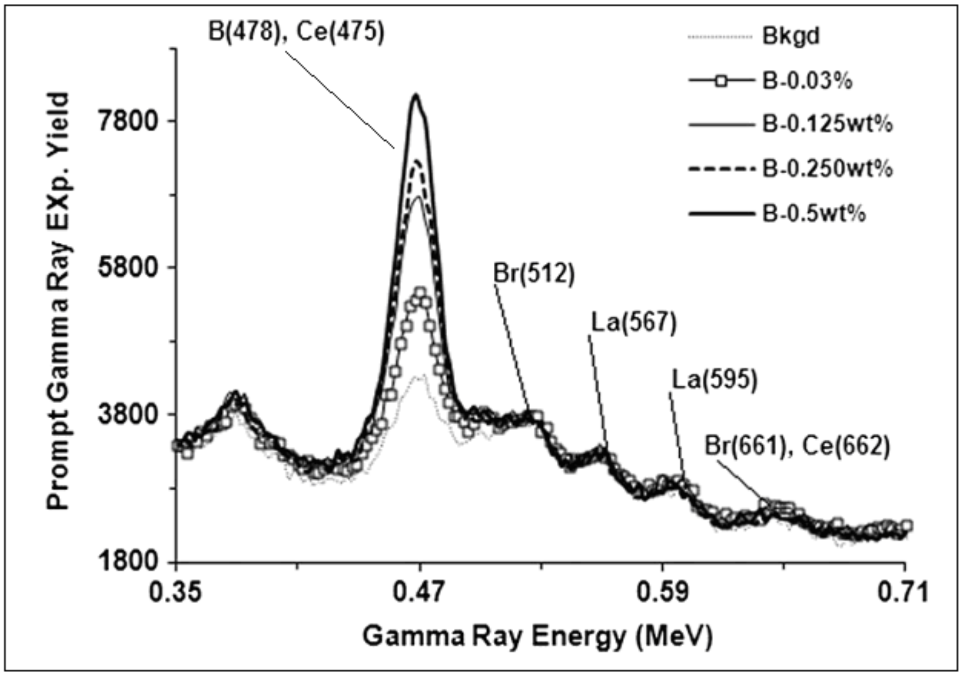

Figure 3.13 Enlarged spectra of boron gamma ray peaks superimposed upon each other for pure water and water containing 0.5, 0.25, 0.125 and 0.03125 wt.% of boron, obtained with LaBr$_3$:Ce detector

Figure 3.14 shows the difference spectra of boron peaks for 0.031, 0.125, 0.250 and 0.500 wt% boron concentration. Finally, the peaks of the difference spectra were integrated to generate integrated yield as a function of boron concentration. The integrated boron yield data for each boron concentration was corrected for dead time and neutron flux fluctuations. The background of the difference spectra from the dead time corrected counts was subtracted from the corrected counts.

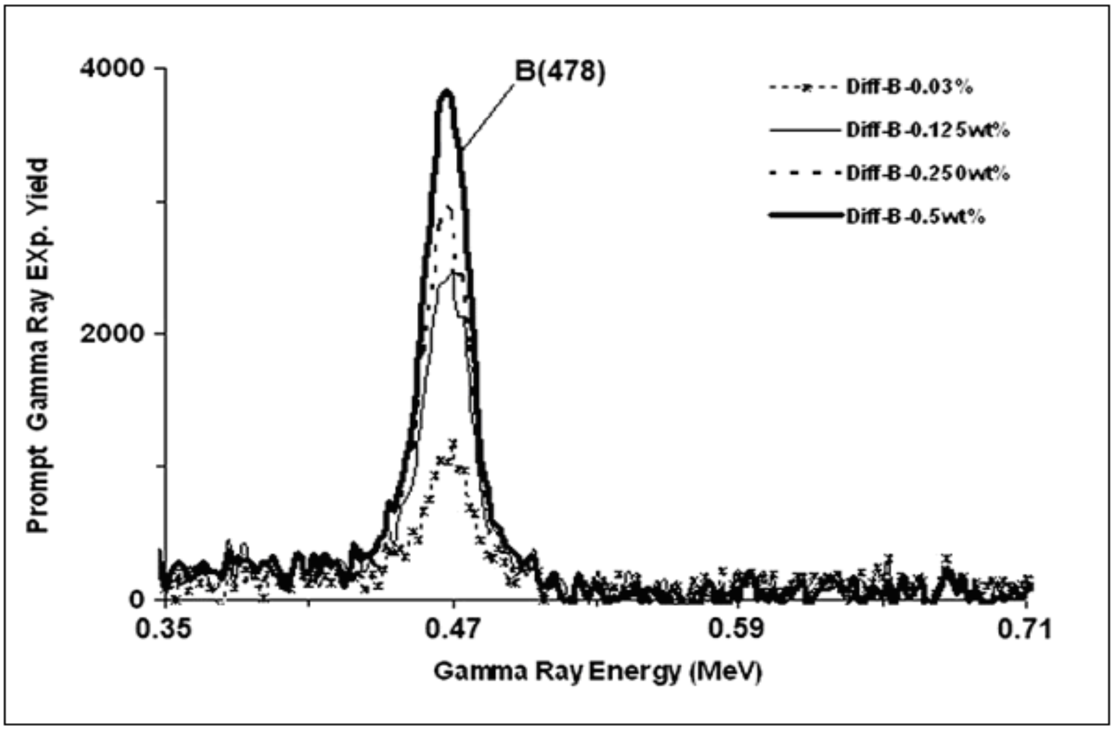

Figure 3.14 Prompt gamma ray spectra for boron samples after background subtraction obtained with $LaBr_3$:Ce detector

The background was determined from the intercept of corrected count vs. concentration plot of the boron data. Figure 3.15 shows dead time corrected and background subtracted counts of four boron samples as a function of boron concentration for boron contaminated water samples. The solid line in Figure 3.15 represents results of calculated yield of prompt gamma-ray obtained from Monte Carlo calculation [31]. There is an excellent agreement between the theoretical yield and experimental yield of prompt gamma-ray from boron measured by $LaBr_3$:Ce detector as a function of boron concentrations in the water samples.

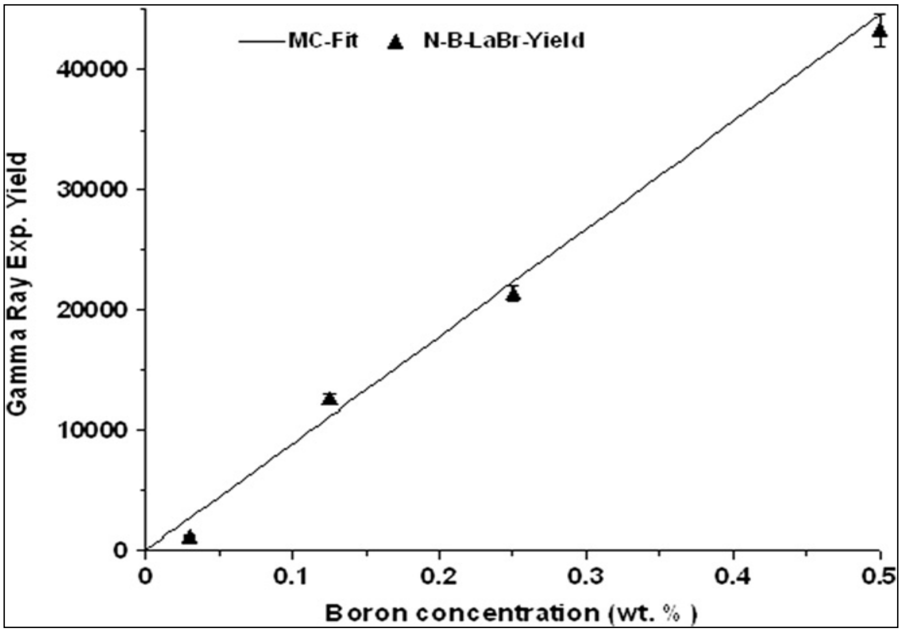

Figure 3.15 Integrated dead time corrected yield of 478 keV prompt gamma-ray of boron from four water samples plotted as a function of boron concentration. The solid line shows normalized-calculated yield of the gamma-rays obtained through Monte Carlo calculations [31].

Figure 3.16 shows the pulse height spectra of prompt gamma rays from water samples containing 0.0625, 0.125, 0.250 and 0.500 wt% cadmium superimposed upon each other along with background spectrum taken without sample. In order to show the effect of increasing concentration of cadmium on the pulse height spectrum, the pulse height spectra for different cadmium concentrations are plotted with a constant vertical offset.

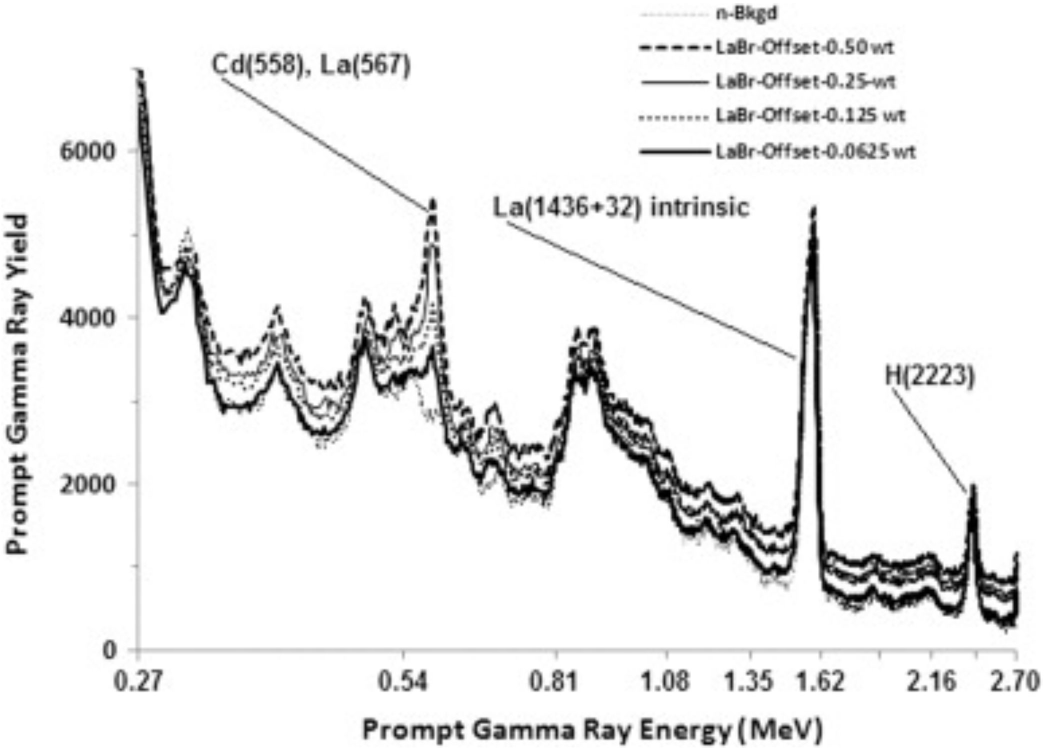

Figure 3.16 Prompt gamma-ray experimental pulse height spectra from water samples containing 0.0625, 0.125, 0.250 and 0.500 wt% cadmium showing different peaks of prompt gamma-rays produced due to the capture of thermal neutrons in the cadmium. In order to show effect of increasing concentration of cadmium on the pulse height spectrum, pulse height spectra for different cadmium concentration are plotted with a constant vertical offset.

Figure 3.17 shows the 558 keV cadmium peak on an enlarged scale to show its interference with the 567 keV peak from activation of lanthanum in $LaBr_3$:Ce detector. Since the cadmium peak contains a contribution from the 567 keV La peak, the difference spectra of cadmium peaks for 0.0625, 0.125, 0.250 and 0.500 wt% concentration were generated by subtracting the background spectrum from each of them.

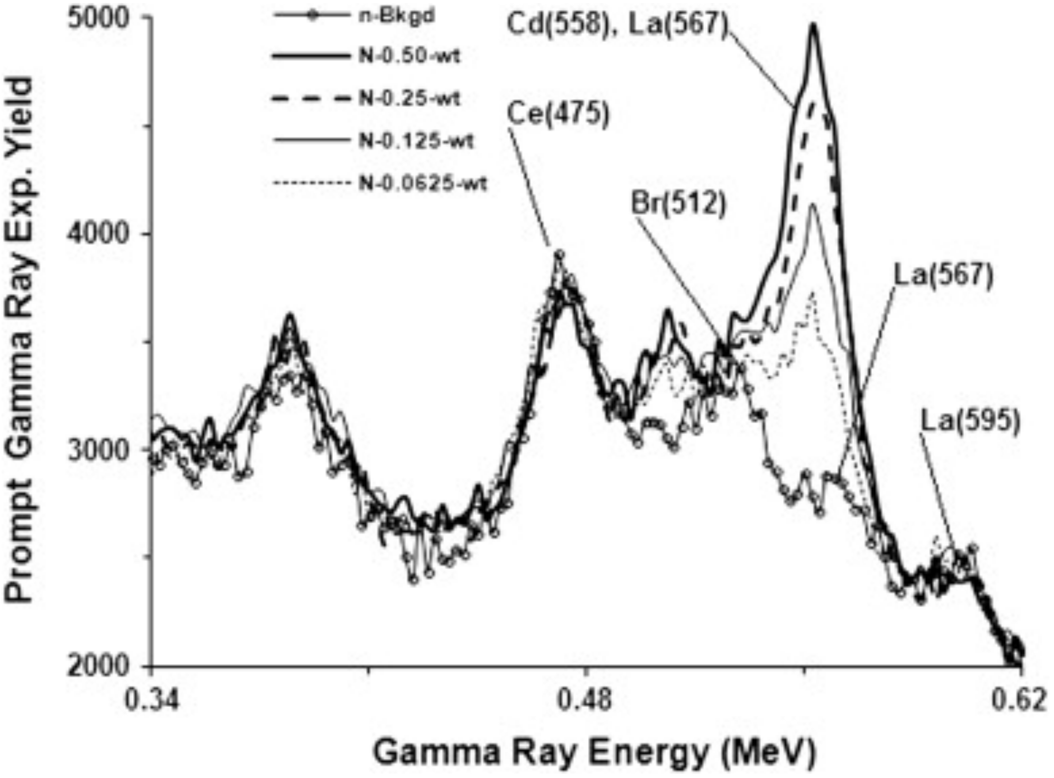

Figure 3.17 Enlarged prompt gamma-ray experimental pulse height spectra of cadmium peak from water samples containing 0.0625, 0.125, 0.250 and 0.500 wt% cadmium showing interference of 558 keV cadmium peak with 567 keV La peak. (The background spectrum taken with pure water sample is also superimposed for comparison).

Figure 3.18 shows difference spectra of cadmium peaks for 0.0625, 0.125, 0.250 and 0.500 wt% cadmium concentrations. They were then integrated, corrected for dead time, and background subtracted following the procedure described for boron samples. Figure 3.19 shows dead time corrected and background subtracted counts of the four cadmium samples as a function of cadmium concentration. The solid line in Figure 3.19 represents results of calculated yield of prompt gamma-rays obtained from Monte Carlo calculations [31]. There is an excellent agreement between the theoretical yield and the experimental yield of prompt gamma-rays from cadmium measured by $LaBr_3$:Ce detector as a function of cadmium concentration in water samples.

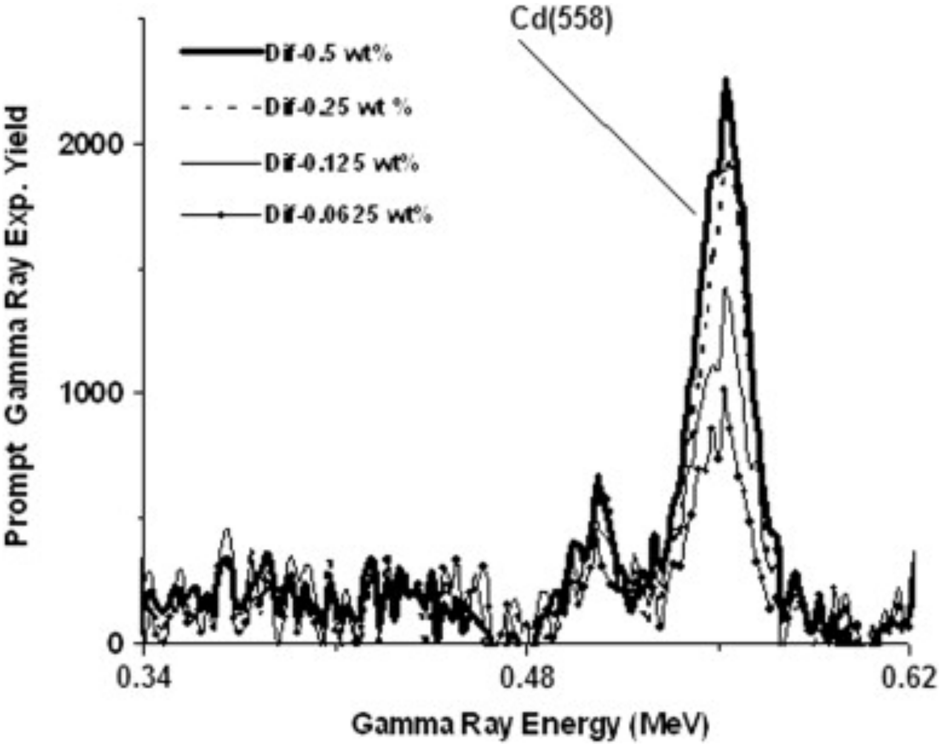

Figure 3.18 Enlarged prompt gamma-ray experimental pulse height spectra after background subtraction from the four cadmium-contaminated water samples.

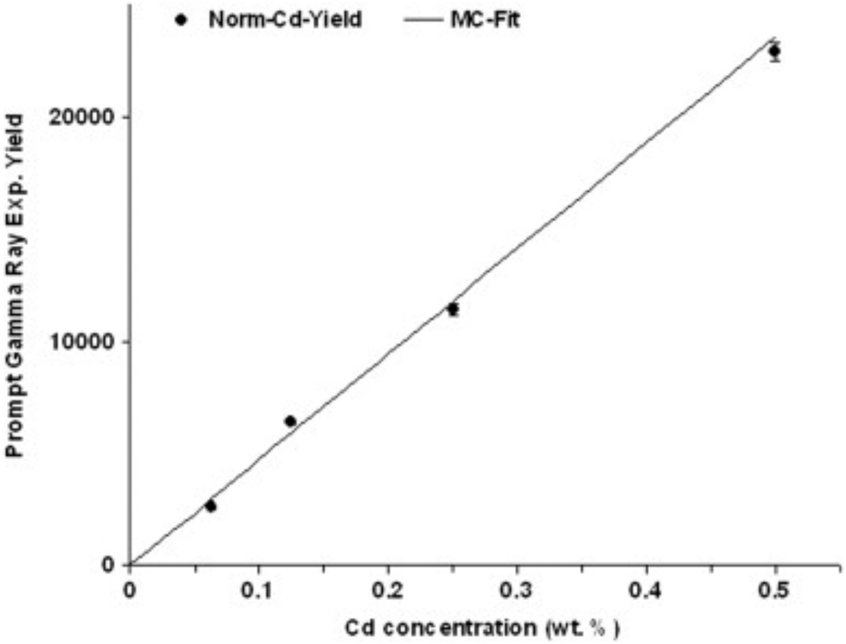

Figure 3.19 Integrated dead time corrected yield of 558 keV prompt gamma-ray of cadmium from four water samples plotted as a function of cadmium concentration. The solid line shows normalized-calculated yield of the gamma-rays obtained from Monte Carlo calculations.

Minimum Detection Limit of Boron and Cadmium in Water Samples for LaBr$_3$:Ce Detector

The minimum detection limit (MDC) of KFUPM portable neutron generator based PGNAA setup was determined from LaBr$_3$:Ce detector tests data following the procedure described in [31]. The MDC for an elemental concentration C measured under a peak with net counts P and associated background counts B (under the peak), where the P and B counts integration are carried out for same channel width and for same time, is defined in [32]

$$MDC = 4.653 \times \left(\frac{C}{P}\right) \times \sqrt{B} \qquad (3.3)$$

where C/P is concentration per counts for a specific gamma ray peak.

The error in MDC is

$$\sigma_{MDC} = \left(\frac{C}{P}\right) \times \sqrt{2B} \qquad (3.4)$$

For 90 mm × 145 mm (diameter × height) cylindrical water sample, minimum detection limit of boron MDC$_B$ and its standard deviation σ_{MDC_B} were calculated to be: $MDC_B = 30.1 ppm$ and $\sigma_{MDC_B} = 9.3 ppm$, while for cadmium we found $MDC_{Cd} = 78.3 ppm$ and $\sigma_{MDC_{Cd}} = 23.8 ppm$.

The results are in agreement with [33] for analysis of cylindrical (with 40 cm diameter × 20 cm height) water samples using a 1 Ci Am-Be source-based PGNAA setup. They have reported minimum detection limits for boron $MDC_B = 1.6 ppm$ and for cadmium $MDC_{Cd} = 6.7 ppm$. Our detection limits for boron and cadmium were larger than those reported in [33] because our sample volume is almost 30 times smaller than the one used in [33]. Our volume sample is 0.88 liters while the sample volume used in [33] is 25.11 liters. For equal sample volume, we could achieve better MDC's than those reported in [33].

3.3.2 LaCl$_3$:Ce Gamma Ray Detector Tests

Boron concentrations in water samples were also measured. The prompt gamma rays produced from the B and Cd samples were detected by 3 inches by 3 inches (diameter x length) LaCl$_3$:Ce detector. For each run the data was taken for 25 minutes. The same setup and procedure described earlier in section 3.3.1 were utilized in this part of the study.

Prompt Gamma-Ray Measurements of Boron and Cadmium in Water Samples

Figure 3.20 shows the pulse height spectra of prompt gamma-rays from water samples containing 0.031, 0.125, 0.250 and 0.5 wt. % boron superimposed upon each other along with background spectrum taken with pure water sample.

In order to show the effect of increasing concentration of boron on the pulse height spectrum, the pulse height spectra for different boron concentrations are plotted with a constant vertical offset. The 478 keV boron gamma-ray peak along with the intrinsic (1436+32 keV) activity peak are quite prominent.

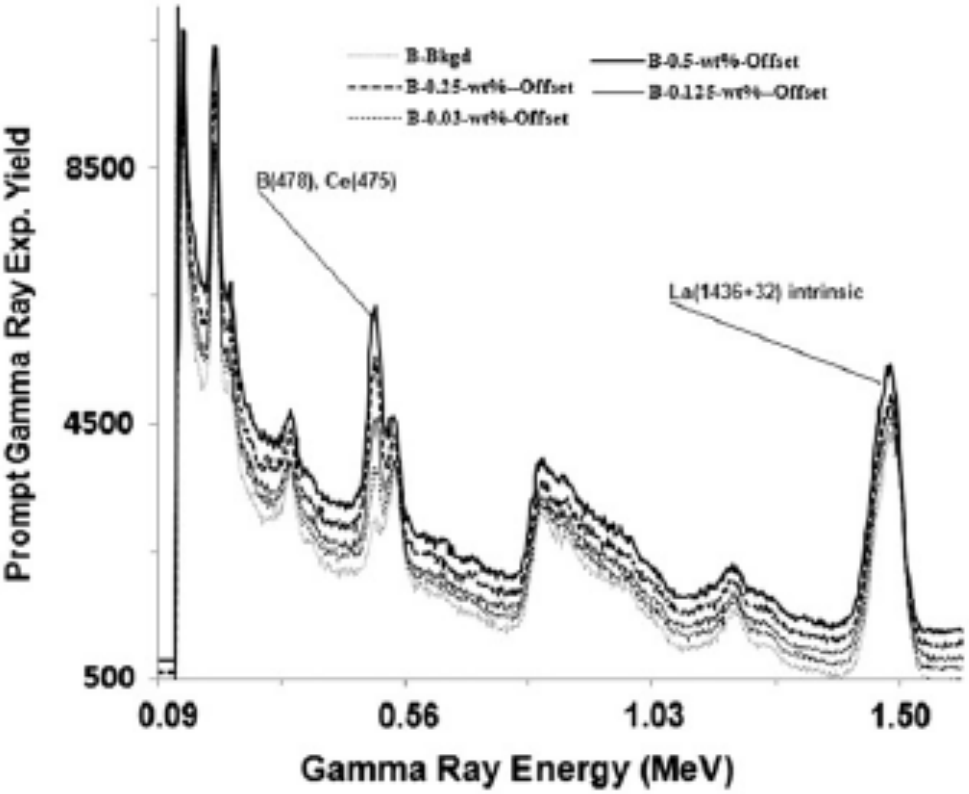

Figure 3.20 Prompt gamma-rays pulse height spectra of four boron-contaminated water samples containing 0.031, 0.125, 0.250 and 0.50 wt. % boron, along with background spectrum taken with pure water sample, plotted with a constant vertical offset.

Figure 3.21 shows the 478 keV boron peak on an enlarged scale to show its interference with the 475 keV peak from activation of cerium in $LaCl_3$:Ce detector. Since the boron peaks contain a contribution from the Ce (475 keV) peak, the difference spectra of boron peaks for 0.031, 0.125, 0.250 and 0.500 wt.% concentrations were generated by subtracting the background spectrum from each of them.

Figure 3.22 shows the difference spectra of the boron peaks. Finally, the peaks of the difference boron spectra were integrated to generate the integrated boron gamma yield as a function of boron concentration. Similarly the pulse height spectra of prompt gamma rays from water samples containing 0.0625, 0.125, 0.250 and 0.500 wt. % cadmium were analyzed through difference spectra and were integrated to generate the integrated cadmium gamma yield as a function of cadmium concentration.

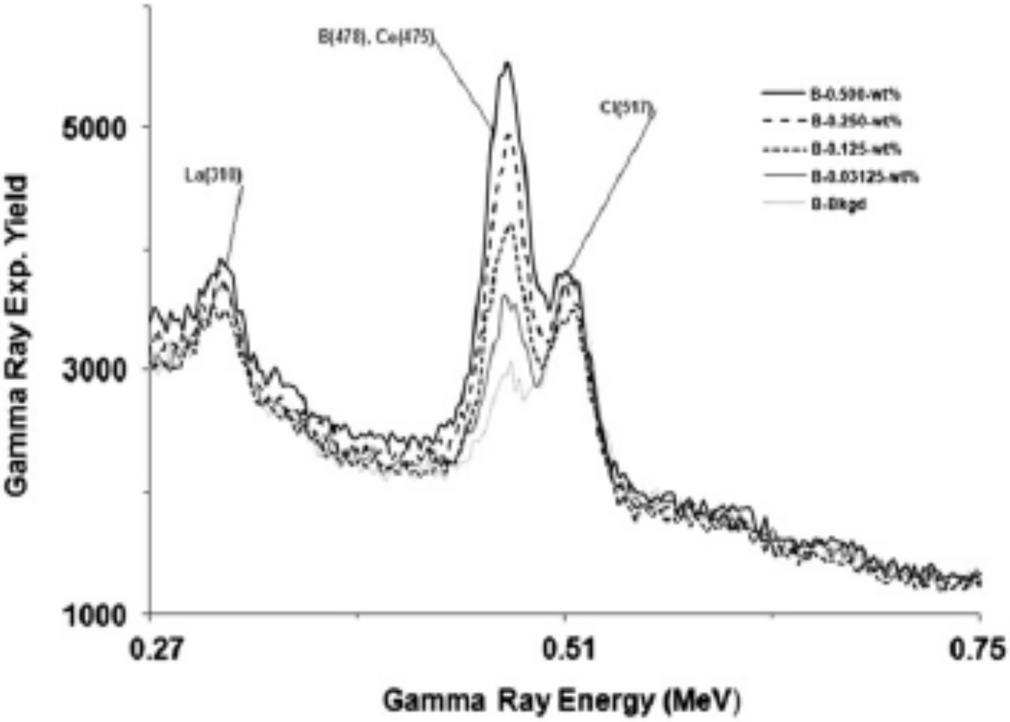

Figure 3.21 Enlarged prompt gamma-ray experimental pulse height spectra of water samples containing 0.031, 0.125, 0.250 and 0.5 wt % boron, along with background pure water sample, showing interference of the 478 keV boron peak with the 475 keV Ce peak.

The integrated boron and cadmium gamma ray yield data was corrected for dead time and neutron flux fluctuation using the neutron monitor counts for each boron and cadmium concentration peak. Figure 3.23 shows the dead time corrected and background subtracted counts of four cadmium and boron samples as a function of cadmium and boron concentration in the contaminated water samples respectively. The lines in Figure 3.23 represent results of calculated yield of boron and cadmium prompt gamma-rays obtained from Monte Carlo calculations following the procedure described earlier in section 3.1. There is an excellent agreement between the theoretical and experimental yields of prompt gamma-ray from boron and cadmium-contaminated water samples.

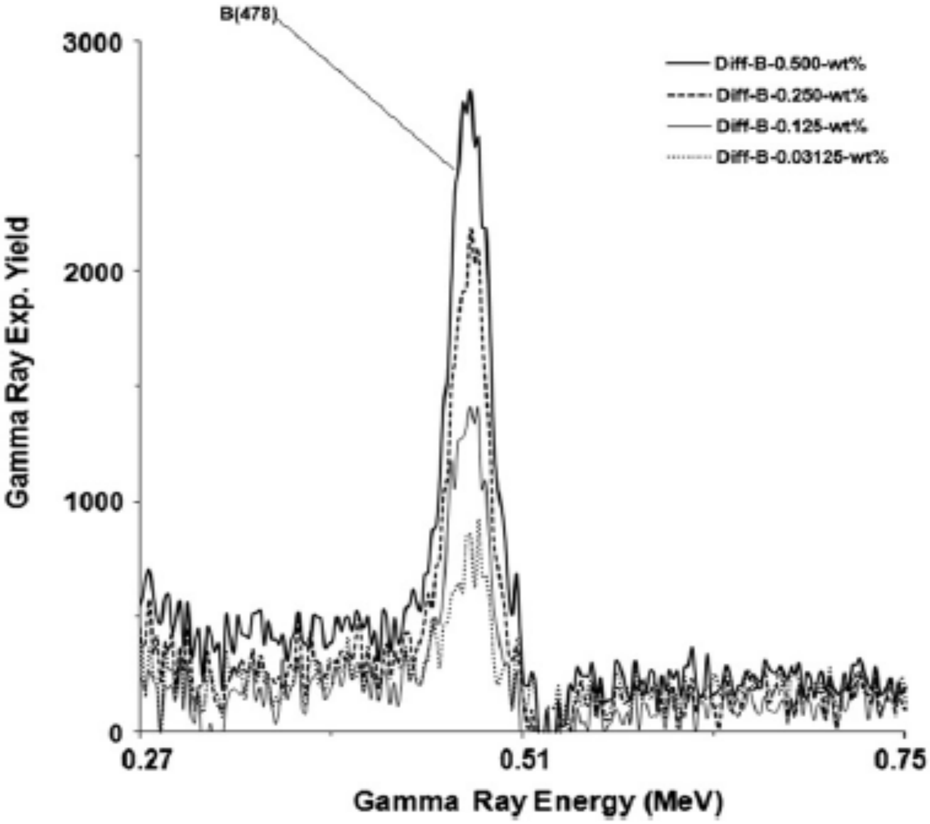

Figure 3.22 Enlarged prompt gamma-ray experimental pulse height spectra after background subtraction from the four boron-contaminated water samples.

Finally the minimum detection limit (MDC) of boron and cadmium in water for the LaCl$_3$:Ce detector was also calculated using the procedure described in section 3.3.1. For 90 mm × 140 mm (diameter × height) cylindrical water samples, the minimum detection limit of boron $MDC_B = 104 \pm 32\ ppm$ was calculated from 0.5 wt % B data with net counts $P_B = 70915$, background counts $B_B = 100270$ and using equation (3.3).

Similarly minimum detection limit of cadmium $MDC_{CD} = 130 \pm 32\ ppm$ was calculated from 0.5 wt % Cd data with $P_{CD} = 34417$, $B_{CD} = 36942$ and using equation (3.3). The MDC values of boron and cadmium agree with each other within statistical uncertainty.

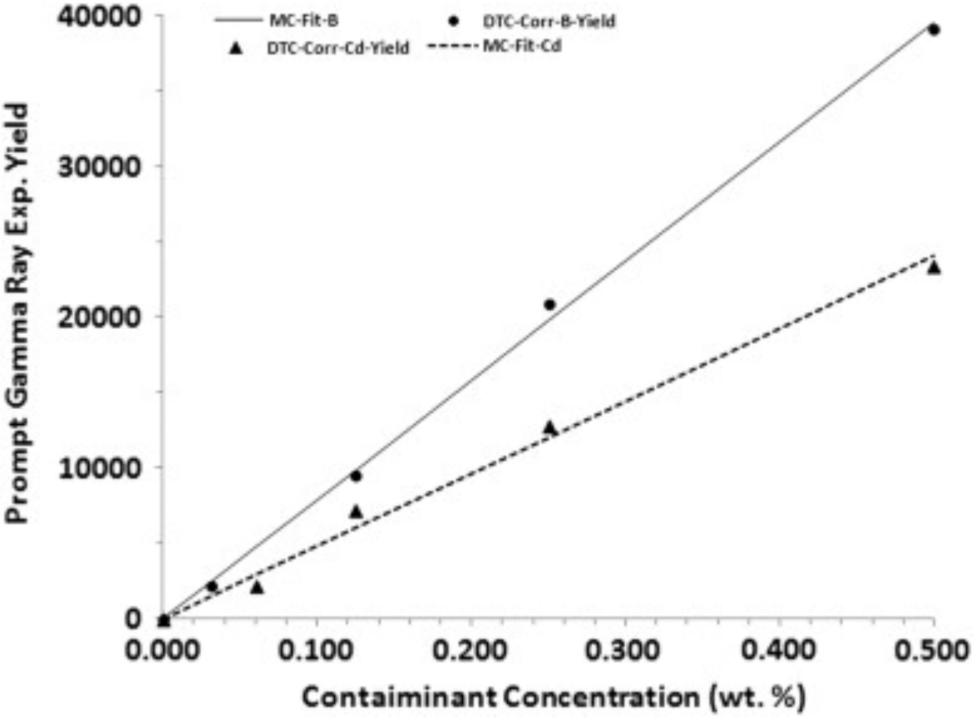

Figure 3.23 Dead time corrected integrated yield of 478 and 558 keV prompt gamma-ray of boron and cadmium, respectively, from four contaminated water samples plotted as a function of contaminant concentration. The solid line shows normalized-calculated yield of the gamma-rays obtained through Monte Carlo calculations.

3.3.3 BGO Gamma Ray Detector Tests

A thermal neutron capture-based Prompt Gamma ray Activation Analysis setup has been designed separately to test BGO (bismuth germinate) detector using a D(d,n) reaction-based portable neutron generator. The performance of the setup was tested through mercury concentration measurements in Hg-contaminated water samples.

Figure 3.24 shows a schematic of the portable neutron generator-based PGNAA setup. It consists of a cylindrical sample container placed in a cylindrical cavity drilled through a cylindrical High Density Polyethylene (HDPE) moderator. A cylindrical gamma-ray detector (BGO), with its longitudinal axis aligned along the sample's longitudinal axis detects the prompt gamma rays from the top-side of the sample.

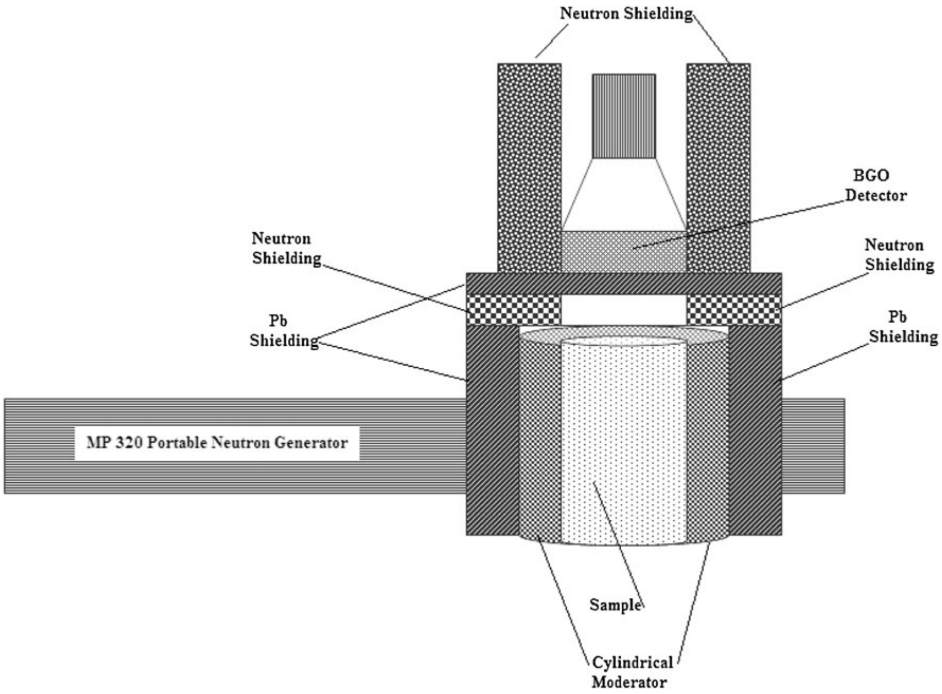

Figure 3.24 Schematic side view of the portable neutron generator based PGNAA setup

The moderator is placed adjacent to the neutron target plane of the portable neutron generator. In order to prevent undesired gamma-rays and neutrons from reaching the detector, 3 mm thick lead shielding and 50 mm thick neutron shielding surround the BGO detector. The neutron shielding is made of a mixture of paraffin and lithium carbonate mixed in equal weight proportions.

Four Hg-contaminated water samples with 1.25, 2.50, 5.00, and 10.0 wt% Hg concentrations were prepared. The water samples were then irradiated in a pulsed beam of 2.5 MeV neutrons produced with a 70 keV deuteron beam. The deuteron pulse had a width of 5 ms and a frequency of 250 Hz. The pulsed neutron beam improved the signal to background ratio in the PGNAA studies. A typical beam current of the generator was 70 μA. The prompt gamma-ray data from Hg-contaminated water samples were acquired using a cylindrical 125 x 125 mm (diameter x height) BGO detector for 25 min. Due to its radiation resistant property against neutron damage; BGO was selected as a gamma ray detector. During irradiation of the samples, the BGO detector, although well shielded, was also exposed to thermal neutrons and it registered the prompt gamma rays due to the capture of thermal neutrons in Bi and Ge elements present in the detector. There might be interferences from other elements present in the environmental samples in this energy but due to large thermal capture cross section of Hg, very small contamination of Hg will be still detectable in spite of those interferences. The energies and intensities of prominent prompt gamma-rays due to capture of thermal neutrons in the detector material and Hg are listed in Table 3.4.

Element	Gamma-ray energy (keV)	$\sigma_\gamma^Z(E_\gamma)$-barns
Bi	162	0.008
	320	0.0115
	674	0.0026
	2505	0.0021
	2828	0.00179
	4054	0.0137
	4171	0.0171
Ge	175	0.164
	493	0.133
	500	0.162
	596	1.100
	608	0.250
	868	0.553
	961	0.129
	1101	0.134
	1204	0.141
	1472	0.083

Element	Gamma-ray energy (keV)	$\sigma_\gamma^Z(E_\gamma)$-barns
Hg	368	251
	1570	29.6
	1693	56.2
	2002	24.3
	2639	11.6
	3186	11.3
	3289	13.3
	4675	13
	4739	30
	4759	12.5
	4842	20
	5050	20
	5658	27.5
	5967	62.5
	6458	23

Table 3.4: Energies and partial elemental cross section $\sigma_\gamma^Z(E_\gamma)$-barns of prominent capture gamma-rays of bismuth, germanium and mercury [23].

Prompt gamma-ray measurements of Hg-contaminated Water samples

Figures 3.25, 3.26 and 3.27 show the pulse height spectra of the BGO detector from water samples contaminated with mercury. Figure 3.25 shows the pulse height spectra of prompt gamma rays from water samples containing 1.25, 2.50, 5.00, and 10.0 wt% Hg concentrations superimposed upon each other along with the background spectrum taken with non-contaminated demineralized water sample. Figure 3.25 also shows the 2.22 MeV hydrogen capture peak from the moderator material along with 2.64, 3.19-3.29, and 4.67–5.05 MeV prompt gamma ray peaks from mercury in the contaminated water.

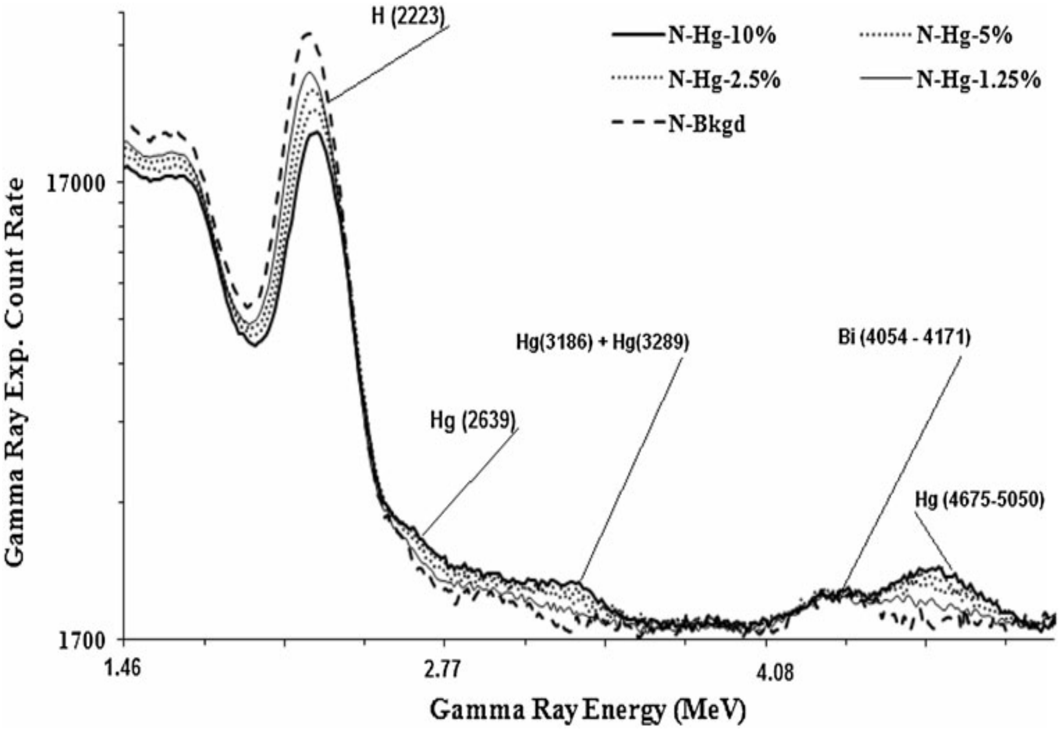

Figure 3.25 Prompt gamma-ray experimental pulse height spectra from mercury contaminated water sample containing 1.25, 2.50, 5.00, and 10.0 wt% mercury showing 2.64, 3.19 - 3.29, and 4.67–5.05 MeV prompt gamma rays peaks of mercury also superimposed is the background gamma-ray spectrum

Moreover, Figure 3.25 also shows unresolved prompt gamma ray peaks at 4.06–4.25 MeV energies from bismuth in BGO detector material. The BGO detector has poor energy resolution (11 % for 662 keV gamma-rays from Cs-137 source).

Figure 3.26 shows enlarged prompt gamma rays pulse height spectra of the four Hg-contaminated water samples over 2.51–5.14 MeV gamma energy range, showing an increase in intensity of 2.64, 3.19 - 3.29, and 4.67–5.05 MeV Hg prompt gamma ray peaks for increasing Hg concentration in the water samples.

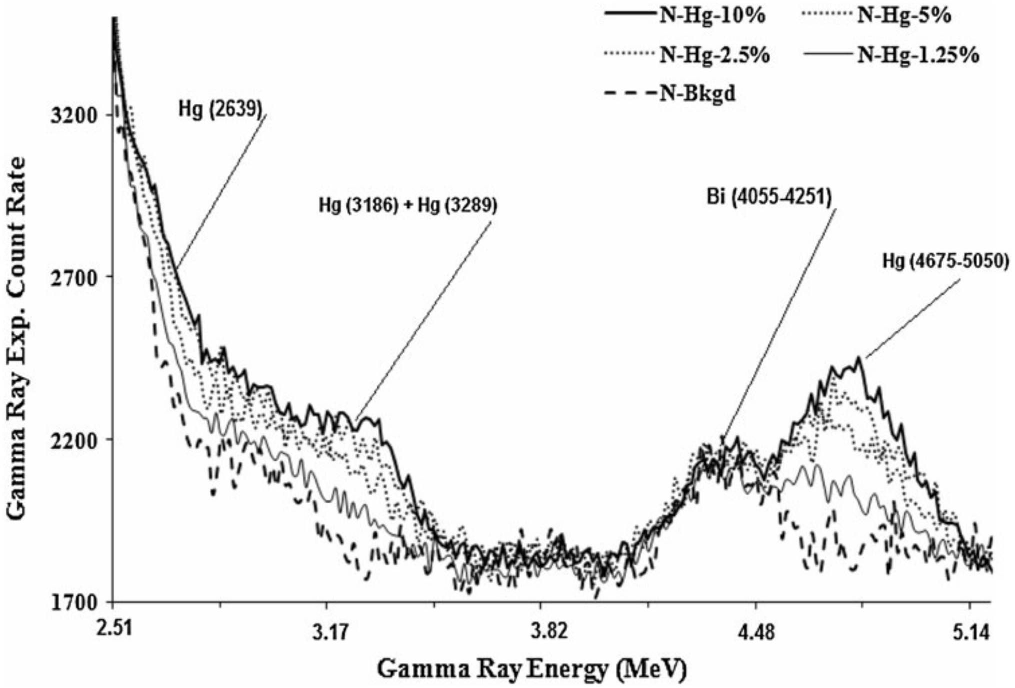

Figure 3.26 Enlarged prompt gamma-ray experimental pulse height spectra from 1.25, 2.50, 5.00, and 10.0 wt% mercury contaminated water sample over 2.51–5.14 MeV showing 2.64, 3.19 - 3.29, and 4.67–5.05 MeV prompt gamma rays peaks of mercury

Figure 3.27 shows the difference spectra showing well resolved peaks of 2.64, 3.19 - 3.29, and 4.67–5.05 MeV prompt gamma rays of Hg for the four samples containing 1.25, 2.50, 5.00, and 10.0 wt% Hg concentrations. These spectra were obtained after subtracting the background spectrum from each sample pulse height spectrum.

Finally, the peaks of the difference spectra were integrated to generate integrated count rates of 2.64, 3.19-3.29, and 4.67–5.05 MeV prompt gamma ray peaks of Hg as a function of mercury concentration, as shown in Figure 3.28. The solid lines in Figure 3.28 represent the results obtained from Monte Carlo calculations following the procedure described in section 3.1.

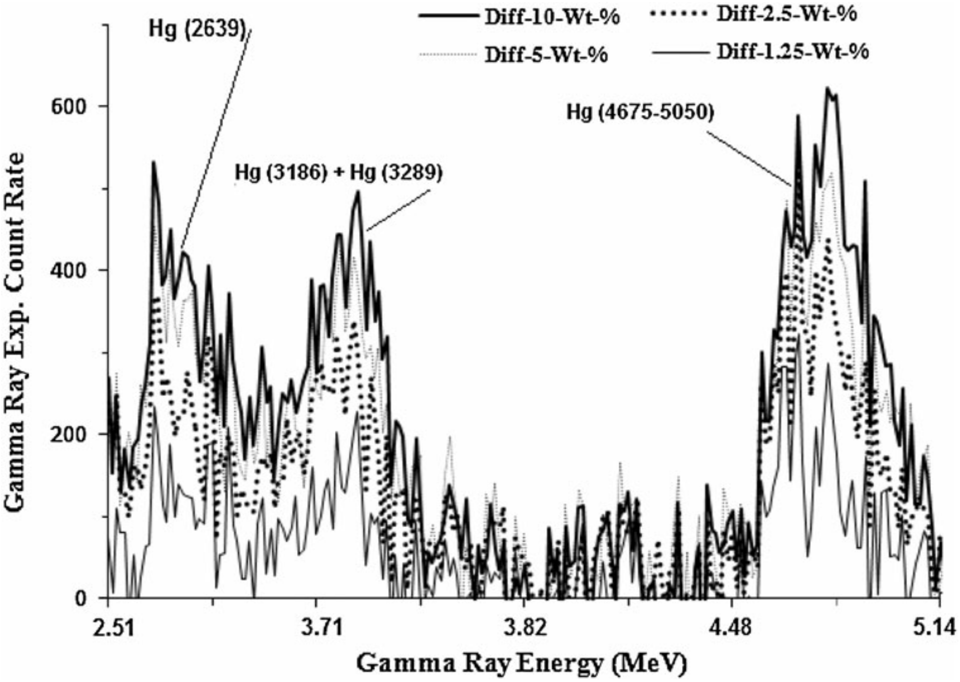

Figure 3.27 Enlarged mercury prompt gamma-ray pulse height difference spectra for water samples containing 1.25, 2.50, 5.00, and 10.0 wt% mercury after background subtraction over 2.51–5.14 MeV and showing 2.64, 3.19-3.29, and 4.67–5.05 MeV mercury peaks

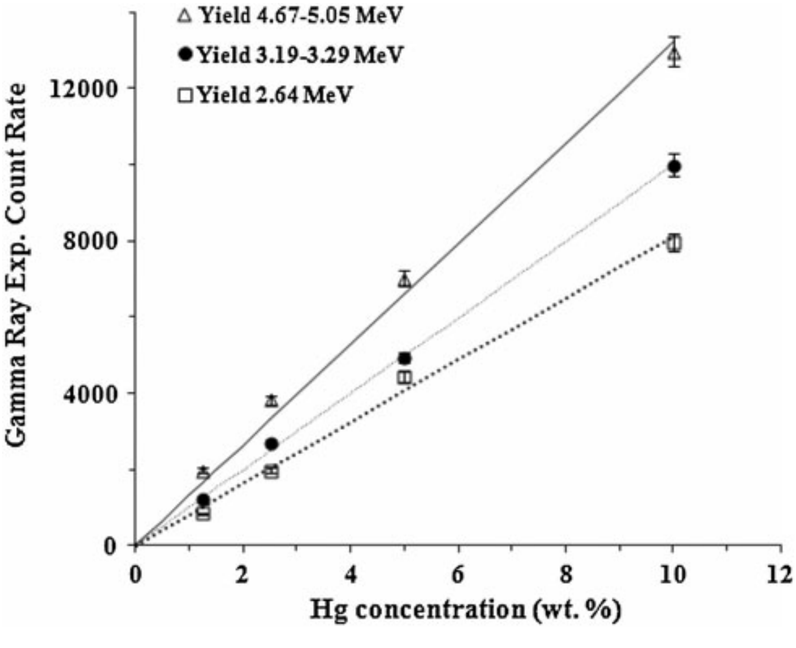

Figure 3.28 Experimental integrated count rate of 2.64, 3.19-3.29, and 4.67–5.05 MeV prompt gamma-rays from mercury plotted as a function of mercury concentration in water samples. Lines represent the results of the Monte Carlo simulations

Each gamma ray line has a different slope of count rate versus Hg-concentration. The slope of the line defines the minimum detectable activity (MDA) of the PGNAA setup for the specific element using that particular gamma line. The maximum value of the slope observed in the present study is for the 4.67–5.05 MeV line. The MDA of Hg for high energy gamma rays studied in this study is expected to be quite poor as compared to that obtained using high-intensity, low-energy 386 keV Hg gamma ray. The MDA of Hg using 2.6–5.1 MeV gamma rays for the portable neutron generator based PGNAA setup was calculated to be 0.19 ± 0.06 wt%. For 386 keV Hg gamma ray, with two order of magnitude larger production cross section, the corresponding MDA is expected to be about 19 ppm. There is an excellent agreement between the theoretical count rate and the experimental count rate of prompt gamma-rays from mercury measured by a BGO detector as a function of Hg concentration in the water samples.

3.4 Measurement of Chlorine Concentrations in Saline Water Samples

The efficacy of neutron flux from the MP320 generator for its application in prompt gamma-ray analysis of bulk samples was tested through salinity measurements in water samples using the PGNAA setup. Prompt gamma-ray yield of chlorine was calculated from saline water samples contained in plastic bottles having 90 mm diameter and 140 mm length. The saline water samples were prepared by mixing water with sodium chloride containing 1.0, 1.5, 2.0, 2.5, 3.0, 3.5 and 4.0 wt.% chlorine. The saline water was chosen to test neutron flux efficacy because of the large thermal neutron capture cross section of chlorine, as shown in Table 3.5 [23].

The saline water samples were irradiated in the MP320 based PGNAA setup. The pulsed deuteron beam with 60 keV energy and 60 μA beam current had a pulse width of 5 ns and a frequency of 250 Hz. The prompt gamma-rays produced in saline water samples were detected by a 125 mm by 125 mm (diameter x length) BGO detector. The prompt gamma-ray data were acquired for a preset time of 25 minutes.

As shown in Table 3.5 [23] there are several prompt gamma-rays emitted by chlorine due to capture of thermal neutrons. Some of them have energies that cannot be resolved by the BGO detector with 11% energy resolution.

Element	**Gamma-rays energy (MeV)**	**$\sigma_\gamma^z(E_\gamma)$-barns**
Cl	1.164	8.91
	1.951	6.33
	1.959	4.10
	2.863	1.82
	3.062	1.13
	4.98	1.23
	5.715	1.82
	6.110	6.59
	6.619	2.53
	6.627	1.47
	7.413	3.29
	7.790	2.66

Table 3.5 Energies and partial elemental cross section $\sigma_\gamma^z(E_\gamma)$-barns of prominent capture gamma rays of chlorine [23].

The unresolved pairs of gamma-rays have the energies: 1.951 and 1.959 MeV; 2.863 MeV and 3.062 MeV and 6.619 and 6.627 MeV. In this study, chlorine prompt gamma-rays with 3.06 (2.863-3.062), 4.98, 5.72, 6.11, and 6.63 (6.619 - 6.627) MeV energies were analyzed.

Figure 3.29 shows the experimental pulse height spectra of prompt gamma-rays from saline water samples over 1.18-8.32 MeV, exhibiting prompt gamma-ray peaks at 2.86-3.06, 4.98, 5.72, 6.11 and 6.62-6.63 MeV.

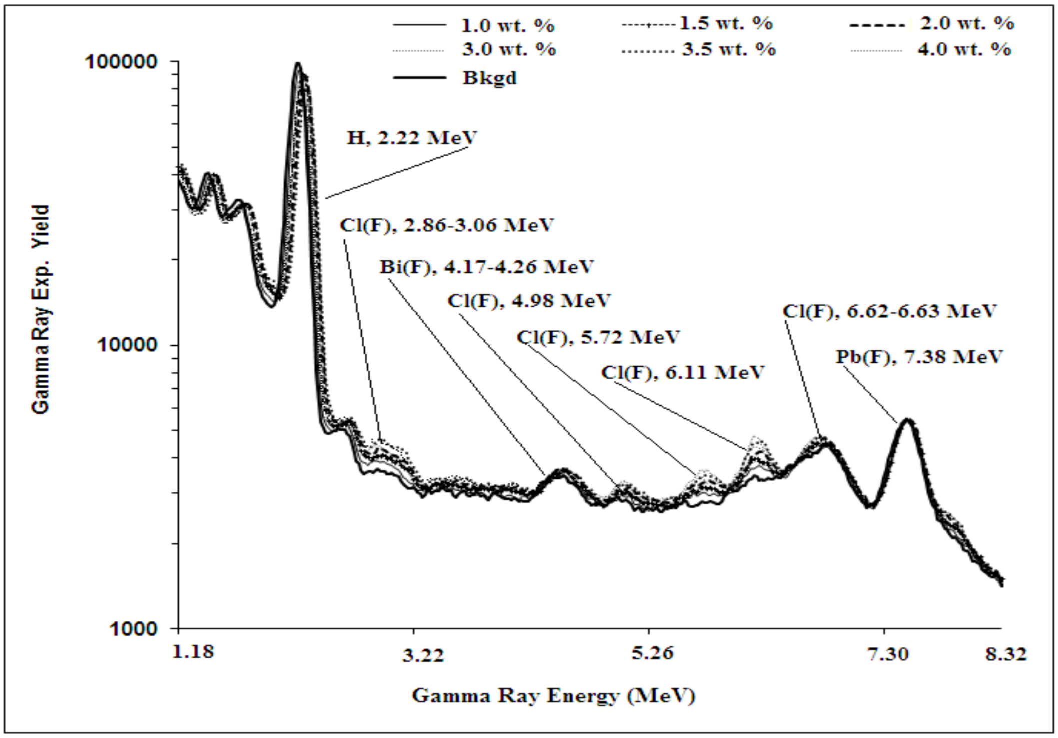

Figure 3.29 Prompt gamma-rays experimental pulse height spectrum from saline water samples over 1.18-8.32 MeV showing different peaks of prompt gamma-rays produced due to capture of thermal neutrons in the chlorine sample.

Figure 3.30 shows gamma-ray pulse height spectra over 2.81 to 7.71 MeV energies from saline water samples containing 1.0, 1.5, 2.0, 3.0, 3.5, and 4.0 wt.% chlorine. Also superimposed on the spectra is the background gamma-ray spectrum.

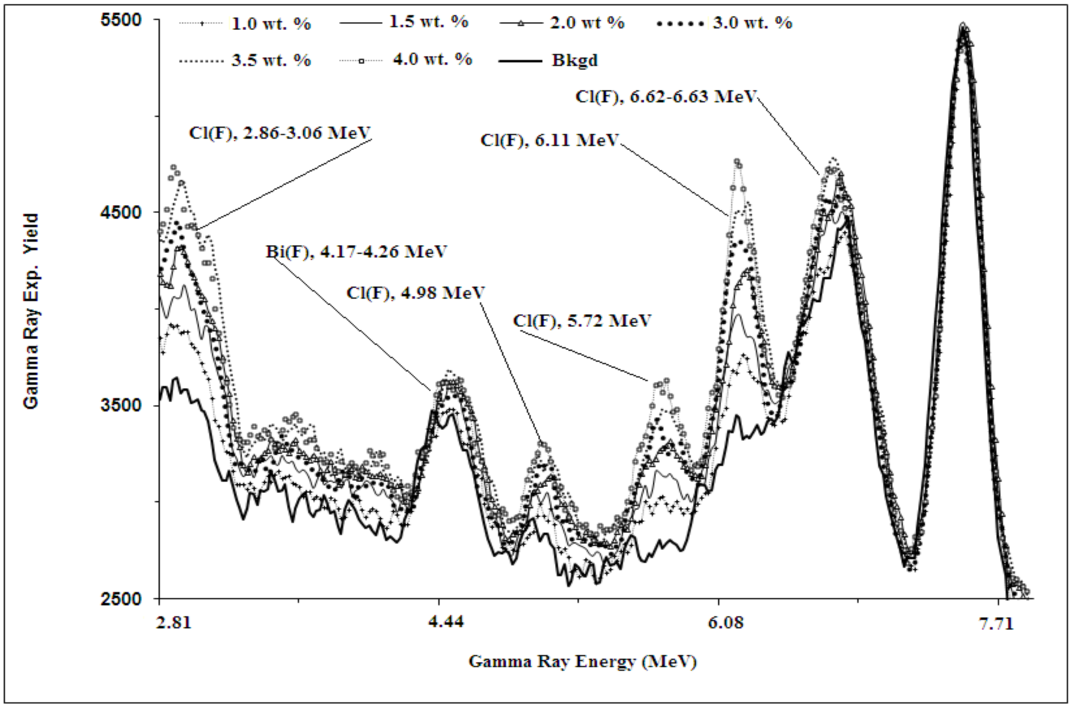

Figure 3.30 Prompt gamma-rays experimental pulse height spectra from saline water samples over 2.81-7.71 MeV showing chlorine peaks from water samples containing 1.0, 1.5, 2.0, 3.0, 3.5, and 4.0 wt % chlorine. Also superimposed is the background gamma-ray spectrum

An increase in the peak intensity of chlorine prompt gamma-ray with increasing chlorine concentration is clearly exhibited in the pulse height spectra of the water samples. In order to extract the prompt gamma-ray yield as a function of the chlorine concentration, the difference spectra were generated after subtracting the background spectrum from the pulse height spectra of saline water samples.

Figure 3.31 shows the difference pulse height spectra of prompt gamma-rays over 2.57 to 7.15 MeV from saline water samples containing 1.0, 1.5, 2.0, 3.0, 3.5, and 4.0 wt % chlorine. The chlorine prompt gamma-ray peaks corresponding to 3.06 (2.86-3.06), 4.98, 5.72, 6.11, and 6.63 (6.62-6.63) MeV energies are quite prominently shown in Figure 3.31. Finally, the counts under each peak were integrated to obtain gamma-ray integrated yields. The gamma-ray yields were further normalized to the same incident fast neutron flux on the sample. Since chlorine prompt gamma ray intensity is directly proportional to chlorine concentration in the sample, the integrated yield of chlorine prompt gamma rays of any particular energy will also be linearly proportional to the chlorine concentration in the sample.

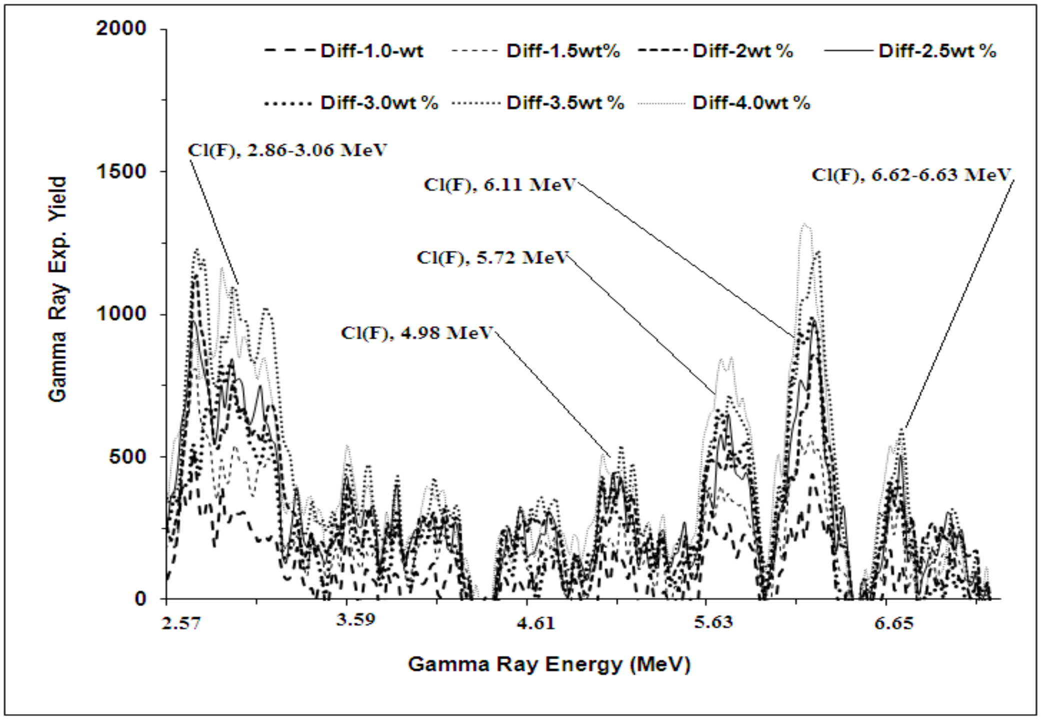

Figure 3.31 Prompt gamma-rays difference pulse height spectra from chlorinated water samples containing 1.0, 1.5, 2.0, 3.0, 3.5, and 4.0 wt % chlorine. The spectra were generated after background subtraction

Experimental normalized yield of 3.06, 5.72, 6.11, and 6.63 MeV prompt gamma-rays from chlorine are plotted in Figure 3.32 as a function of the chlorine concentration and they exhibit a linear correlation with the chlorine concentration.

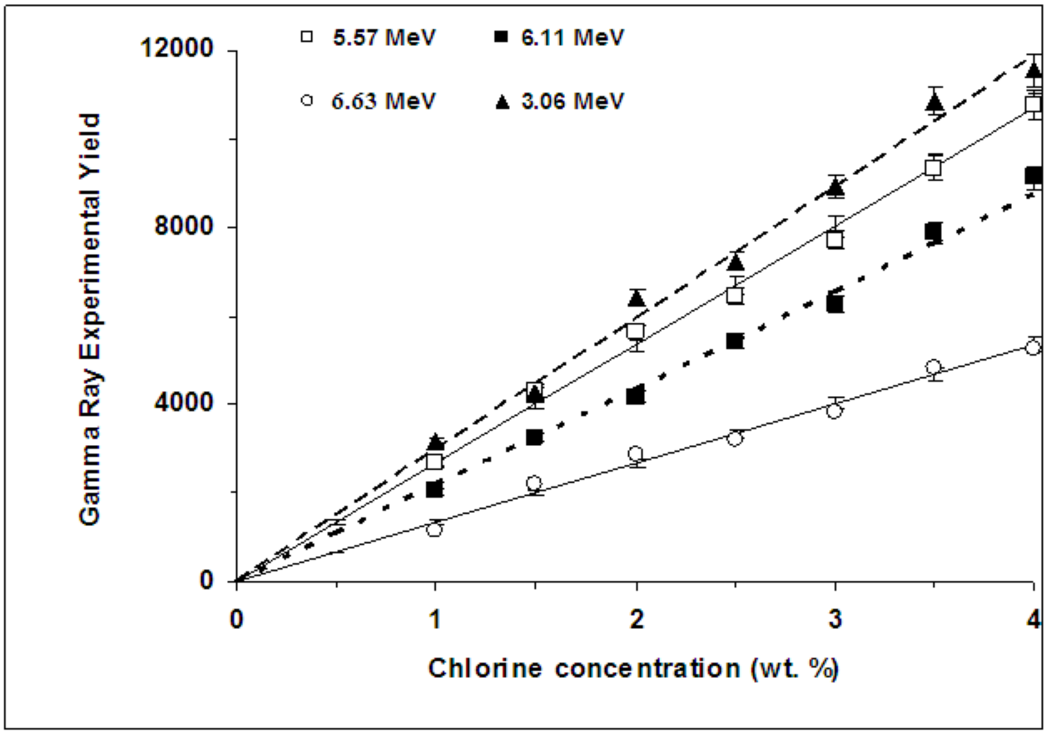

Figure 3.32 Experimental integrated yields of 3.06, 5.72, 6.11, and 6.63 MeV prompt gamma-rays from chlorine potted as a function of chlorine concentration. Lines represent the results of Monte Carlo simulations.

CHAPTER 4

H, C AND O ANALYSIS OF BULK SAMPLES USING 14 MeV NEUTRON INELASTIC SCATTERING

Prompt gamma ray tests of cylindrical lanthanum halides ($LaBr_3$:Ce & $LaCl_3$:Ce) gamma ray detectors have been carried out for the measurement of Hydrogen, Carbon and Oxygen (H, C, O) concentrations in bulk samples via inelastic scattering of neutrons (NIS) using a 14 MeV neutron based PGNAA setup. Inspite of its intrinsic activity, the LaBr3:Ce detector showed superior performance than the BGO detector for the measurement of Hydrogen, Carbon and Oxygen concentrations in benzene, water, toluene, propanol, ethanol and methanol bulk samples. The BGO detector has a large concentration of oxygen in its detector material and is consequently less sensitive for oxygen detection in bulk samples. Hence, it is not a suitable choice for oxygen determination in bulk samples.

4.1 Calibration Measurements of PGNAA Setup

H, C and O bulk samples comprising benzene, toluene, propanol, ethanol and methanol were analyzed in this part of the study through prompt gamma rays using LaBr3:Ce, $LaCl_3$:Ce and BGO gamma ray detectors. The analysis was done utilizing a common setup for the three detectors used. The setup was built around the zero-degree beam line of the 350 keV accelerator [34]. The geometry of the 14 MeV neutron based PGNAA setup used in the present study is shown in Figure 4.1. It mainly consists of a cylindrical sample (90 mm x 145 mm) placed 7.0 cm away from a tritium target at a 0^o angle with respect to the 14 MeV neutron beam. The gamma ray detector is placed at a center-to-center distance of 1.9 cm from the sample at an angle of 90 degrees with respect to the 14 MeV neutron beam. Tungsten blocks are inserted between the neutron target and the gamma ray detector to shield it from the direct beam of 14 MeV neutrons, the detector was also shielded from 14 MeV neutron-induced gamma ray background through massive lead shielding inserted between the detector and the tungsten shield. Finally a paraffin structure was built next to the tungsten blocks to shield the detector from room scattered neutrons. The paraffin shield was prepared by mixing lithium carbonate and paraffin wax in equal weight proportions. The paraffin and lead shield was quiet effective in shielding the detector against scattered neutrons and background gamma rays. However, the gamma ray peaks in the background spectrum due to inelastic scattering of 14 MeV neutrons from lead and paraffin shielding were quite pronounced.

A pulsed beam of 14 MeV neutrons was produced via the T(d,n) reaction using a pulsed deuteron beam with 200 nano-sec width and a frequency of 31 kHz. A typical pulsed deuteron beam current was 60 μA DC. The fast neutron flux from the tritium target was monitored using a cylindrical 76 mm x 76 mm (diameter x height) NE213 fast neutron detector, placed at a distance of 1.8 m from the target and at a backward angle of 130 degrees with respect to the beam axis on the opposite side of the $LaBr_3$:Ce gamma ray detector. The prompt gamma-rays produced in the sample were recorded for a preset number of fast neutrons recorded by NE213 monitor.

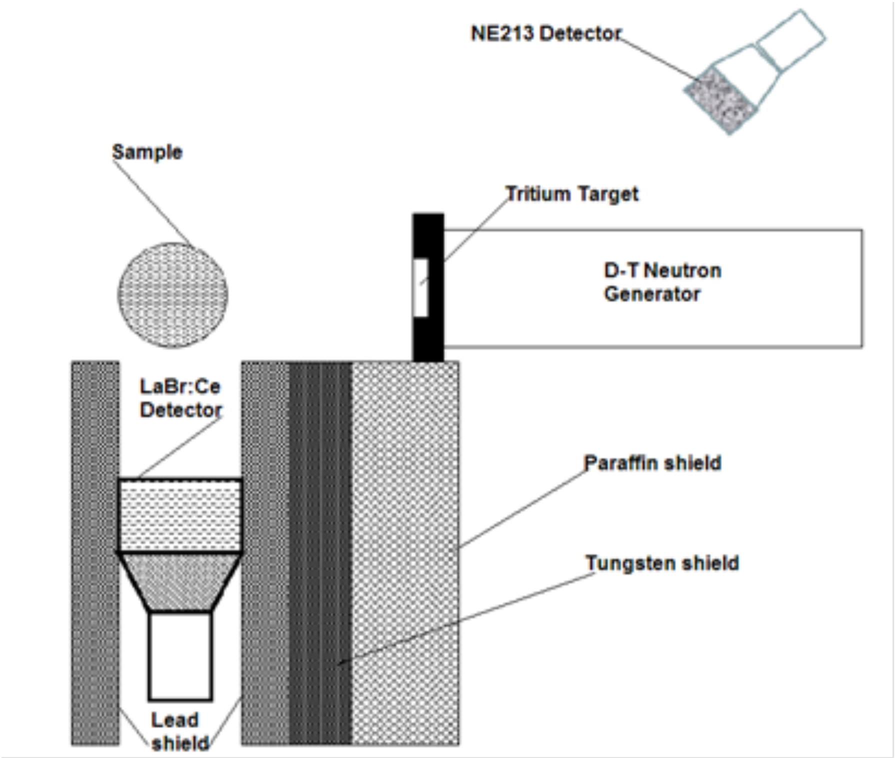

Figure 4.1 Schematic of 14 MeV neutron-based setup used for measurement of H, C and O concentration in bulk samples

4.1.1 Calibration Measurements Using $LaBr_3$:Ce & BGO Detectors

The $LaBr_3$:Ce detector gamma ray response was measured for prompt gamma rays produced in inelastic scattering of 14 MeV neutrons from H, C and O present in Propanol, Methanol, Water, Benzene and Ethanol samples, as shown in Table 4.1. The H, C and O concentrations in those samples were independently measured at the Atomic Absorption Spectrometry Laboratory of the Department of Chemistry, King Fahd University of Petroleum and Minerals. The samples were then irradiated in the 14 MeV neutron-based PGNAA setup. The prompt gamma-ray data from the samples were acquired for a preset amount of time using a Multichannel Buffer-based data acquisition system. The neutron flux during each run was stored as a NE213 detector spectrum taken at half Cs pulse height bias and was used later for neutron flux normalization during data correction.

Compounds	Chemical Formula	Mol.-wt	C(wt%)	O(wt%)	H(wt%)
Propanol	C_3H_8O	60	60.0	26.7	13.3
Methanol	CH_2O	30	40.0	53.3	6.7
Water	H_2O	18	-	87.8	11.4
Benzene	C_6H_6	78	92.3	-	7.7
Toluene	C_7H_8	92	91.3	-	8.7
Ethanol	C_2H_6O	46	52.2	34.8	13.0

Table 4.1 Elemental composition of the Propanol, Methanol, Benzene and Ethanol samples

Figures 4.2 - 4.4 show pulse height spectra of high energy prompt gamma-rays from propanol, methanol, water and benzene samples taken with the $LaBr_3$:Ce detector. Figure 4.2 shows full spectrum of the detector while Figures 4.3 and 4.4 show its enlarged portions. Also superimposed in the spectrum is the detector background spectrum taken with an empty container. Figure 4.2 shows the pulse height spectra of gamma ray peaks over 0.30-7.74 MeV from inelastic scattering of 14 MeV neutrons from hydrogen, carbon and oxygen in propanol, methanol, water and benzene samples along with lead shielding.

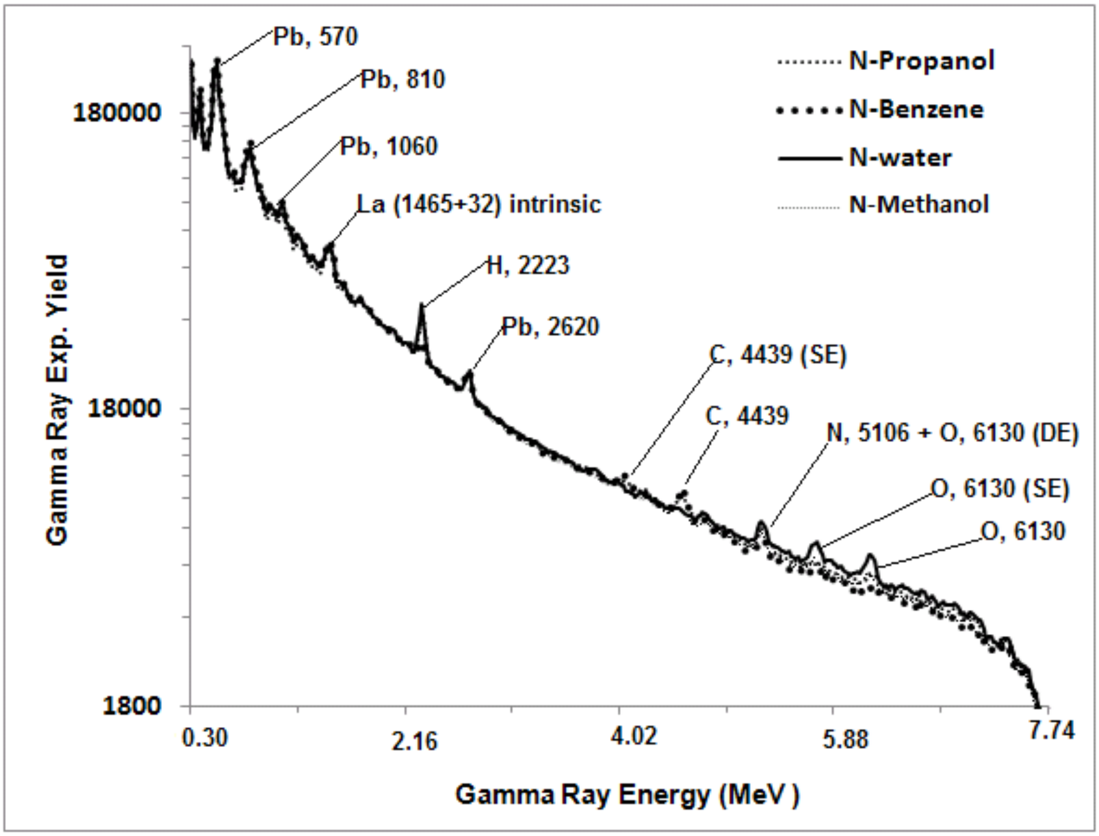

Figure 4.2 Full prompt gamma ray spectra of $LaBr_3$:Ce gamma ray detector for benzene, propanol, water and methanol samples, taken with 14 MeV neutrons PGNAA setup

As reported in the literature [44], the gamma rays due to inelastic scattering of 14 MeV neutrons from lead were detected at 570, 810, 1060 and 2620 keV. Figure 4.3 shows pulse height spectra of prompt gamma-rays over 1.96-3.19 MeV energy exhibiting the hydrogen peak from propanol, methanol, water and benzene samples. The hydrogen peak has increasing intensity for benzene, methanol, propanol, and water samples respectively. Figure 4.4 shows enlarged pulse height spectra of prompt gamma-rays over 3.81-7.13 MeV energy exhibiting carbon and oxygen peaks due to inelastic scattering of 14 MeV neutrons from propanol, methanol, water and benzene samples. As mentioned earlier, the spectra exhibit the full energy peaks along with associated escape peaks. For the 4.439

MeV prompt gamma rays from carbon, the full energy and single escape (SE) peaks have been detected while for the 6.13 MeV prompt gamma rays of oxygen, the single escape, double escape (DE) and triple escape (TE) peaks have been detected along with the full energy peak. The 5106 keV gamma rays from nitrogen in melamine in the plastic container are interfering with DE peak of oxygen, thereby increasing the yield of DE peak of oxygen over SE peak of oxygen. The oxygen peaks have increasing intensity for benzene, methanol, propanol, and water samples, respectively. While the carbon peaks have increasing intensity for water, methanol, propanol and benzene samples, respectively.

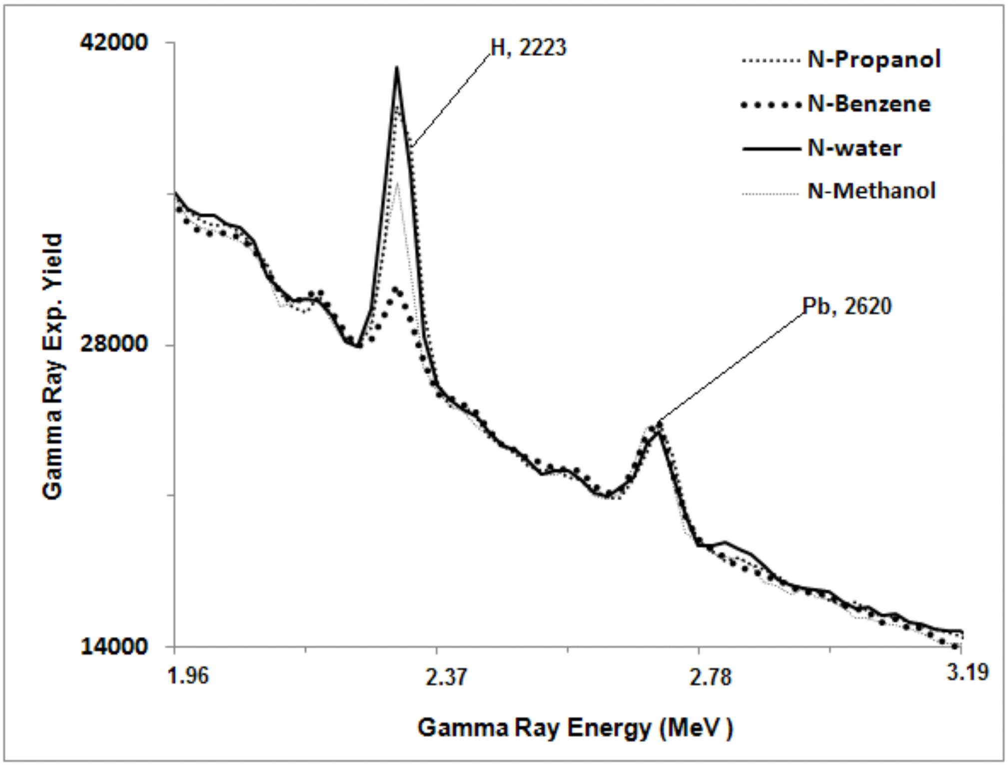

Figure 4.3 Enlarged $LaBr_3$:Ce detector prompt gamma ray spectra of benzene, propanol, water and methanol samples plotted over 1.96 MeV to 3.19 MeV energy range showing the hydrogen peak.

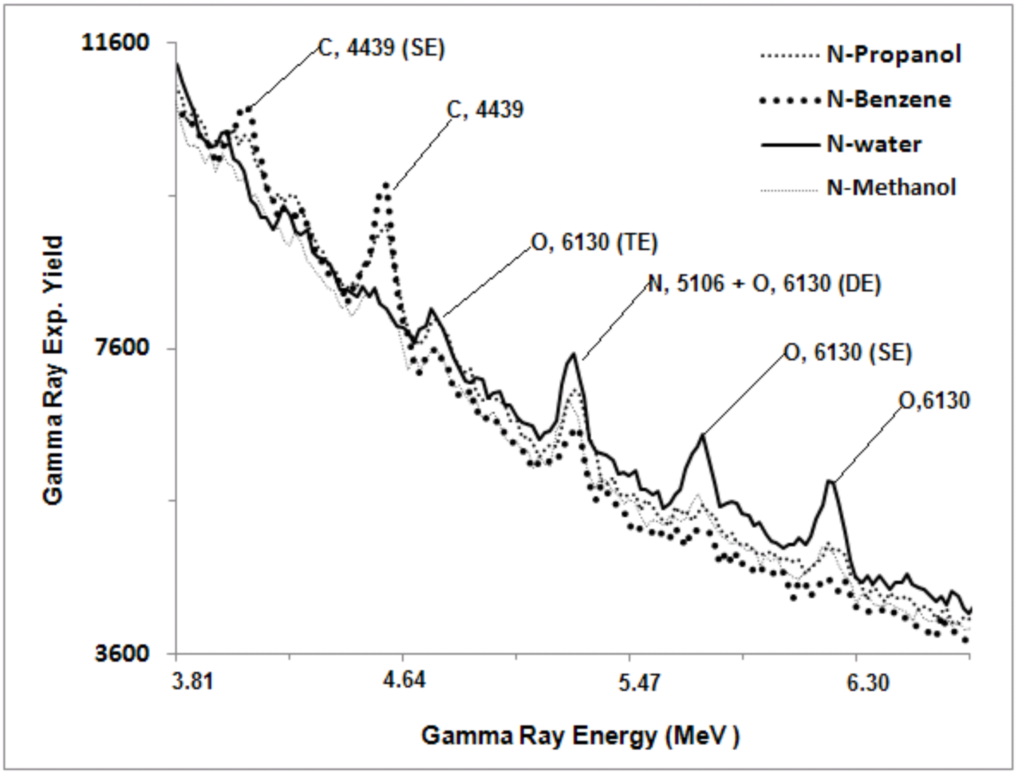

Figure 4.4 Enlarged LaBr$_3$:Ce detector prompt gamma ray spectra of benzene, propanol, water and methanol samples plotted over 3.81 MeV to 7.13 MeV energy range showing carbon and oxygen peaks along with associated escapes peaks.

BGO detector performance tests for the detection of high energy gamma rays from H, C and O in Toluene, Propanol, Methanol, Water, Benzene and Ethanol samples were carried out following the procedure used for the LaBr$_3$:Ce detector mentioned previously. Figure 4.5 shows the full pulse height spectrum of the BGO detector for prompt gamma-ray peaks due to inelastic scattering of 14 MeV neutrons from Propanol, Methanol, Water, Benzene and Ethanol samples and the detector lead shielding.

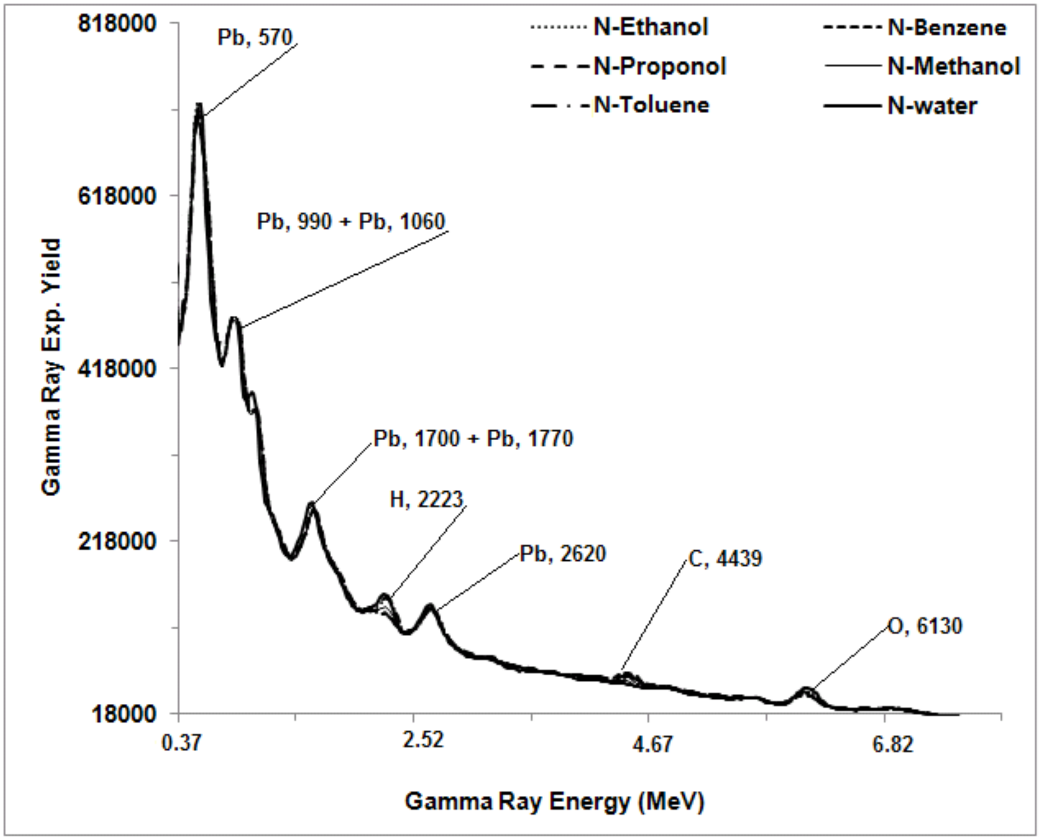

Figure 4.5 Full prompt gamma ray spectra of 102 mm x 102 mm (diameter x height) BGO detector for benzene, ethanol, toluene, water and methanol samples, taken with 14 MeV neutrons PGNAA setup

Figure 4.6 shows enlarged pulse height spectra of high energy prompt gamma-rays from ethanol, propanol, methanol, water and benzene samples taken with the BGO detector over 1.91-6.53 MeV energy range exhibiting hydrogen, carbon and oxygen peaks. Although the BGO detector is less sensitive to oxygen contents variation in the sample material, due to the large concentration of oxygen in the BGO detector, the oxygen peak still shows increased intensity of oxygen gamma rays for water sample. This is the main drawback of the BGO detector in the detection of oxygen in bulk samples using the PGNAA technique.

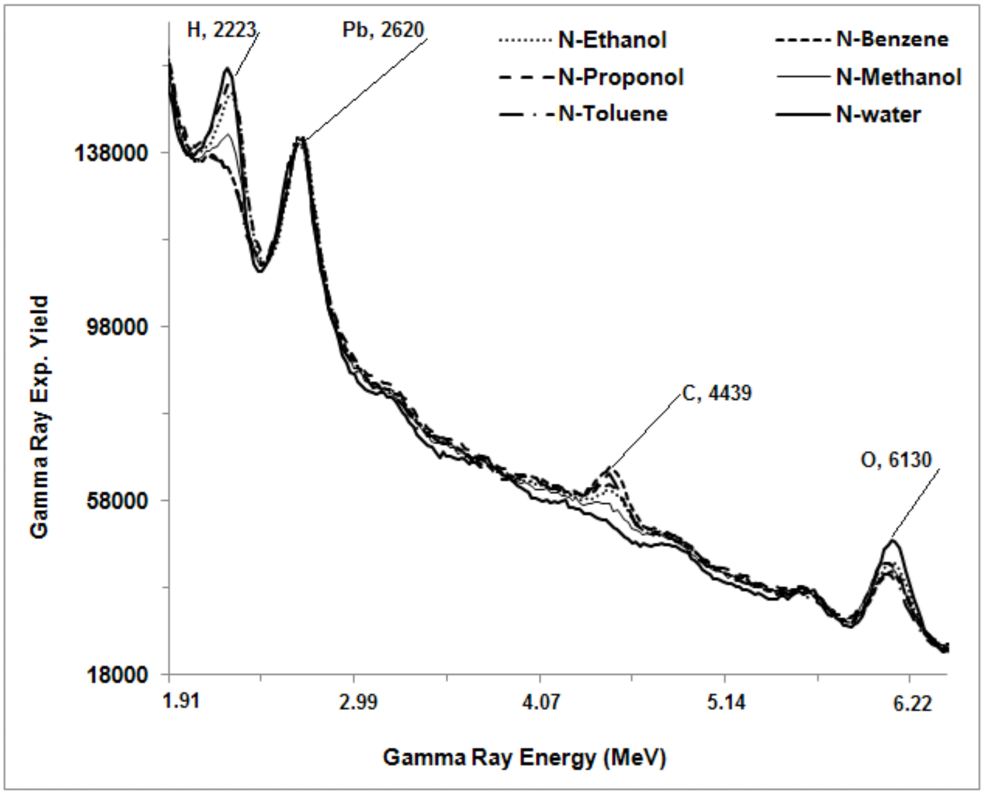

Figure 4.6 Enlarged BGO detector prompt gamma ray spectra of benzene, propanol, water and methanol samples plotted over 1.91 MeV to 6.53 MeV energy range showing carbon and oxygen peaks along with associated escapes peaks.

The net counts under the hydrogen, carbon and oxygen peaks were extracted by subtracting the container background spectra from the sample spectra. They were corrected for dead time and neutron flux variation. Finally the gamma ray yield curves were generated as functions of hydrogen, carbon and oxygen concentrations in benzene, water, propanol, ethanol and methanol samples. Figures 4.7 & 4.8 show gamma ray yields as functions of hydrogen, carbon and oxygen concentrations in benzene, water, propanol, ethanol and methanol samples taken with the $LaBr_3$:Ce detector. The solid lines in Figures 4.7 & 4.8 represent results of hydrogen, carbon and oxygen prompt gamma-ray yield from benzene, water, propanol, ethanol and methanol samples obtained through

Monte Carlo calculations using MNP4C code [35] following the procedure described elsewhere [27].

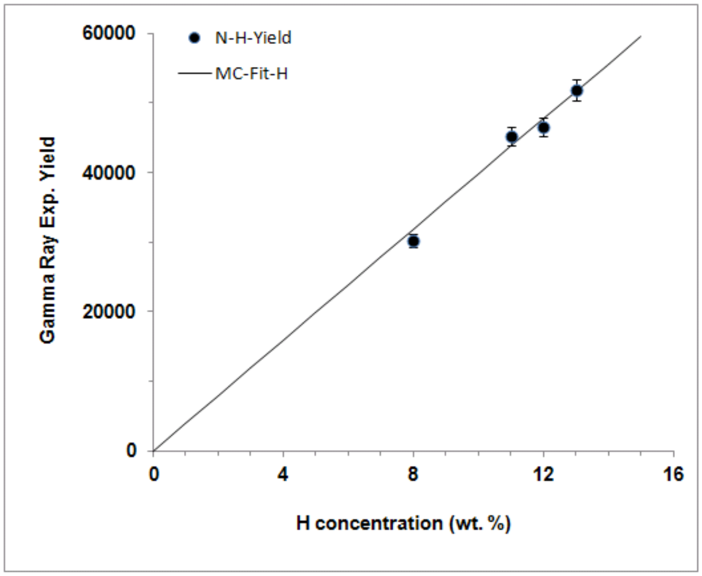

Figure 4.7 Integrated normalized experimental yield of hydrogen prompt gamma rays taken with the $LaBr_3$:Ce detector, plotted as a function of hydrogen concentration in benzene, propanol, water and methanol samples. The solid line is a Monte Carlo fit to the experimental data

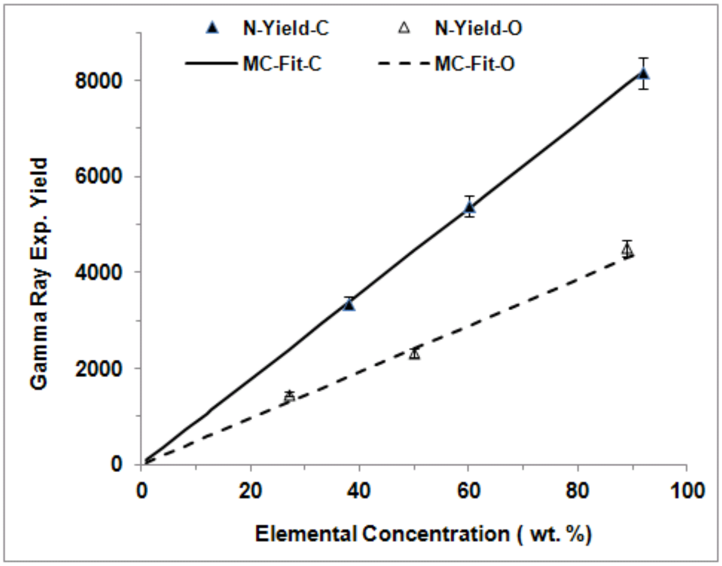

Figure 4.8 Integrated normalized experimental yield of carbon and oxygen prompt gamma rays taken with the $LaBr_3$:Ce detector, plotted as a function of carbon and oxygen concentrations in benzene, propanol, water and methanol samples. The solid line is a Monte Carlo fit to the experimental data.

Figures 4.9 & 4.10 show the gamma ray yields as functions of hydrogen and carbon concentrations in benzene, water, ethanol and methanol samples taken with the BGO detector. The solid lines in Figures 4.9 & 4.10 represent results of calculated yield of hydrogen and carbon prompt gamma-rays obtained from benzene, water, ethanol and methanol samples using Monte Carlo calculations.

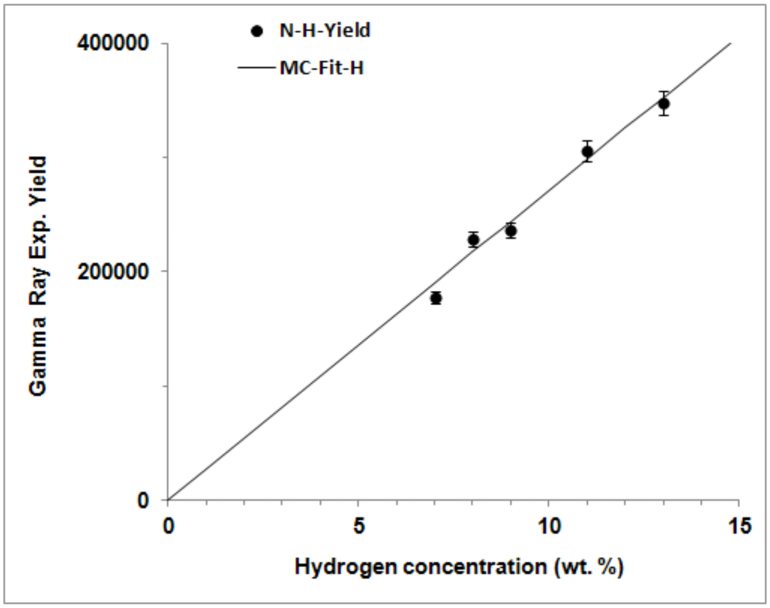

Figure 4.9 Integrated normalized experimental yield of hydrogen prompt gamma rays taken with the BGO detector, plotted as a function of hydrogen concentration in benzene, propanol, toluene, water and methanol samples. The solid line is a Monte Carlo fit to the experimental data

The excellent agreement between the theoretical and experimental yields of hydrogen, carbon and oxygen prompt gamma-rays as a function of their respective concentration recorded by the $LaBr_3$:Ce detector, shows its successful utilization in hydrogen, carbon and oxygen detection for contraband and explosive measurements. However for the BGO detector an excellent agreement has been achieved between the theoretical and experimental yield of hydrogen and carbon only. Due to its lack of sensitivity for oxygen detection, the BGO detector is not a suitable choice for oxygen measurements.

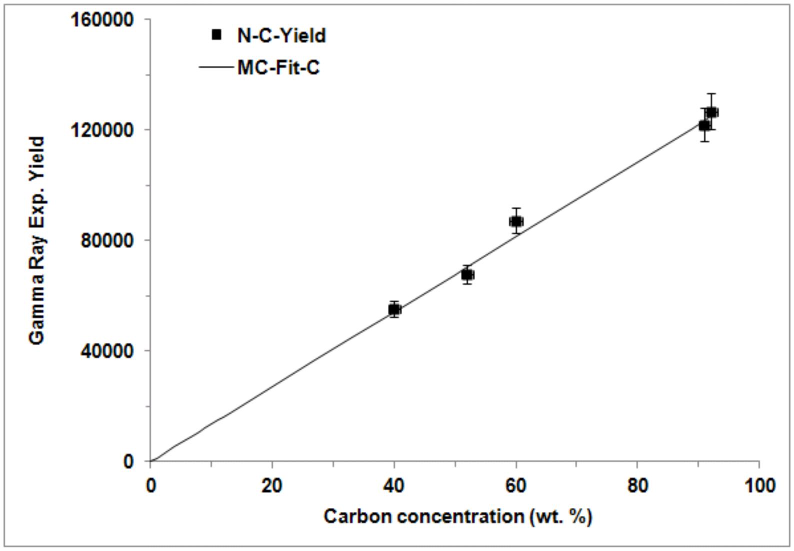

Figure 4.10 Integrated normalized experimental yield of carbon prompt gamma rays taken with the BGO detector, plotted as a function of carbon concentration in benzene, propanol, toluene, water and methanol samples. The solid line is a Monte Carlo fit to the experimental data

Minimum detectable concentrations of H, C and O in bulk samples using $LaBr_3$:Ce & BGO Detectors

Finally from the hydrogen, carbon and oxygen concentration measurements in the various samples, the minimum detectable concentrations, MDC, and their associated errors, σ_{MDC}, for hydrogen, carbon and oxygen were calculated for the KFUPM 14 MeV based PGNAA setup using equations (3.3 & 3.4) described earlier in section (3.3.1), and are listed in Table 4.2 for both the $LaBr_3$:Ce and BGO detectors.

The MDC of hydrogen and carbon in bulk samples using the BGO detector is lower than that of the $LaBr_3$:Ce detector because the BGO detector has a larger. Due to its large oxygen content, however, the BGO detector is not a suitable choice for detection of oxygen in bulk samples.

Detector Type	MDC_H (wt%)	MDC_C (wt%)	MDC_O (wt%)
$LaBr_3$:Ce	0.5±0.1	12.2±3.8	15.8±4.8
BGO	0.3±0.1	3.2±1.0	-

Table 4.2 MDC of Hydrogen, Carbon and Oxygen for 14 MeV neutron-based PGNAA setup using $LaBr_3$:Ce and BGO detectors

4.1.2 Calibration Measurements using $LaCl_3$:Ce Detector

Previously carbon, hydrogen and oxygen concentrations in bulk samples were measured in hydrocarbon samples in 14 MeV (NIS) studies using a $LaBr_3$:Ce detector. In this part of the study a 76 mm x 76 mm (3 in x 3 in) (height x diameter) $LaCl_3$:Ce detector has been used to measure hydrogen, carbon, and oxygen concentrations in the bulk hydrocarbon samples of benzene, butyl alcohol, propanol, propanic acid, and formic acid using the 14 MeV neutrons-based PGNAA setup described earlier in section 4.1.

The response of a $LaCl_3$:Ce detector has been found to depend upon the hydrogen content of bulk samples in prompt gamma analysis using 14 MeV neutron inelastic scattering (NIS). The moderation of 14 MeV neutrons from hydrogen in the bulk sample produces thermal neutrons around the sample which ultimately excite chlorine capture gamma rays in the $LaCl_3$:Ce detector material. Interference of 6.11 MeV chlorine gamma rays from the detector itself with 6.13 MeV oxygen gamma rays from the bulk samples makes the intensity of the 6.13 MeV oxygen gamma ray peak relatively insensitive to variations in oxygen concentration. The strong dependence of the 1.95 MeV doublet chlorine gamma ray yield on hydrogen content of the bulk samples confirms that fast neutron moderation from hydrogen in the bulk samples as a major source of production of thermal neutrons and chlorine gamma rays in the $LaCl_3$:Ce detector material.

Despite their poor oxygen detection capabilities, lanthanum halides detectors have nonetheless excellent detection capabilities for hydrogen and carbon in benzene, butyl alcohol, propanol, propanic acid, and formic acid bulk samples using 14 MeV neutron inelastic scattering (NIS). One can further conclude that $LaBr_3$:Ce detector is superior to $LaCl_3$:Ce detector in terms of MDC for all hydrocarbon samples due primarily to the large neutron capture cross section for Cl that introduces large and unwanted backgrounds in the Cl-based detector that are not present in the Br-based detector.

Although $LaCl_3$:Ce detectors [28, 36-38] have comparable light output and energy resolution with $LaBr_3$:Ce detectors [39-43], they, however, generate a higher background in thermal neutron fields due to thermal neutron capture in the chlorine of the $LaCl_3$:Ce detector material. Thermal neutrons are produced at the detector location due to moderation of 14 MeV neutrons from hydrogen in bulk samples. Therefore, chlorine background in $LaCl_3$:Ce detector in 14 MeV neutrons inelastic scattering studies is likely to increase with increasing hydrogen concentration in the bulk samples. Consequently, the interference of chlorine capture gamma rays background from $LaCl_3$:Ce detector and gamma rays of interest from the bulk sample may limit the utilization of $LaCl_3$:Ce detectors in PGNAA applications. The interference of 6.13 MeV prompt gamma rays of oxygen and 6.11 MeV chlorine capture gamma rays in $LaCl_3$:Ce detector material makes oxygen concentration analysis in 14 MeV neutron inelastic scattering via 6.13 MeV peak intensity more complicated. For bulk samples with higher hydrogen concentrations, the oxygen full energy peak intensity is relatively insensitive to oxygen concentration variations in the samples.

The elemental concentrations of the hydrocarbon bulk samples, as shown in Table 4.3, were independently verified using Atomic Absorption Spectrometry in the Department of Chemistry, King Fahd University of Petroleum and Minerals.

Compound	**Chemical Formula**	**C (wt-%)**	**H (wt-%)**	**O (wt-%)**
Butyl alcohol	$C_6H_{10}O$	73.5	10.2	16.3
Propanol	C_3H_8O	60.0	13.3	26.7
Benzene	C_6H_6	92.3	7.7	0.0
Propanic acid	$C_3H_6O_2$	48.6	8.1	43.2
Formic acid	CH_2O_2	26.1	4.3	69.6

Table 4.3 Elemental compositions of the hydrocarbon samples.

For prompt gamma ray analysis, the samples were prepared by filling the sample materials in the plastic containers. The containers were then irradiated in the PGNAA setup. The prompt gamma-ray data from the samples were acquired for a preset amount of time using a Multichannel Buffer-based data acquisition system. The neutron flux spectrum, which was recorded during each run using the NE213 detector, was later used for neutron flux normalization during data correction. The NE213 detector was operated at half Cs-137 pulse height bias following the procedure described in [43].

Figures 4.11(a) and 4.11(b) show prompt gamma-rays pulse height spectra due to inelastic scattering of the neutrons from water and benzene samples superimposed upon each other. Water and benzene samples were chosen to show the effect of hydrogen contents of the bulk samples on the gamma ray response of the $LaCl_3$:Ce detector. These samples represent extreme conditions, i.e., the water sample does not contain carbon while the benzene sample does not contain oxygen but both samples contain 7 wt.% and 11 wt.% hydrogen, respectively.

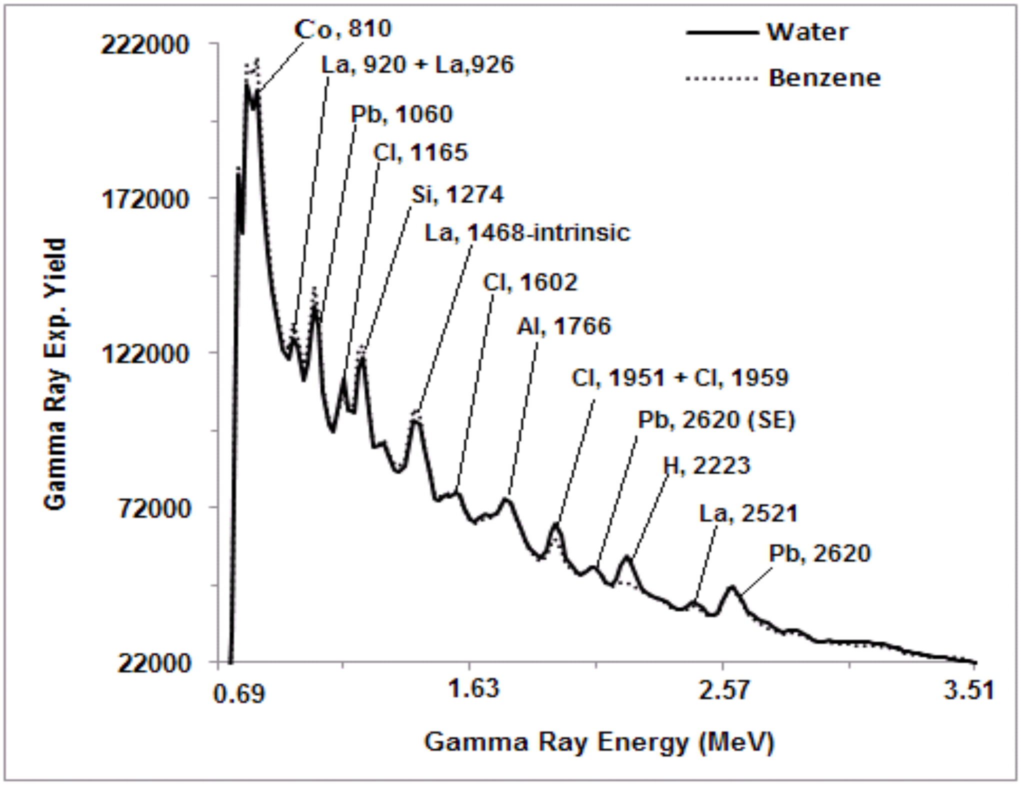

Figure 4.11(a) Prompt gamma ray spectra of $LaCl_3$:Ce gamma ray detector from benzene, and water samples showing capture and inelastic scattering prompt gamma rays over 0.68-3.51 MeV energy range.

Figure 4.11(a) shows the pulse height spectrum of gamma rays from benzene and water samples over 0.69-3.51 MeV energy showing lead gamma ray peaks at 1.06 MeV and

2.62 MeV, produced due to inelastic scattering of the neutrons from lead shielding. This is consistent with previously reported results in the literature [44]. The gamma ray peak at 0.81 MeV is due to decay of ^{58}Co produced in 14 MeV neutron induced ^{59}Co(n,2n)^{58}Co reaction. Cobalt is found in many metal alloys used for magnets or beam lines. Figure 4.11(a) also shows the single escape (SE) peak corresponding to the 2.62 MeV lead peak, 1.27 MeV silicon peak, the 1.77 MeV aluminum peak, along with the 0.92+0.93, 1.47 (intrinsic activity) and the 2.52 MeV peaks from lanthanum.

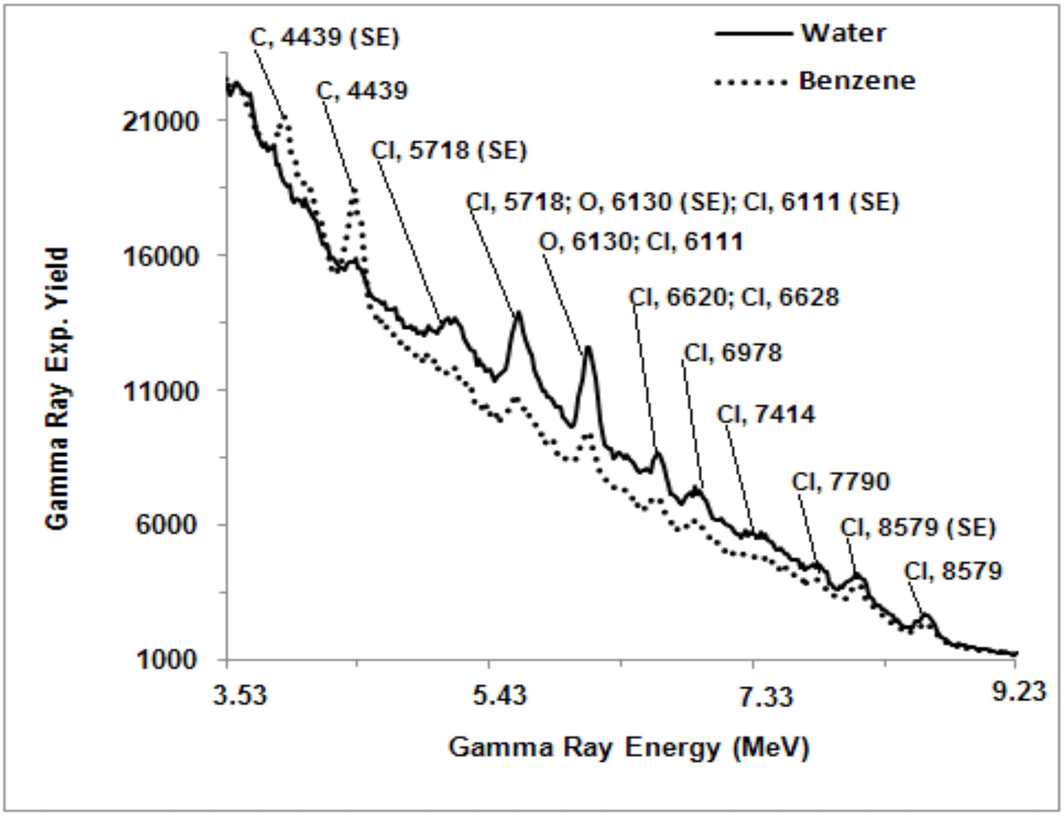

Figure 4.11(b) Prompt gamma ray spectra of $LaCl_3$:Ce gamma ray detector from benzene, and water samples showing capture and inelastic scattering prompt gamma rays over 3.53 MeV to 9.23 MeV energy range.

In Figure 4.11(a) prompt gamma ray peaks due to thermal neutron capture in chlorine of $LaCl_3$:Ce material appear at 1.17, 1.60 and 1.95-1.96 MeV (later referred as 1.95 MeV doublet). The intensities of 2.22 MeV hydrogen peak and 1.95 MeV chlorine peak are higher in the water spectrum than those in the benzene spectrum. The higher intensity of 1.95 MeV doublet chlorine gamma rays in the water sample as compared to the benzene sample is due to increasing thermalization of fast neutrons from higher hydrogen contents of the water sample. Therefore, the higher concentration of hydrogen in the water sample produces not only a higher intensity 2.22 MeV hydrogen capture gamma ray peak but also a higher intensity 1.95 MeV doublet chlorine capture peak intensity in the $LaCl_3$:Ce spectrum. This effect has been also observed in the higher energy part of the gamma ray spectra of water and benzene samples shown in Figure 4.11(b). In the higher energy gamma ray spectra, chlorine peaks at 5.72, 6.11, 6.62-6.63 (later referred as 6.62 MeV doublet), 6.98, 7.79 and 8.58 MeV are quite prominent. The intensity of these peaks is also higher for the water sample than that of the benzene sample. The full energy and associated single escape peaks of oxygen 6.13 MeV gamma rays overlap with these peaks. Energies of prompt gamma rays produced due to inelastic scattering of 14 MeV neutrons from chlorine and oxygen are listed in Table 4.4.

In the spectra of Figure 4.11(b) the full energy peak of oxygen at 6.13 MeV contains a contribution from 6.11 MeV chlorine prompt gamma rays, whose intensity strongly depends upon the hydrogen content of the bulk samples. The 6.11 MeV chlorine prompt gamma rays full energy peak has a 6.6 barns cross section [23]. The single escape peak of 6.13 MeV oxygen gamma rays contains contributions from both the overlapping 5.72 MeV full energy chlorine peak (with 1.8 barns cross section [23]) and the single escape peak of 6.11 MeV chlorine peak. No such effects were observed in the prompt gamma spectra of hydrogen, carbon, and oxygen elements taken with a $LaBr_3$:Ce detector in section 4.2.

	Gamma-ray energy (keV)	**Reaction**
O	2742	(n,n'γ)
	3089	(n,αγ)
	3684	(n,αγ)
	3854	(n,αγ)
	6130	(n,n'γ)
	6917	(n,n'γ)
	7117	(n,n'γ)
Cl	660	(n,n'γ)
	790	(n,n'γ)
	1210	(n,n'γ)
	1290	(n,n'γ)
	1780	(n,n'γ)
	2000	(n,n'γ)
	2150	(n,n'γ)
	2650	(n,n'γ)
	2710	(n,n'γ)
	3080	(n,n'γ)
	3170	(n,n'γ)
	3300	(n,n'γ)

Table 4.4 Energies of prominent (n,n'γ) gamma-rays of oxygen and chlorine [23]

Figures 4.12, 4.13 and 4.14 show the gamma ray pulse height spectra of the hydrocarbon samples, containing hydrogen, carbon and oxygen elemental concentrations over a broad range. Figure 4.12 shows the enlarged pulse height spectra of the hydrocarbon bulk samples over 1.63-2.96 MeV energy range. The 2.22 MeV hydrogen and the 1.95 MeV doublet chlorine capture peaks are shown in Figure 4.12 along with the 2.6 MeV lead peak from lead shielding. The intensity of the hydrogen peak increases with hydrogen concentration with a maximum for propanol sample (13 wt.%) and a minimum for the formic acid sample (4 wt.%). Due to increasing flux of thermal neutrons with hydrogen concentration, the chlorine 1.95 MeV doublet peak intensity also increases with hydrogen concentration. The maximum intensity of the chlorine 1.95 MeV doublet peak has been observed for propanol while the minimum intensity has been observed for the formic acid, as expected.

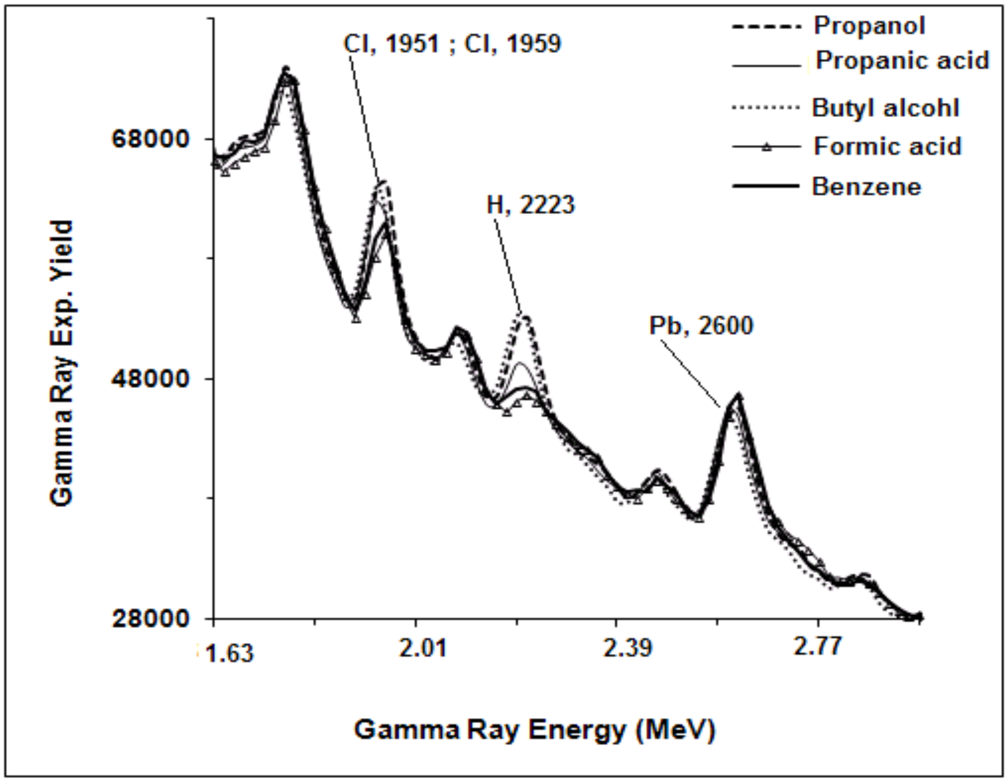

Figure 4.12 Enlarged $LaCl_3$:Ce detector prompt gamma ray spectra from the hydrocarbon samples plotted over 1.63 MeV to 2.96 MeV energy range showing chlorine, lead and hydrogen capture peaks.

In order to verify chlorine peak intensity dependence upon hydrogen concentration, the counts under the 1.95 MeV doublet chlorine peak in the hydrocarbon bulk samples were integrated and, after background subtraction and normalization, were plotted as a function of hydrogen concentration in the corresponding bulk samples.

Figure 4.13 shows the enlarged pulse height spectra of the hydrocarbon bulk samples over 3.53-4.86 MeV energy range. It shows an increasing intensity of the 4.44 MeV carbon peak along with its associated single escape peak. Benzene and formic acid have the highest and the lowest peak intensities for 4.44 MeV carbon peaks, with 92 wt.% and 26 wt.% carbon concentrations, respectively.

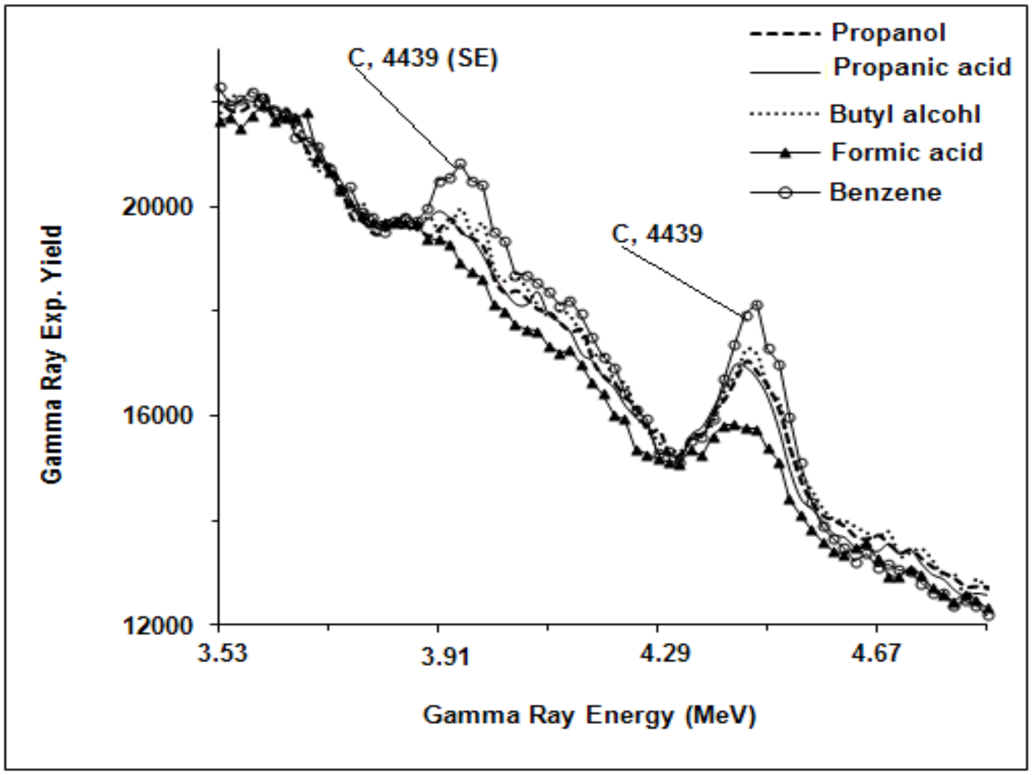

Figure 4.13 Enlarged $LaCl_3$:Ce detector prompt gamma ray spectra from the hydrocarbon samples plotted over 3.53 MeV to 4.86 MeV energy range showing the carbon peaks.

Figure 4.14 shows the enlarged spectra of the hydrocarbon bulk samples over 4.86-7.14 MeV energy range displaying the 5.72, 6.11, 6.62 MeV doublet, and 6.98 MeV chlorine peaks along with the 6.13 MeV oxygen peak. Also shown in Figure 4.14 are the associated single escape (SE) peaks.

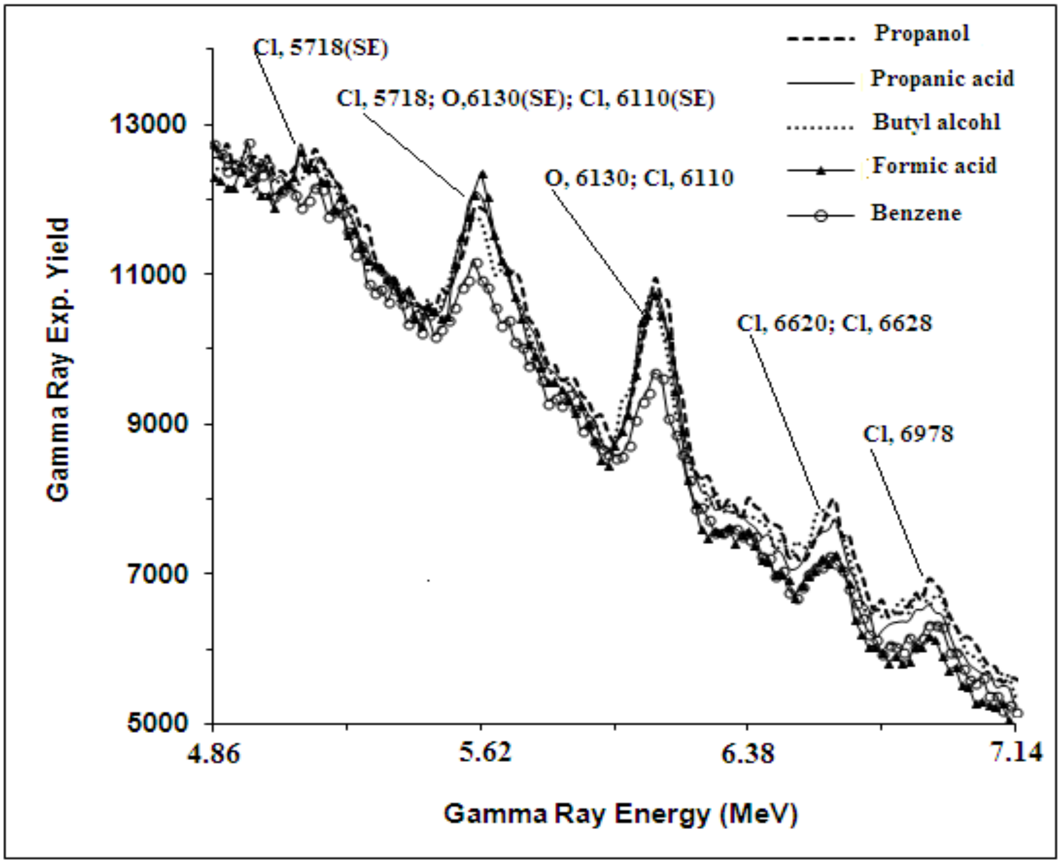

Figure 4.14 Enlarged $LaCl_3$:Ce detector prompt gamma ray spectra from the hydrocarbon samples plotted over 4.86 MeV to 7.14 MeV energy range showing oxygen and chlorine peaks.

Due to overlapping of 6.13 MeV oxygen and 6.11 MeV chlorine peaks and single escape peak of 6.62 MeV doublet chlorine peak, the resulting intensity of 6.13 MeV oxygen peak depends not only upon the oxygen, but also on the hydrogen contents of the bulk samples. Therefore, a sample with high oxygen concentration and low hydrogen concentration has almost the same intensity of oxygen 6.13 MeV peak as compared to a sample with low oxygen concentration and high hydrogen concentration. However, our setup is sensitive to samples that are extremely deficient in O as shown in Figure 4.14 for the case of benzene.

For hydrogen and carbon concentration analysis in the hydrocarbon bulk samples the hydrogen and carbon peak data in $LaCl_3$:Ce detector spectra were analyzed and the net counts under the hydrogen and carbon peaks were extracted by subtracting the container background spectra from the sample spectra. The net counts were then corrected for dead time and neutron flux variation using the procedure described in [43]. Finally, the gamma ray yield curves as a function of hydrogen and carbon concentration in the bulk samples were generated. Figures 4.15 and 4.16 show the gamma ray yields plotted as a function of hydrogen and carbon concentration, respectively, in the hydrocarbon samples.

The solid lines in Figures 4.15 and 4.16 represent results of hydrogen and carbon prompt gamma-ray calculated yields from the hydrocarbon samples obtained through Monte Carlo calculations using the MCNP4C code [35] following the procedure described in [43]. In Figure 4.15, the integrated normalized experimental yield of chlorine 1.95 MeV doublet prompt gamma rays has also been superimposed on the integrated normalized yield of 2.22 MeV hydrogen peak yield to show how chlorine yield depends upon hydrogen content in the samples. The solid line is a Monte Carlo fit to the experimental data. Within experimental uncertainties, chlorine and hydrogen peak data overlap each other. The excellent agreement between the theoretical and the experimental yields of hydrogen and carbon prompt gamma-rays as a function of their respective concentrations in the bulk samples shows the successful application of $LaCl_3$:Ce detector in hydrogen and carbon concentrations measurements in the hydrocarbon bulk samples.

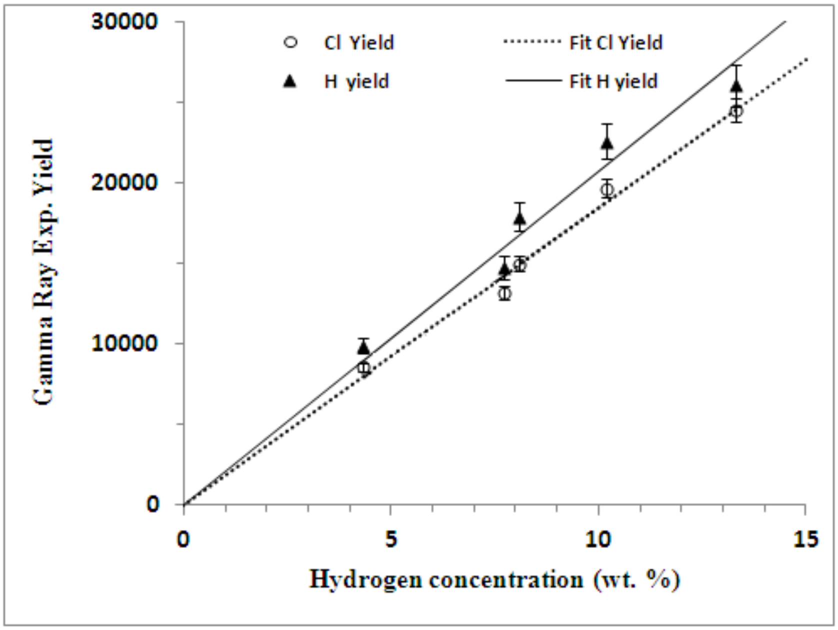

Figure 4.15 Integrated normalized experimental yield of 2.22 MeV peak of hydrogen prompt gamma rays taken with the $LaCl_3$:Ce detector and integrated experimental yield of chlorine 1.95 MeV doublet prompt gamma rays, plotted as a function of hydrogen concentration in the hydrocarbon samples. The solid line is a Monte Carlo fit to the experimental data.

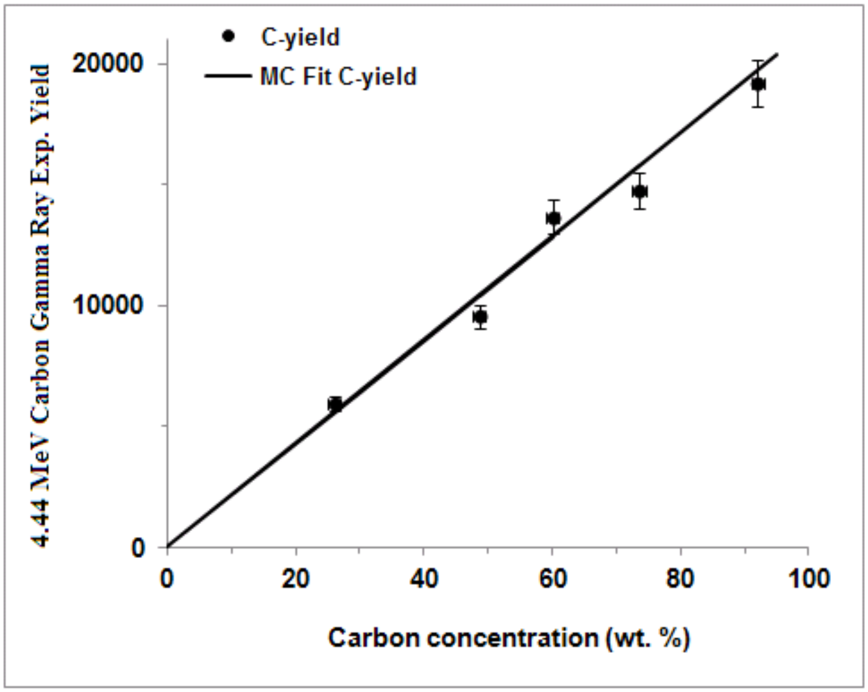

Figure 4.16 Integrated normalized experimental yield of carbon 4.44 MeV prompt gamma rays taken with the $LaCl_3$:Ce detector, plotted as a function of carbon concentration in the hydrocarbon samples. The solid line is a Monte Carlo fit to the experimental data

Lastly, full energy (FE) and SE peaks of oxygen from the hydrocarbon samples were analyzed. In this analysis, FE and SE peaks from the hydrocarbon samples were integrated and then benzene sample integrated counts were subtracted from the remaining samples as background (due to zero oxygen concentration). Figure 4.17 shows benzene sample counts subtracted gamma ray yields plotted as a function of oxygen concentration in the hydrocarbons samples. As expected FE peak yield is practically insensitive to oxygen concentration but SE peak yield shows a weak linear dependence of gamma ray yield on oxygen concentration due to small difference between various SE peaks heights of the hydrocarbon samples.

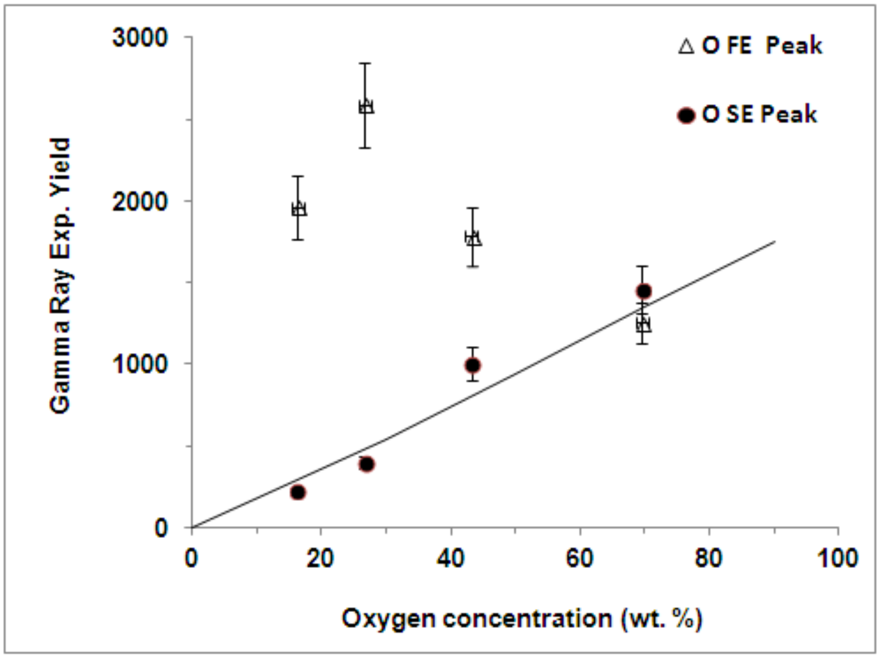

Figure 4.17 Integrated normalized experimental yield of oxygen 6.13 MeV full energy (FE) and single escape (SE) prompt gamma rays taken with the $LaCl_3$:Ce detector, plotted as a function of oxygen concentration in the hydrocarbon samples. The solid line is a Monte Carlo fit to the experimental data

Minimum detectable concentrations of H, C and O in bulk samples using $LaCl_3$:Ce Detector

Finally**,** the minimum detectable concentration, MDC, and its associated error, σ_{MDC}, were calculated for hydrogen and carbon in the hydrocarbon samples using equations (3.3 & 3.4) described earlier in section (3.3.2). For 90 mm x 145 mm (diameter x height) cylindrical hydrocarbon bulk samples, the MDC of the KFUPM 14 MeV neutron-based PGNAA setup was calculated for hydrogen and carbon concentration measurement data taken with the $LaCl_3$:Ce detector using 2.22 MeV and 4.44 MeV gamma rays respectively. The MDC data for the $LaCl_3$:Ce detector are listed in Table 4.5. For comparison, MDC of hydrogen calculated using 1.95 MeV chlorine peak is also included in Table 4.5. As expected from Figure 4.17, the MDC of hydrogen calculated using hydrogen peak agrees within statistical uncertainties with that calculated using the chlorine peak.

For the sake of comparison, the MDC for hydrogen, carbon and oxygen in bulk samples measured using a $LaBr_3$:Ce detector (section 4.2.1) have also been included in Table 4.5. Apparently values of MDC for carbon seems to be comparable for both the $LaCl_3$:Ce and the $LaBr_3$:Ce detectors, while for hydrogen MDC for the $LaCl_3$:Ce detector is 2 times poorer than those for the $LaBr_3$:Ce detector .

Detector	**MDC_H (wt%)**	**MDC_C (wt%)**	**MDC_O (wt%)**
$LaBr_3$:Ce	0.5±0.1	12.2±3.8	15.8±4.8
$LaCl_3$:Ce	1.11±0.32 *1.67±0.51	9.68±2.94	-

*** MDC of hydrogen using 1.95 MeV doublet chlorine gamma rays**

Table 4.5 MDC of Hydrogen, Carbon and Oxygen for 14 MeV neutron-based PGNAA setup using $LaCl_3$:Ce and $LaBr_3$:Ce

4.2 Analysis of Contraband-Proxy Bulk Samples Using $LaBr_3$:Ce Detector

In this part of the study, Hydrogen, Carbon and Oxygen concentrations were measured in caffeine, urea, ammonium acetate and melamine bulk samples via 14 MeV neutron inelastic scattering (NIS) using a $LaBr_3$:Ce detector. The samples tested here represent drugs, explosives and benign materials, respectively. Despite its intrinsic activity, the $LaBr_3$:Ce detector performed well in detecting the hydrogen, carbon and oxygen in bulk samples. Because 5.1 MeV nitrogen gamma rays interfere with silicon and calcium prompt gamma rays from the room background, the nitrogen peak was not detected in the samples. An excellent agreement was observed between the experimental and theoretical yields of 2.22, 4.43 and 6.13 MeV gamma rays from the analyzed samples as a function of H, C and O concentrations, respectively. Within statistical errors, the minimum detectable concentration (MDC) of hydrogen, carbon and oxygen in the tested materials were consistent with previously reported MDC values for these elements measured in hydrocarbon samples in section 4.1.1.

The samples tested were used because their elemental composition ratios are similar to benign, explosive and narcotics materials, as shown in Table 4.6.

Material Category	Compound	Formula	Elemental Concentration (wt. %)				$(C/O)_{calc}$	$(C/O)_{exp}$	N/O
			H	C	N	O			
Benign	Melamine	$C_3H_6N_6$	4.8	28.6	66.7	-	-	-	-
Explosive	Ammonium Acetate	$C_2H_7NO_2$	9.1	31.2	18.2	41.6	0.75	0.92 ±0.12	0.75
	Urea	CH_4NO_2	6.7	20.0	46.7	26.7	0.75	0.91±0.11	1.75
Narcotics	Caffeine	$C_8H_{10}N_4O_2$	5.2	49.5	28.6	16.5	3.00	3.82 ± 0.38	1.73

Table 4.6 Elemental composition of proxy material samples analyzed in this study

Carbon, oxygen and hydrogen concentrations for melamine, ammonium acetate, urea, and caffeine bulk samples were measured using the 14 MeV neutron-based PGNAA setup, the setup is shown in Figure. 4.1 and it was described earlier in section 4.1.

Figure 4.18 shows the prompt gamma-ray pulse height spectra from inelastic 14 MeV neutron scattering for hydrogen, carbon and oxygen in the caffeine and ammonium acetate bulk samples with shielding comprising 0.46-8.30 MeV gamma-rays using the $LaBr_3$:Ce detector. The gamma ray energy values from inelastic 14 MeV neutron scattering in lead were observed at 570, 810, 1060 and 2620 keV.

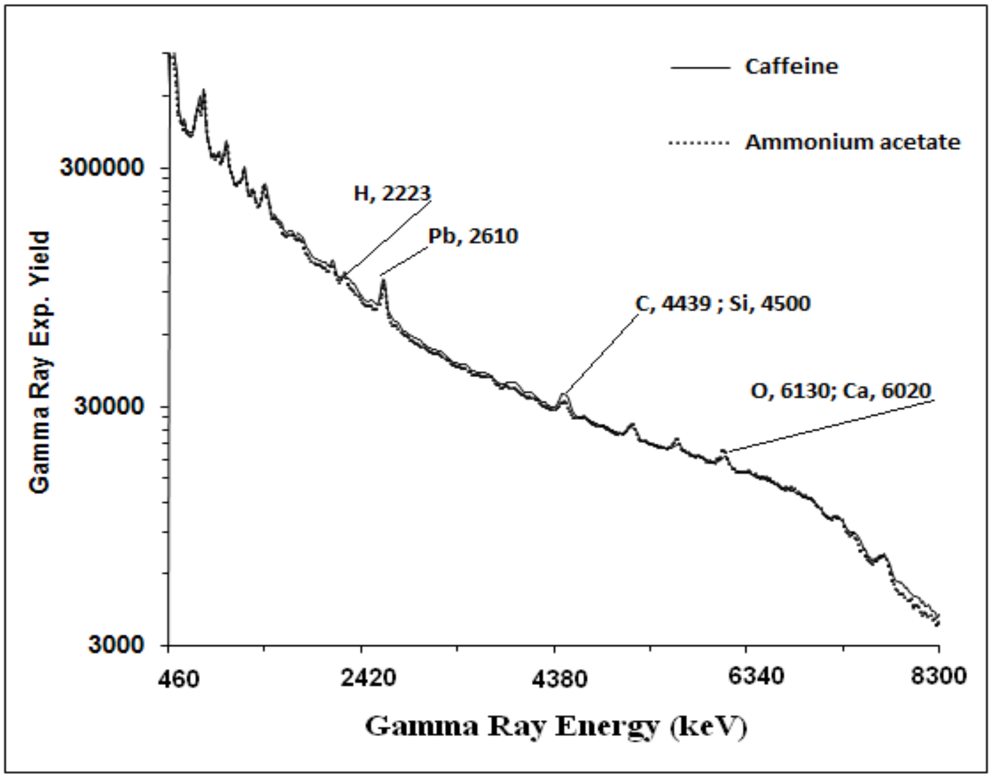

Figure 4.18 Prompt gamma ray spectra of $LaBr_3$:Ce gamma ray detector from ammonium acetate and caffeine bulk samples plotted over 0.46 to 8.3 MeV energy range , superimposed upon each other.

Figures 4.19-4.21 show the prompt gamma spectra for the caffeine, ammonium-acetate, urea, and melamine bulk samples with hydrogen, carbon and oxygen prompt gamma ray peaks in the 1.92-6.53 MeV range as well as the background gamma rays produced through inelastic 14 MeV neutron scattering from silicon and calcium in the walls and floor [45]. Such gamma rays can interfere with carbon and oxygen prompt gamma rays; the 4.50 MeV silicon peak interferes with the 4.44 MeV carbon peak, and the 6.02 MeV calcium gamma ray interferes with the 6.13 MeV oxygen peak [46]. Figure 4.19 shows the full hydrogen energy peak at 2.22 MeV and the Pb peak from the shielding material at 2.62 MeV. Also shown in Figure 4.19 is the single escape (SE) peak that corresponds to the full 2.62 MeV energy peak for Pb. The hydrogen peak increases in intensity in the samples as the hydrogen concentration increases. The maximum peak intensity was observed in the ammonium acetate sample with a 9.1 wt.% hydrogen concentration, while the minimum peak intensity was observed for melamine, which has a 4.8 wt.% hydrogen concentration.

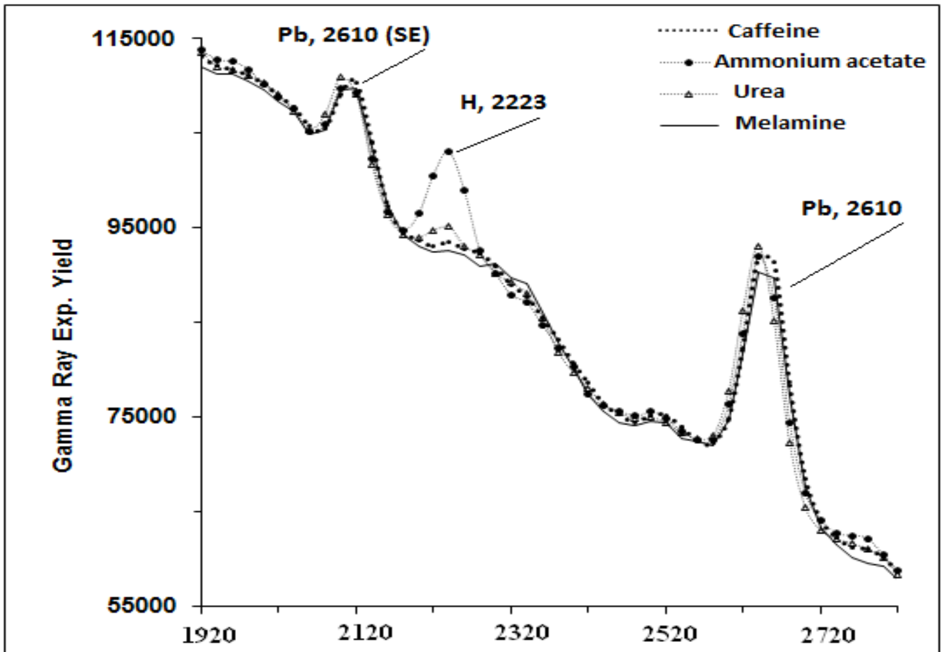

Figure 4.19 LaBr3:Ce detector prompt gamma ray spectra from ammonium acetate, caffeine, urea and melamine bulk samples plotted over 1.92 MeV to 2.82 MeV energy range showing hydrogen and lead shielding peaks.

Figure 4.20 shows the pulse height spectra for the caffeine, ammonium-acetate, urea and melamine bulk samples over a 3.79- 4.76 MeV energy range with single escape (SE) and full energy peaks at 4.439 MeV prompt gamma rays via inelastic 14 MeV neutron scattering from carbon. The carbon peak intensity in Figure 4.20 increases with carbon concentration in the samples (i.e., the maximum peak intensity for the carbon peak was observed in caffeine with 49.5 wt. % carbon, and the minimum peak intensity was observed for the urea bulk sample containing 20.0 wt. % carbon).

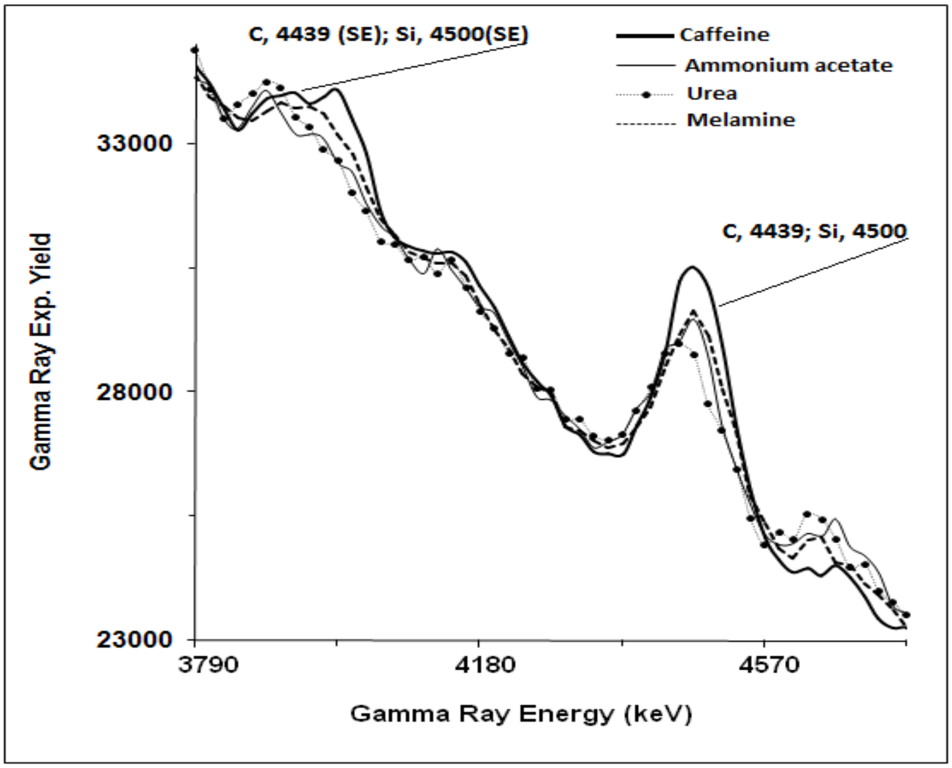

Figure 4.20 LaBr3:Ce detector prompt gamma ray spectra from ammonium acetate, caffeine, urea and melamine bulk samples plotted over 3.79 MeV to 4.76 MeV energy range showing carbon full energy peak along with carbon and silicon single escape peaks.

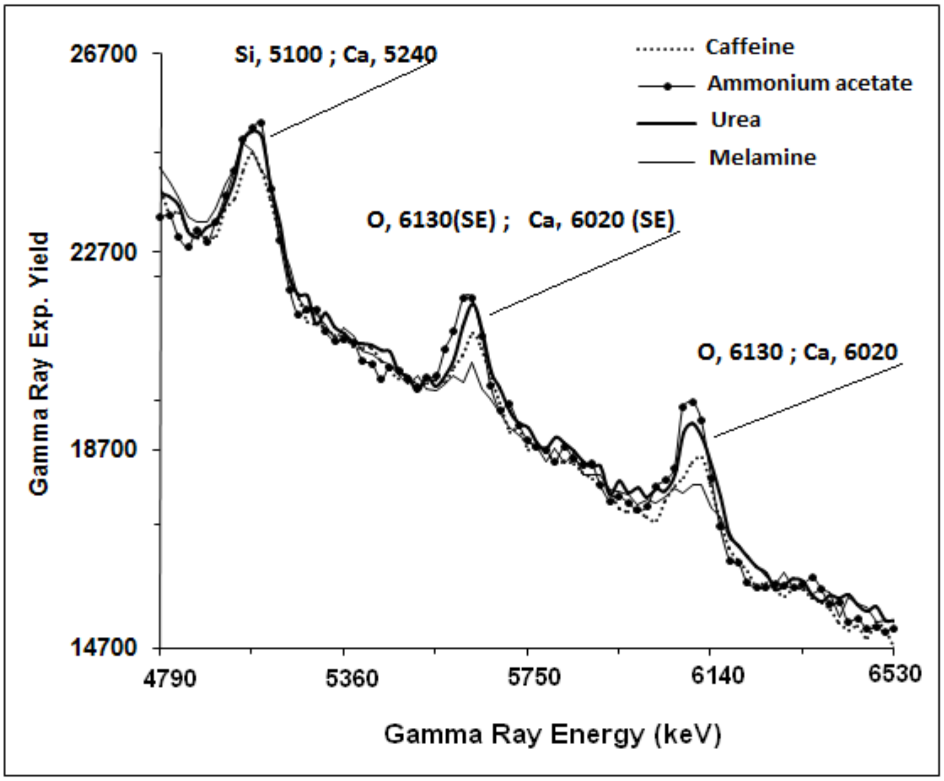

Figure 4.21 LaBr$_3$:Ce detector prompt gamma ray spectra of from ammonium acetate, caffeine, urea and melamine bulk samples plotted over 4.97 MeV to 6.53 MeV energy range showing oxygen peaks along with calcium and silicon peaks from the room background.

Figure 4.21 shows the pulse height spectrum for the caffeine, ammonium-acetate, urea and melamine bulk samples over the 4.97-6.53 MeV energy range including the full energy peak at the 6.13 MeV prompt gamma ray via inelastic 14 MeV neutron scattering from oxygen. Also shown in Figure 4.21 is the full energy peak for 5.10 MeV gamma rays due to 14 MeV neutron inelastic scattering from silicon in the walls and floor of the room, it is higher than the oxygen double escape peak because the silicon content is higher in the walls and floor. The full energy and single escape peaks from 6.13 MeV for oxygen in the caffeine, ammonium-acetate, urea and melamine bulk samples demonstrated an increasing trend proportional to the oxygen content in the samples. The maximum intensity for an oxygen peak was observed in ammonium acetate, with a 41.6 wt.% oxygen concentration, while the minimum intensity was observed for melamine, with a 0.0 wt. % oxygen concentration. Because the silicon and calcium prompt gamma rays from the room background interfere with the 5.1 MeV nitrogen gamma rays, the nitrogen peak could not be detected in the samples.

Data from the $LaBr_3$:Ce detector for hydrogen, carbon and oxygen peaks in the respective pulse height spectra for the caffeine, ammonium acetate, urea, and melamine bulk samples were analyzed. The net content for the H, C and O peaks were extracted by subtracting the floor and walls background spectra from the sample spectra. The net counts were then corrected for dead time and neutron flux variations. Finally, the gamma rays yield curves were generated as a function of H, C and O concentrations in the bulk samples.

Figures 4.22 and 4.23 show the gamma ray yields as a function of the O, C and H concentrations measured using the $LaBr_3$:Ce detector. The straight lines in Figures 4.22 and 4.23 are the theoretical O, C and H prompt gamma ray yields calculated by Monte Carlo simulations using the MCNP4C code [35] following a the procedure described in [43]. The theoretical and experimental yields were consistent for the H, C and O as measured by the $LaBr_3$:Ce detector, which demonstrated that the detector is appropriate for measuring H, C and O in contraband and explosive detection.

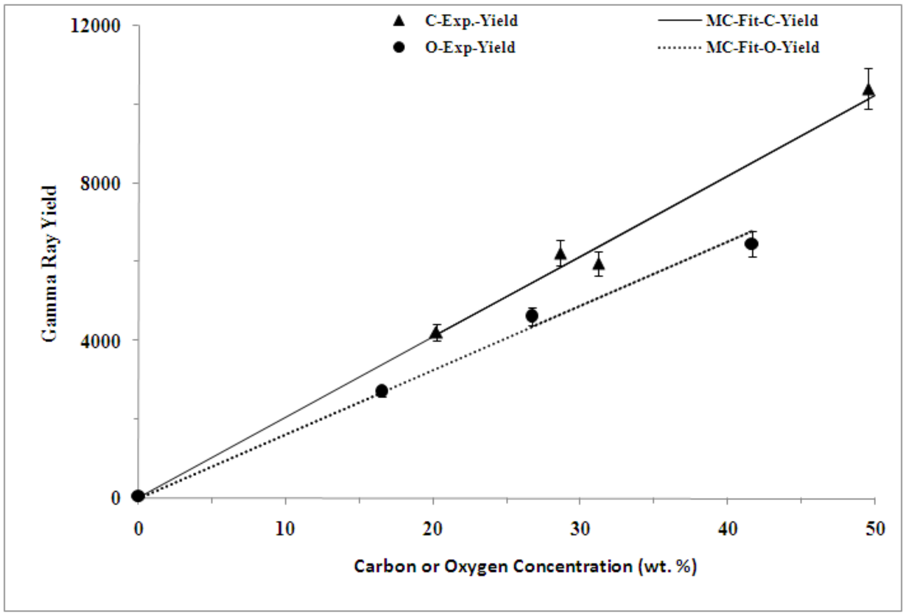

Figure 4.22 Integrated normalized experimental yield of carbon and oxygen prompt gamma rays taken with the $LaBr_3$:Ce detector, plotted as a function of oxygen concentration in ammonium acetate, caffeine and urea bulk samples. The straight lines are Monte Carlo fits to the experimental data.

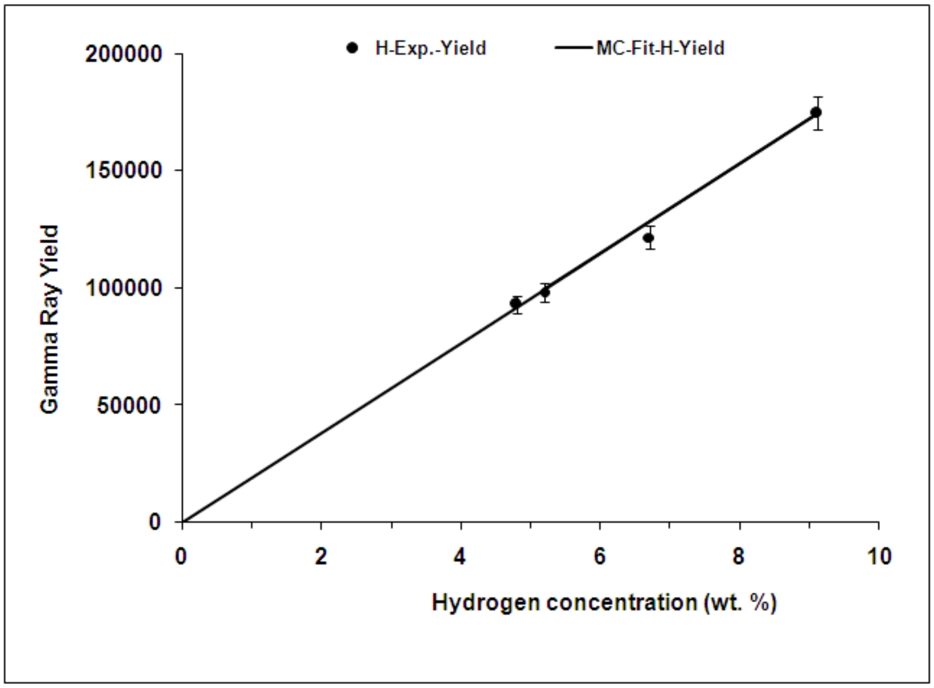

Figure 4.23 Integrated normalized experimental yield of hydrogen prompt gamma rays taken with the $LaBr_3$:Ce detector, plotted as a function of hydrogen concentration in ammonium acetate, caffeine, urea and melamine bulk samples. The solid line is a Monte Carlo fit to the experimental data

The carbon to oxygen (C/O) element ratio for the samples, which differentiates between explosive and narcotics, was calculated from the experimental data for ammonium-acetate, urea and caffeine. The C/O ratios for the ammonium-acetate and urea were 0.92 ± 0.12 and 0.91 ± 0.11, respectively, while for caffeine, the C/O was 3.82 ± 0.38. As expected, the explosive-like materials (ammonium-acetate and urea) produced smaller C/O ratios, while the narcotics-like material (caffeine) generated a higher C/O ratio. Within experimental error, the C/O ratios for ammonium-acetate and urea was consistent with the calculated value, while the C/O ratio for caffeine was approximately 15 % higher than the calculated value.

Minimum detectable concentrations of H, C and O in the proxy material samples

The minimum detectable concentration, MDC, and its associated error, σ_{MDC}, were calculated for hydrogen and carbon in the caffeine, ammonium-acetate, urea and melamine bulk samples using the LaBr3:Ce detector in the KFUPM 14 MeV-based PGNAA setup. The MDC and its associated error, σ_{MDC}, were calculated for an elemental concentration *C* measured for a peak with the net content *P* and associated background content *B* (under the peak) using equations (3.3) & (3.4) described earlier in section (3.3.2). For 90 mm x 145 mm (diameter x height) cylindrical bulk samples containing caffeine, ammonium-acetate, urea and melamine, the MDC for hydrogen, carbon and oxygen using the KFUPM 14 MeV neutron-based PGNAA setup with the $LaBr_3$:Ce detector are listed in Table 4.7. For comparison, the MDC for hydrogen, carbon and oxygen in the bulk hydrocarbon samples measured using a $LaBr_3$:Ce detector (section 4.1.1) are also included. Within statistical errors, the MDC values for H, C and O in the samples are consistent with the MDC from the hydrocarbon bulk samples previously reported in Table 4.2.

Samples Type	**MDC_H (wt %)**	**MDC_C (wt %)**	**MDC_O (wt %)**
Hydrocarbons	**0.5±0.1**	**12.2±3.8**	**15.8±4.8**
Proxy Materials	**0.2±0.1**	**11.9±3.6**	**16.8±5.1**

Table 4.7 Comparison of MDC of Hydrogen, Carbon and Oxygen for the Proxy material samples and hydrocarbon samples (table 4.2) for KFUPM 14 MeV neutron-based PGNAA setup using $LaBr_3$:Ce

CHAPTER 5

NITROGEN ANALYSIS OF BULK SAMPLES USING THERMAL NEUTRON CAPTURE

In this part of the study, Nitrogen concentration was measured in explosive and narcotics proxy material bulk samples (anthranilic acid, caffeine, melamine, and urea) through the Thermal Neutron Capture (TNC) reaction using the 350 keV accelerator based prompt gamma ray neutron activation (PGNAA) setup, as well as the MP320 portable neutron generator-based PGNAA setup. Detection of nitrogen in bulk samples using (NIS) PGNAA is a tedious and difficult task due to interference of nitrogen prompt gamma rays with oxygen gamma rays. Although nitrogen has a small thermal neutron capture cross section, yet it can be detected via prompt (TNC) PGNAA [42,47].

5.1 Monte Carlo Design Calculations of TNC based PGNAA Setup

In this work a TNC-based PGNAA setup has been developed using the 350 keV accelerator to measure nitrogen concentration in bulk samples. Design of the PGNAA setup moderator was obtained through Monte Carlo simulations. The setup was then tested through measurements of prompt gamma ray intensities produced due to thermal neutron capture in explosive and narcotics proxy materials, namely urea, caffeine and disperse orange. These materials were chosen because they have elemental ratios similar to benign, explosive and narcotics substances, respectively Table 5.1 shows elemental compositions and elemental ratios of the bulk sample materials used in this study.

Sample	**Formula**	**Sample Mass (g)**	**H (wt.%)**	**C (wt. %)**	**N (wt.%)**	**O (wt.%)**	**N/O**
Melamine	$C_3H_6N_6$	**682**	**4.8**	**28.6**	**66.7**	**0**	**0**
Urea	CH_4N_2O	**816**	**6.7**	**20.0**	**46.7**	**26.7**	**1.75**
Caffeine	$C_8H_{10}N_4O_2$	**580**	**5.2**	**49.5**	**28.6**	**16.5**	**1.73**
Anthranilic acid	$C_7H_7NO_2$	**534**	**3.7**	**44.9**	**7.5**	**17.1**	**0.44**
Disperse orange	$C_{18}H_{14}N_4O_2$	**534**	**4.4**	**67.9**	**17.6**	**10.1**	**1.74**

Table 5.1 Elemental compositions of proxy material samples used in this study

Monte Carlo calculations were carried out using code MCNP4B2 [22] to design a 350 keV accelerator based PGNAA setup. The PGNAA setup is based upon the detection of prompt gamma-rays produced due to the capture of thermal neutrons in the bulk samples. Fast neutrons produced in a D(d,n) reaction are moderated down to thermal neutron energies at the specimen site using an external moderator [43, 48]. The moderator size was optimized through Monte Carlo calculations assuming an isotropic point neutron source. The sample length defines the length of the moderator. For convenience, a sample with 90 mm diameter and 145 mm height was used. Thermal neutron yield in the sample volume was calculated using F4 Tally of MCNP4B2 code, which allows calculating the particle flux averaged over a cell. For the simulation study, the moderators and the sample cells were divided into sub-cells of 1 cm thickness. These calculations were carried out using a workstation utilizing dual AMD Athlon MP 2800+ processors and following the procedure in [43, 48].

In order to optimize the source-moderator-sample geometry of the setup, the thermal neutron flux at the sample location was calculated for three different arrangements of source-moderator-sample geometry as shown in Figure 5.1(a-c). Figure 5.1(a) shows the geometry for thermal neutron production at a cylindrical sample (90 mm in diameter and 145 mm in height) by inserting a cylindrical high-density polyethylene moderator (HPM) slab between the neutron producing target and the sample. The cylindrical HPM slab (disk shaped) has a fixed 25 cm diameter. Its thickness was varied in one-cm steps along with the sample source distance. The thermal neutron intensity was calculated in the sample volume for each HPM slab thickness.

In the next step, as shown in the configuration of Figure 5.1(b), the sample was enclosed in a HPM cylinder and was placed after a HPM slab with 6 cm thickness obtained from calculations of part (a) corresponding to Figure 5.1(a). The HPM slab was included again in the geometry to find neutron beam-focusing effects of the slab on the HPM cylinder, if any. In part (b) as shown in Figure 5.1(b), the HPM cylinder thickness around the sample (i.e outer diameter of the HPM cylinder) was varied in equal steps and the thermal neutron intensity was calculated in the sample volume for each external diameter of the moderator cylinder. Finally, the sample was enclosed in the HPM cylinder and was placed next to the neutron target without the HPM slab, as shown in Figure 5.1(c). The thermal neutron intensity was calculated in the sample volume as a function of the HPM cylinder thickness around the sample (outer diameter of the moderator).

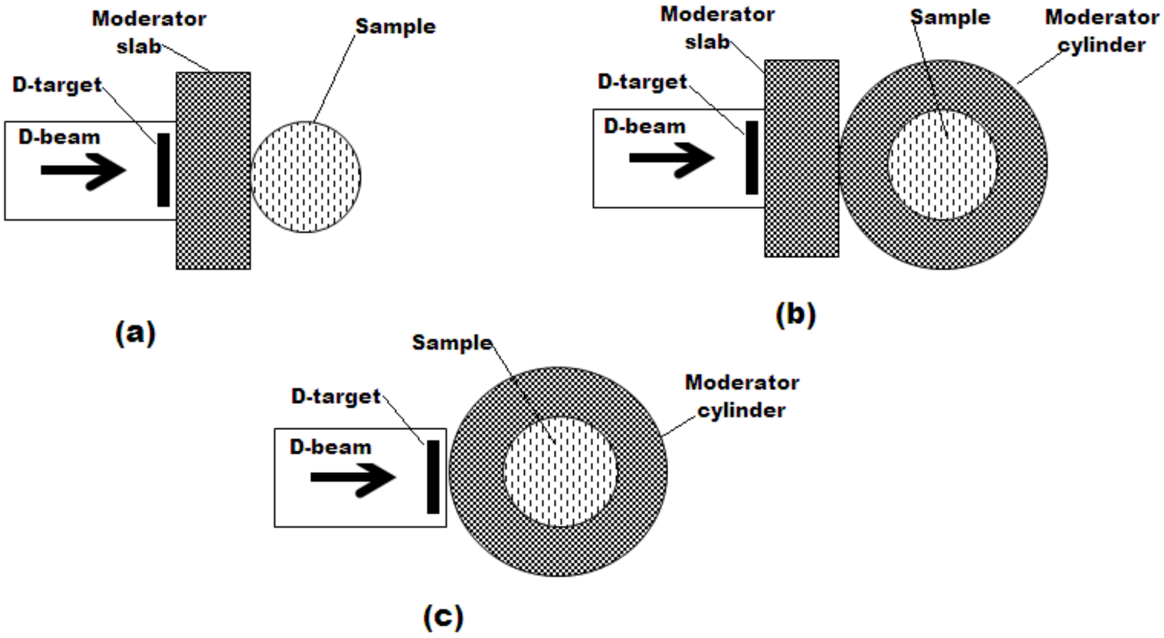

Figure 5.1 Side view of schematic of three different source-moderator-sample geometries of PGNAA setup tested in the present study (a) source + slab moderator (b) source + slab + cylindrical moderators and (c) source + cylindrical moderator

Figure 5.2 shows the calculated thermal neutron intensity as a function of moderator thickness for the three different cases superimposed upon each other for comparison. The thermal neutron intensity for slab-only case (Figure 5.1(a)) increases with slab thickness and reaches an optimum value for a 6 cm thick slab and then drops off due to the increasing distance from the neutron source. By further enclosing the sample in a HPM cylinder (Figure 5.1 (b)), the thermal neutron intensity increases with increasing thickness of the cylinder around the sample and then decreases. The maximum intensity of thermal neutrons in the HPM slab + cylinder case was obtained for a combination of 6 cm thick HPM slab and 4 cm thick HPM cylinder around the sample.

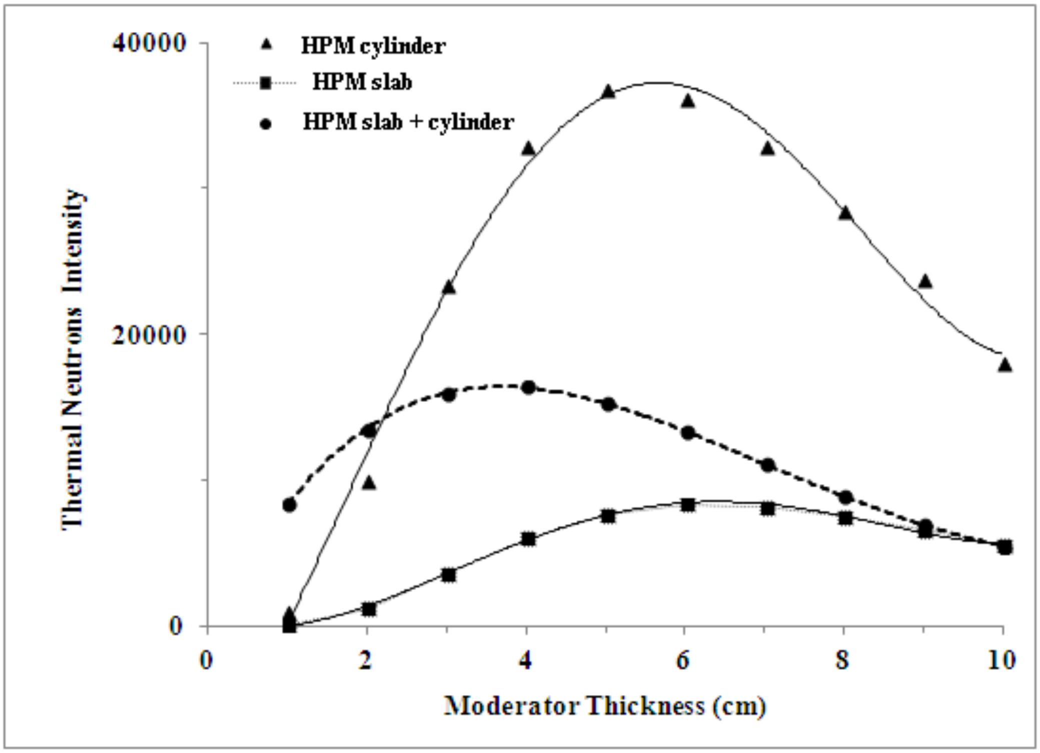

Figure 5.2 Thermal neutron count rate at the sample location from the three geometries plotted as the effective moderator thickness (Results of Monte Carlo Simulations).

Finally, the thermal neutron intensity for the sample enclosed in the HPM cylindrical moderator without the slab (Fig. 5.1(c)) increases initially with cylinder thickness around the sample until it reaches a maximum value for 6 cm thick HPM cylinder. With further increases in thickness of the cylinder, the thermal neutron intensity decreases, a trend similar to the ones observed in Figure 5.1(a and b). The thermal neutron intensity obtained in the design of part(c) was two times higher than the best value achieved from part (a) and (b) designs. Therefore, the design of part (c) was adopted to fabricate the moderator of the 350 keV accelerator based PGNAA set.

Figure 5.3 shows a schematic of the PGNAA setup, built around the 45-degree beam line of the 350 keV accelerator. The PGNAA setup has a cylindrical sample 90 mm in diameter and 145 mm in height, placed in a cavity drilled through the center of cylindrical high density polyethylene moderator with 25 cm diameter and 145 mm height. A cylindrical 100 mm x 100 mm cylindrical gamma-ray detector, with its longitudinal axis aligned along the sample's longitudinal axis detects the prompt gamma rays from the side of the moderator. The moderator is placed adjacent to the accelerator beam line enclosing a deuterium target to moderate the 2.5 MeV neutrons produced by the accelerator. In order to prevent undesired gamma rays and neutrons from reaching the detector, 3 mm thick lead shielding and 50 mm thick neutron shielding are built around the gamma-ray detector. The neutron shielding is made of a mixture of paraffin and lithium carbonate mixed in equal weight proportions.

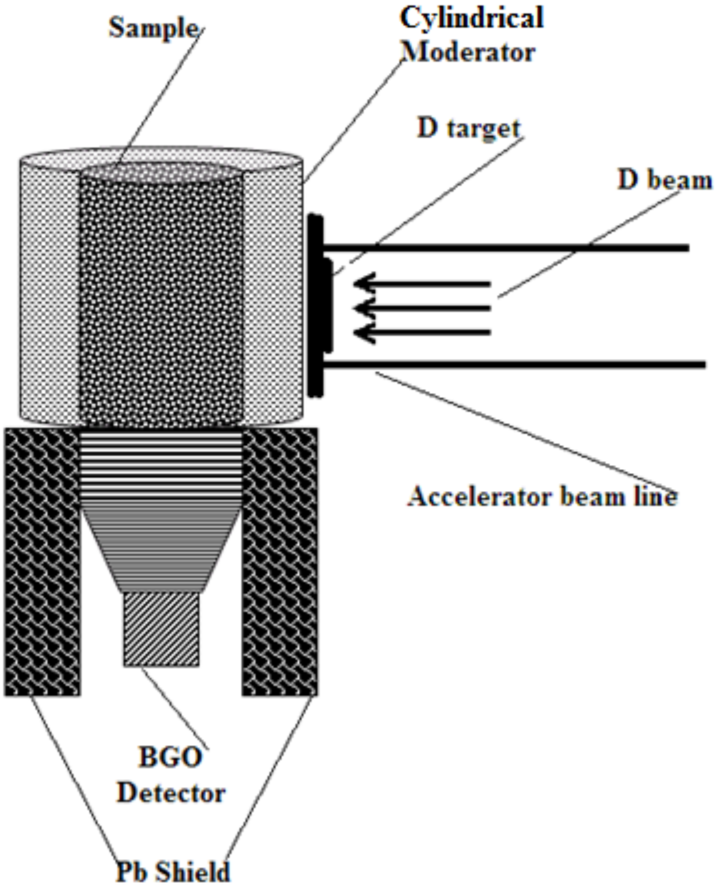

Figure 5.3 Schematic top view of the 350 keV accelerator based PGNAA setup used

In the next step the yield of 2.52, 3.53-3.68, 4.51, 5.27-5.30 and 10.38 MeV prompt gamma-rays of nitrogen was calculated from anthranilic acid, caffeine, melamine, and urea bulk samples inside the detector cell volume with 100 mm by 100 mm (diameter x length) dimension for the optimized geometry of the PGNAA set up shown in Figure 5.3. For simulation study, the moderators, detector, and the sample cells were divided into sub-cells of 1 cm thickness. The yield was integrated in the F4 Tally with ± 10 keV width around the gamma ray energy. The intensities and energies of various nitrogen prompt gamma ray lines due to thermal neutron capture in nitrogen are given in Table 5.2 [23].

Element	**Gamma-ray energy (keV)**	**$\sigma_\gamma^Z(E_\gamma)$-barns**
Bi	162	0.008
	320	**0.0115**
	674	0.0026
	2505	0.0021
	2828	0.00179
	4054	**0.0137**
	4171	**0.0171**
Ge	175	0.164
	493	0.133
	500	0.162
	596	**1.100**
	608	**0.250**
	868	**0.553**
	961	0.129
	1101	0.134
	1204	0.141
	1472	0.083
N	1678	0.0063
	1885	0.0147
	2000	0.0032
	2520	0.0044
	3532	0.0071
	3678	**0.0116**
	4508	**0.0132**
	5269	**0.0236**
	5297	0.0168
	5533	0.0155
	5562	0.0084
	6322	**0.0145**
	7298	0.0075
	8310	0.0033
	10829	**0.0113**

Table 5.2 Energies and partial elemental cross section $\sigma_\gamma^Z(E_\gamma)$-barns of prominent capture gamma-rays of bismuth, germanium and nitrogen [23]

To attain a statistical uncertainty of the order of 1% for prompt gamma-ray calculations about 40 to 45 min were required to calculate the yield of the most intense gamma-rays from the sample. Computation time for thermal neutron yield calculations was half that of the prompt gamma ray yield calculation.

Figure 5.4 shows the calculated yields of 1.68, 2.52, 3.68, 5.28, 6.32 and 10.83 MeV nitrogen gamma rays as a function of nitrogen concentration in anthranilic acid, caffeine, melamine, and urea bulk samples along with the associated least squares fitted lines. The calculated fits were later compared with experimental data.

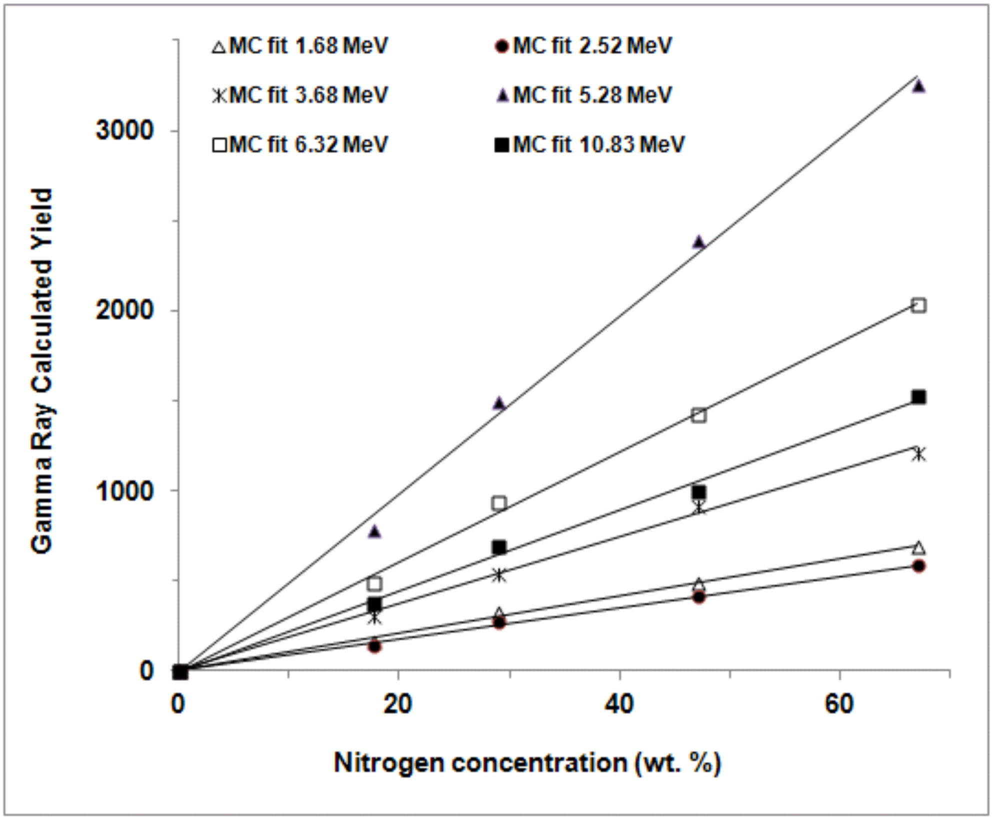

Figure 5.4 Calculated gamma ray yield plotted as a function of nitrogen concentration in anthranilic acid, caffeine, melamine, and urea samples obtained through Monte Carlo simulations

5.2 The 350 keV Accelerator-Based PGNAA Setup

Prompt gamma-ray intensities of nitrogen from anthranilic acid, caffeine, melamine, and urea proxy material samples were measured using the 350 keV accelerator based PGNAA setup shown in Figure 5.3. A pulsed beam of 2.5 MeV neutrons was produced with 110 keV deuteron beam via the D(d,n) reaction. The deuteron beam pulse had a width of 5 milliseconds and a frequency of 250 Hz. The pulsed neutron beam improves the signal to background ratio in the PGNAA studies. A typical beam current of the generator was 70 μA. The nitrogen prompt gamma-ray yield data from the proxy samples were acquired using a 100 mm x 100 mm (diameter x height) BGO detector for 1-1.5 hours period for each sample.

During sample irradiation, the BGO detector although well shielded, was also exposed to thermal neutrons and it registered the prompt gamma-rays due to the capture of thermal neutrons in Bi and Ge present in it. Prompt gamma rays produced due to the interaction of the neutrons in the beam line materials were also detected by the BGO detector. The energies and intensities of prominent prompt gamma-rays due to capture of thermal neutrons in detector and samples material are listed above in Table 5.2 [23].

Figure 5.5 shows a typical BGO detector pulse height background spectrum over 0-13 MeV energy taken with empty plastic bottle exhibiting prompt gamma ray peaks at 2.52 and 4.06-4.26 MeV due to thermal neutron capture in bismuth from BGO detector material and iron and chromium in beam line components. The full energy peaks of Cr at 7.1, 7.9 and 9.7 are quite prominent in Figure 5.5 along with full energy and single escape peaks of the unresolved Fe doublet at 7.63 MeV and 7.65 MeV. In order to show the background level in the region of 10.8 MeV nitrogen peak, the BGO detector background spectrum data shown in Figure 5.5 has been plotted on logarithmic scale in Figure 5.6.

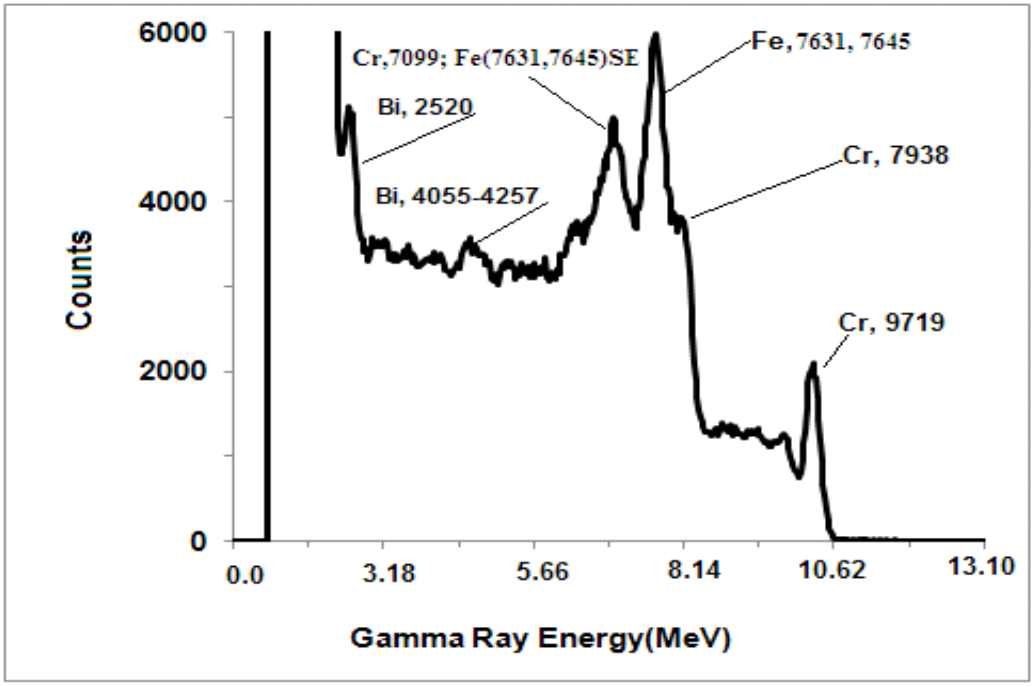

Figure 5.5 BGO detector background gamma ray pulse height spectrum over 0.00-13.1 MeV taken with an empty container showing prompt gamma ray peaks due to thermal neutron capture in detector material and beam line

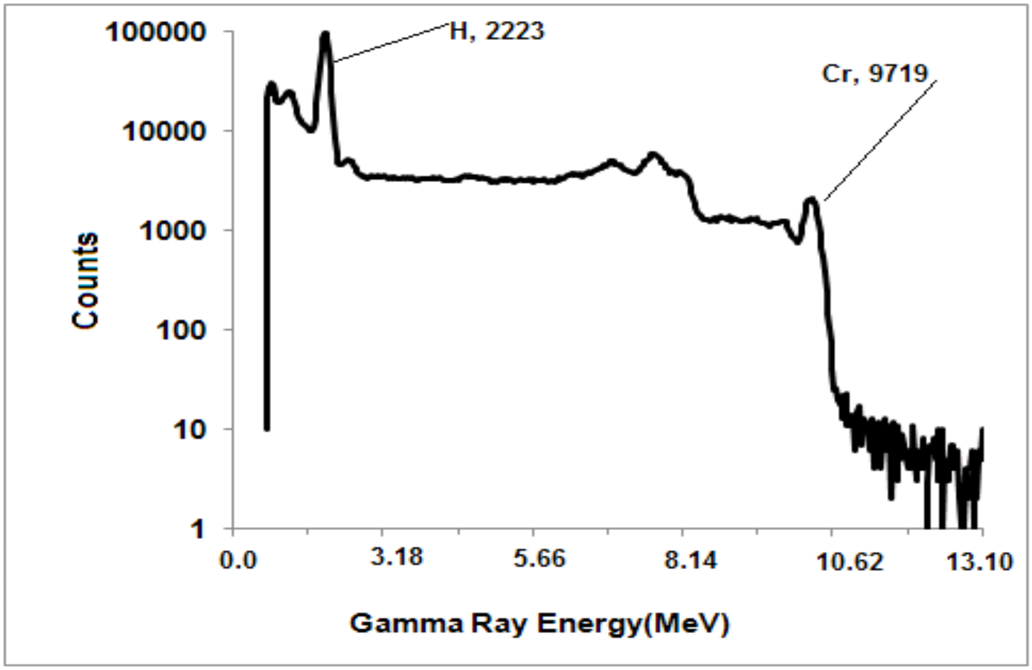

Figure 5.6 BGO detector background gamma ray pulse height spectrum over 0.00-13.1 MeV taken with an empty container plotted on a logarithmic scale to show background around 10.8 MeV energy

Figure 5.7 shows the higher energy part of the BGO detector pulse height spectra from anthranilic acid, caffeine, melamine, and urea samples over 8.63-12.35 MeV along with the background spectrum. Figure 5.7 shows the nitrogen capture peak at 10.8 MeV along with Cr peak at 9.72 MeV. The increasing trend of peak intensity with nitrogen concentration in the sample is very clear showing a maximum peak intensity for melamine and a minimum peak intensity for anthranilic acid, as expected from data shown in Table 5.1. Figure 5.8 shows BGO detector pulse height spectra of melamine, urea, caffeine and anthranilic acid samples over 2.43-8.01 MeV showing nitrogen capture peaks at 2.52, 3.53-3.68, 4.51 and 5.27-5.30 MeV. The nitrogen peak intensities increase with increasing nitrogen concentration, as observed in Figure 5.7.

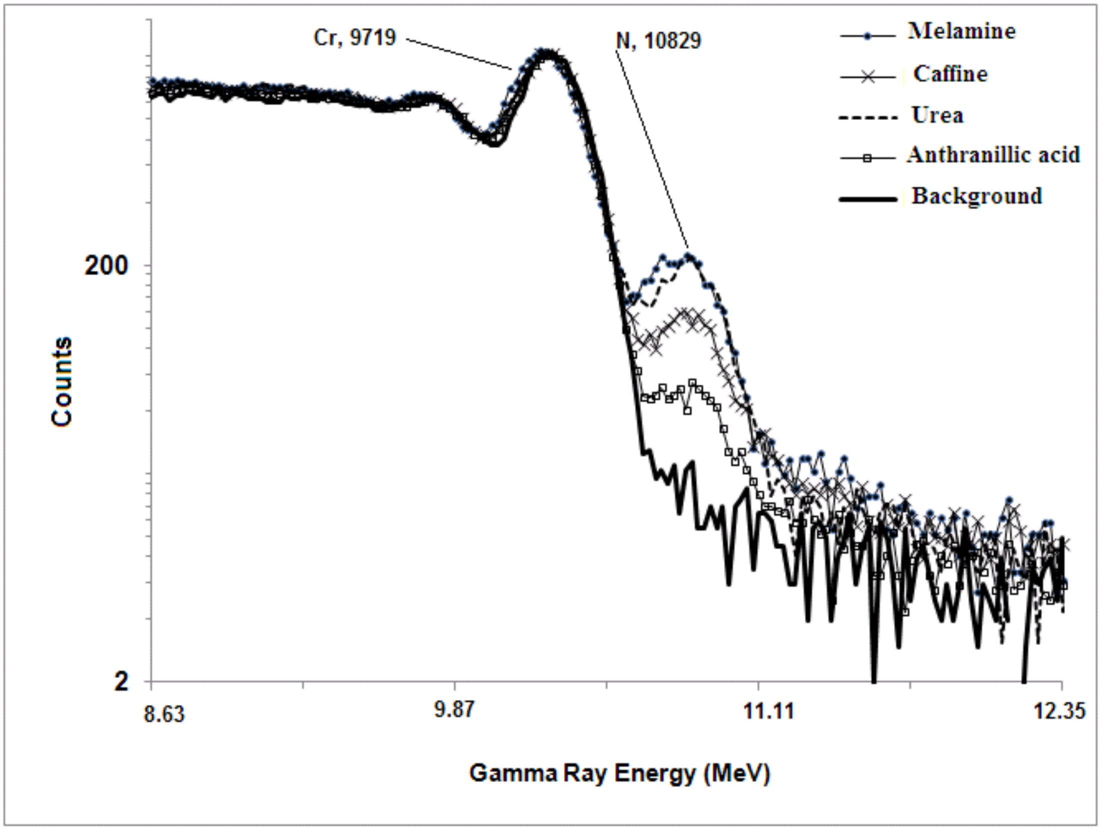

Figure 5.7 Prompt gamma-ray pulse height spectra of BGO detector from anthranilic acid, caffeine, melamine, and urea samples over 8.63-12.35 MeV showing nitrogen 10.83 MeV peak along with chromium background peak.

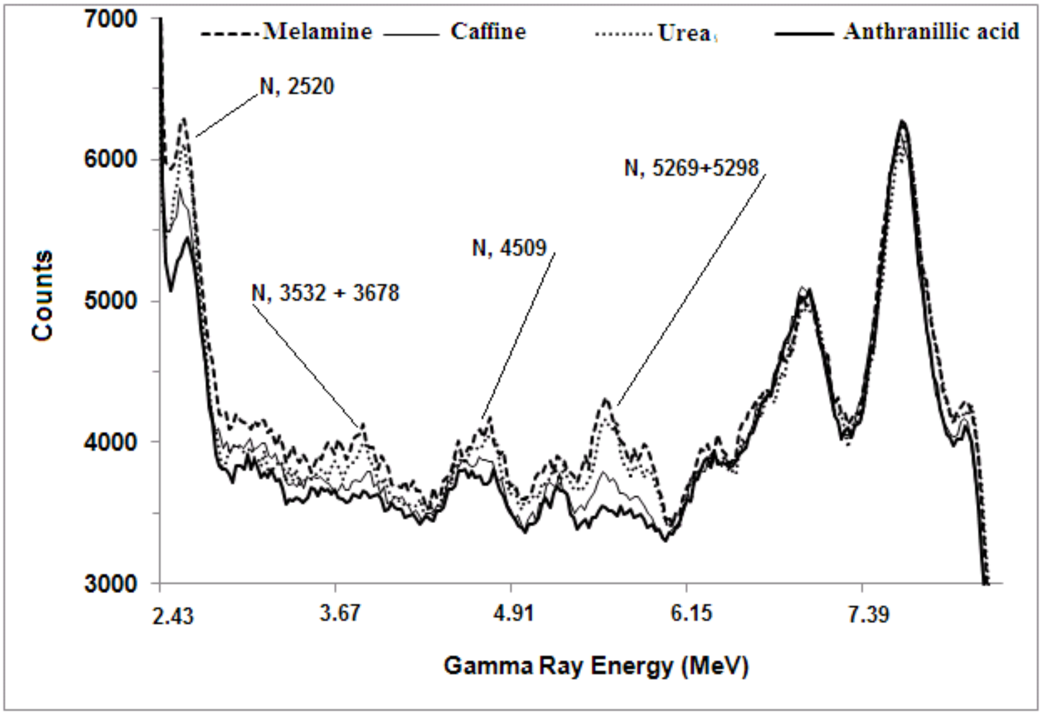

Figure 5.8 Prompt gamma-ray pulse height spectra of BGO detector from anthranilic acid, caffeine, melamine, and urea samples over 2.43-8.01 MeV showing nitrogen capture peaks at 2.52, 3.53-3.68, 4.51 and 5.27-5.30 MeV.

Finally, the background pulse height spectra were subtracted from the samples pulse height spectra and the area under the nitrogen peaks from anthranilic acid, caffeine, melamine, and urea samples were integrated and normalized to the same number of neutrons incident on the sample and background samples. The integrated yields of 2.52, 3.53-3.68, 4.51 and 5.27-5.30 MeV prompt gamma rays peak of nitrogen have been plotted as a function of nitrogen concentration in Figure 5.9. The solid lines in Figure 5.9 represents fits obtained from Monte Carlo calculations. The integrated yield of nitrogen capture peak at 10.8 MeV has been plotted as a function of nitrogen concentration in Figure 5.10 along with a solid line fit obtained from Monte Carlo calculations. There is an excellent agreement between the theoretical yield and the experimental yield of nitrogen prompt gamma rays measured from anthranilic acid, caffeine, melamine, and urea bulk samples using a 350 keV accelerator based PGNAA setup utilizing a 100 mm x 100 mm (diameter x height) BGO detector.

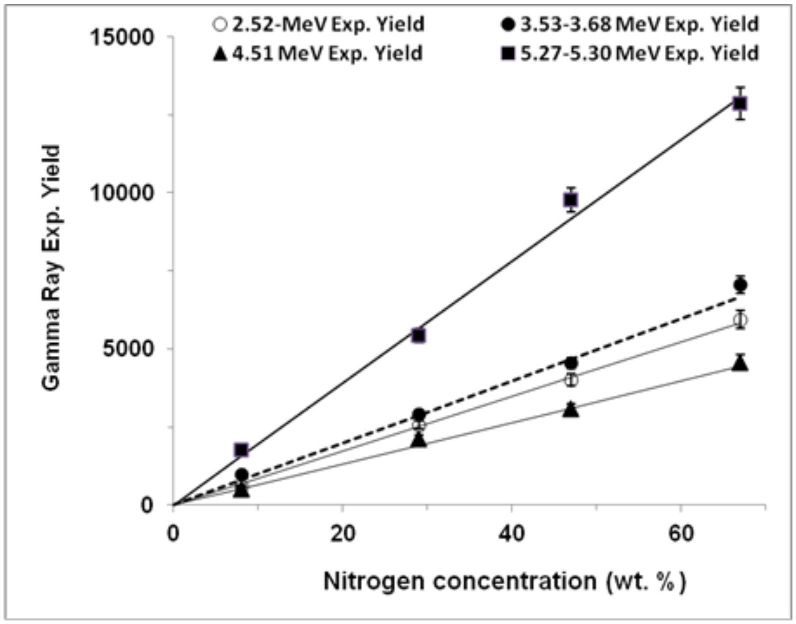

Figure 5.9 Integrated experimental yields of 2.52, 3.53-3.68, 4.51 and 5.27-5.30 MeV prompt gamma-rays from nitrogen plotted as a function of nitrogen concentration. Lines represent results of Monte Carlo simulations.

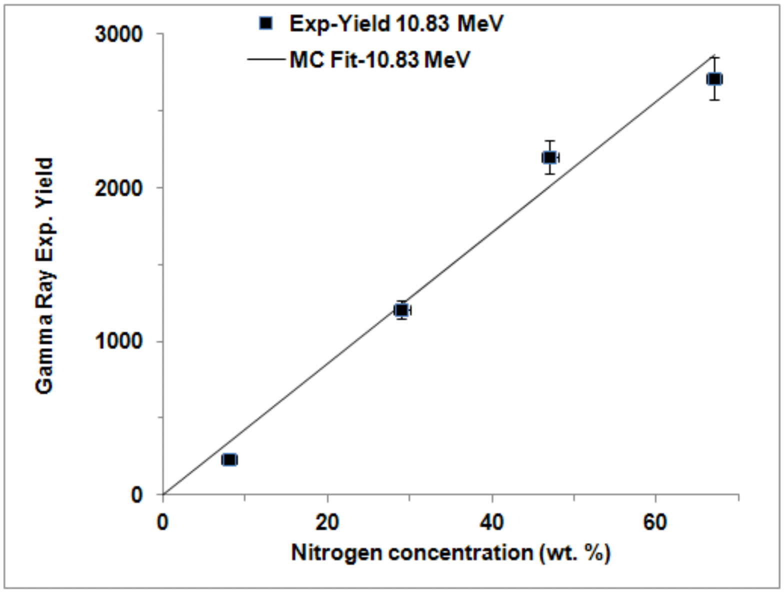

Figure 5.10 Integrated experimental yields of 10.83 MeV prompt gamma-rays from nitrogen plotted as a function of nitrogen concentration. Line represents results of Monte Carlo simulations

5.3 The MP320 Portable Neutron Generator Based PGNAA

In this study nitrogen has been detected in bulk samples via (TNC) using the MP320 portable neutron generator-based PGNAA setup that was described earlier in section 5.1 but with MP320 portable neutron generator instead of 350 keV accelerator. Thermal neutrons were produced by moderating 2.5 MeV fast neutrons from the portable neutron generator using the high density polyethylene moderators. The study has been carried out first time about use of a D-D portable neutron generator in detection of nitrogen in bulk samples.

Melamine, caffeine, urea, and disperse orange samples were irradiated in the MP320 generator-based PGNAA setup as shown in Figure 5.3 (but with the portable generator instead of the 350 keV accelerator). Pulsed 2.5 MeV neutrons were produced with 70 keV pulsed deuteron beam. The portable neutron generator was operated with a pulsed deuteron beam with 5 milliseconds pulse width and 250 Hz frequency. The pulsed beam improves the signal-to-background ratio in the PGNAA studies. The generator was operated at 70 μA deuteron beam current. The nitrogen prompt gamma ray yield data from the samples were acquired using 100 mm × 100 mm (diameter × height) bismuth germinate (BGO) detector for a period of 3 to 4 hours per sample. The BGO detector was chosen because it contains bismuth, which has smaller capture cross-section for thermal neutrons as compared to $LaBr_3$:Ce and $LaCl_3$:Ce detectors.

During sample irradiation, the BGO detector, although well shielded, was also exposed to thermal neutrons and registered the prompt gamma rays due to the capture of thermal neutrons in bismuth (Bi) and germanium (Ge) present in it. The energies and intensities of prominent prompt gamma rays due to capture of thermal neutrons in detector and samples materials are listed in Table 5.2 [23]. Figure 5.11 shows the pulse height spectra of the BGO detector from caffeine sample.

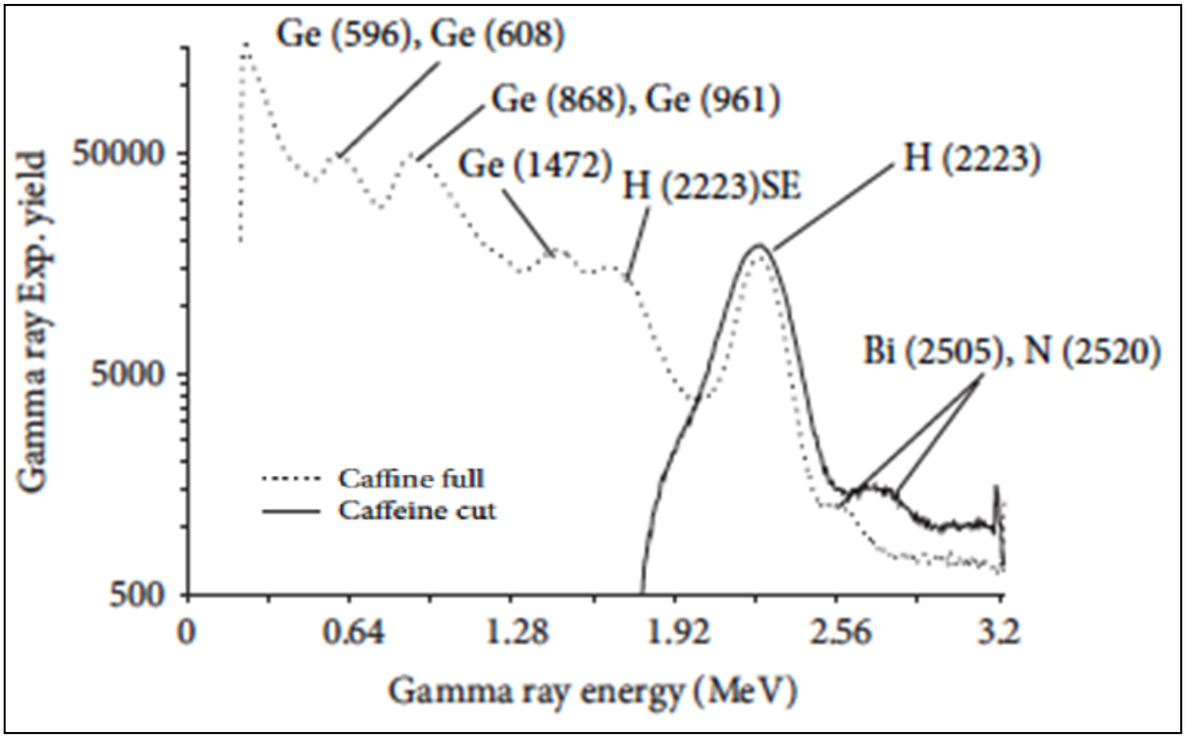

Figure 5.11 Prompt gamma ray experimental pulse height spectra from caffeine sample over 0–3.22 MeV taken with the BGO detector. Also superimposed is pulse height spectrum with lower energy part suppressed from caffeine sample.

In this study, gamma ray spectra with energies less than 3.2 MeV energy were acquired. Nitrogen gamma rays with higher energies were not analyzed in this study because they were interfering with prompt gamma rays from the detector material. Moreover, higher energies gamma rays had very poor statistics because the photo absorption cross-section of gamma rays above 3 MeV energy decreases drastically due to competing Compton scattering and pair production processes. This reduces the detection probability of high energy gamma rays above 3 MeV. Although the intensity of 10 MeV nitrogen line is 2.6

times higher than the 2.52 MeV line, the photoelectric cross-section however drops by a factor of 300 from 2 to 10 MeV. This results in net reduction in detection efficiency of 10 MeV gamma rays using the BGO detector.

Figure 5.11 shows BGO detector pulse height spectrum for caffeine sample over 0–3.22 MeV containing the 2.22 MeV hydrogen capture peak from the moderator material and associated single escape (SE) peak. Figure 5.11 also shows prompt gamma ray peaks at 596, 608, 868, 961, and 1472 keV due to thermal neutron capture in germanium present in BGO detector material. Also shown in Figure 5.11 are unresolved prompt gamma ray peaks from bismuth in BGO detector material and nitrogen in caffeine at 2.50 MeV and 2.52 MeV, respectively. Since the production cross-section of 2.52 MeV nitrogen gamma rays is two times higher than that of 2.50 MeV gamma ray from bismuth, the nitrogen peak is still measureable for samples containing nitrogen in quantities comparable with bismuth contents of the BGO detector. The nitrogen prompt gamma ray peak was located at the higher energy end of the pulse height spectrum. The count rate in the lower energy part of the spectrum was high and it suppressed to minimize detector dead time. The lower energy part of the pulse height spectrum was suppressed (offset) using standard NIM as shown in Figure 5.12.

For data analysis purposes, each pulse height spectrum was converted into an excel spectrum for later subtraction and peak integration. Also shown in Figure 5.11 is a caffeine sample pulse height spectrum with solid line with the lower energy part of the spectrum suppressed. In order to resolve the bismuth-nitrogen peaks from hydrogen 2.22 MeV peak, the detector operating voltage was raised by 50 volts above its optimum operating voltage. Due to this effect, the hydrogen peak shown as a solid line is broader than the peak shown as a dotted line and the bismuth-nitrogen peaks are also more resolved from the hydrogen 2.22 MeV peak than in the dotted line spectrum.

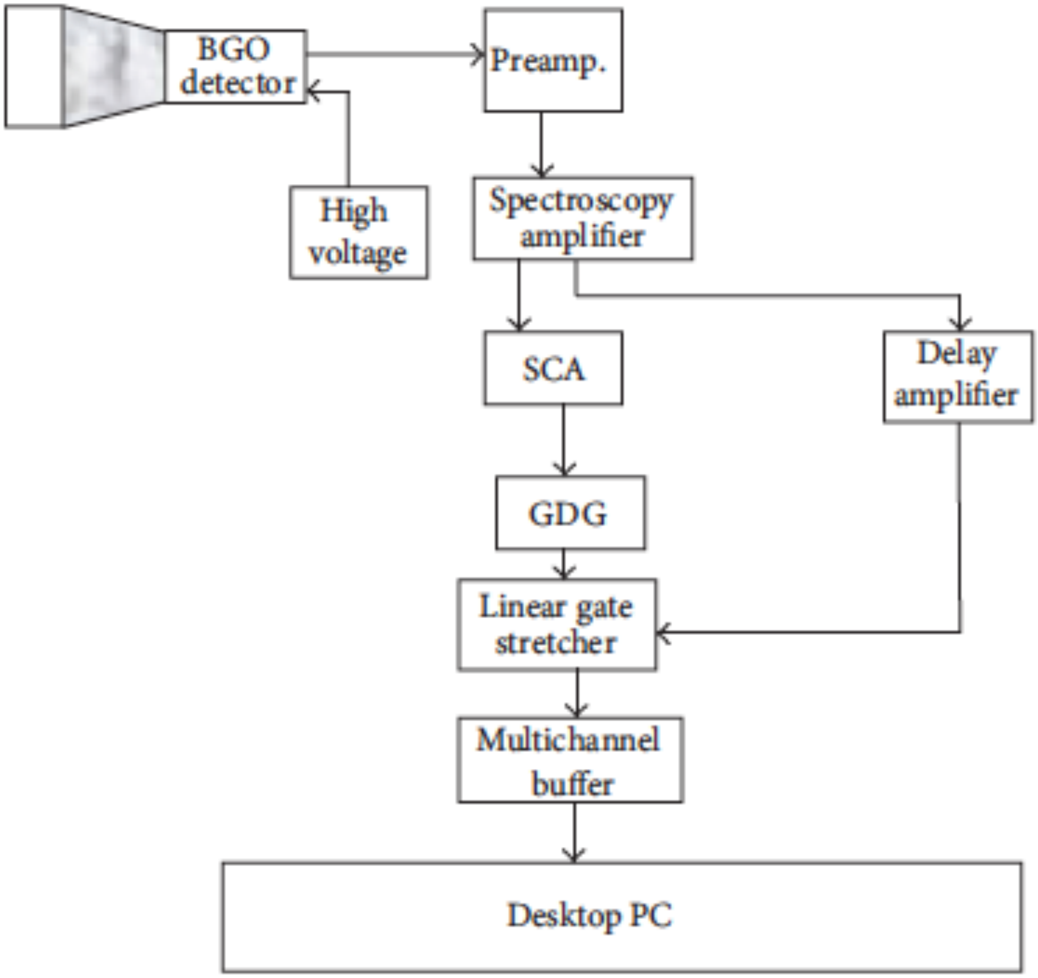

Figure 5.12 Electronics block diagram used to suppress the lower energy part of the BGO detector spectrum.

Figure 5.13 shows (lower energy suppressed) pulse height spectra of melamine, urea, and caffeine samples over 1.76 – 2.81 MeV showing the hydrogen capture peak at 2.22 MeV along with unresolved prompt gamma ray peaks from bismuth and nitrogen at 2.50 and 2.52 MeV, respectively.

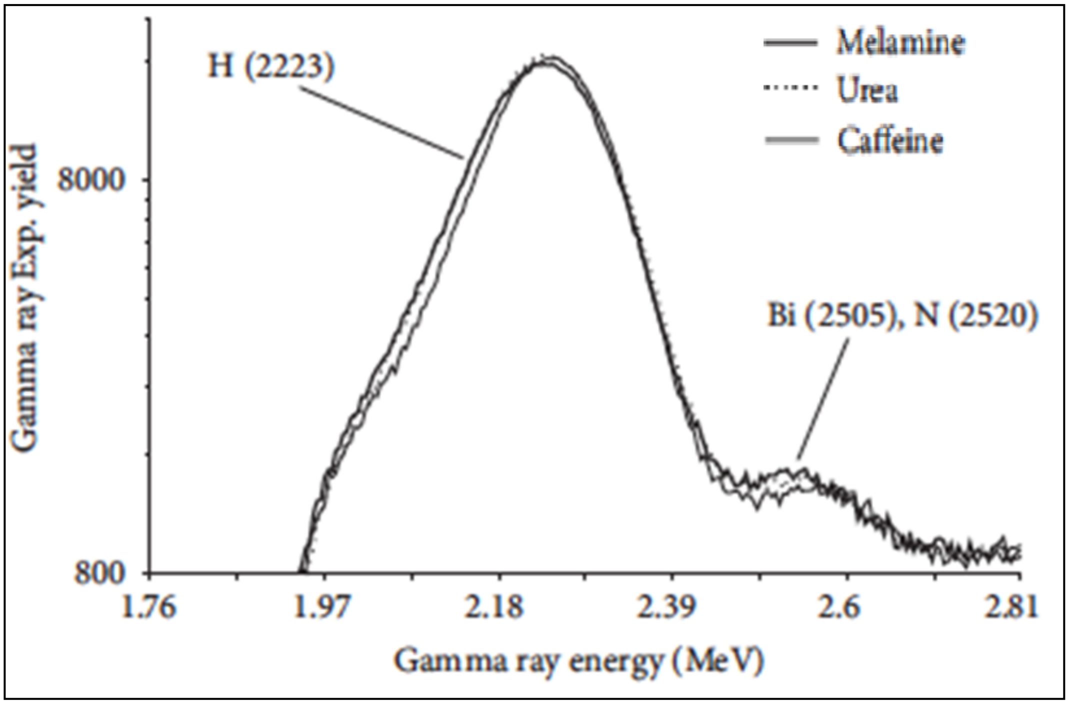

Figure 5.13 Enlarged (lower energy suppressed) prompt gamma ray experimental pulse height spectra of BGO detector from caffeine, melamine, and urea samples over 1.76–2.81MeV showing hydrogen capture peak along with the unresolved 2.50 and 2.52MeV bismuth and nitrogen peaks, respectively.

Figure 5.14 shows enlarged portion of Figure 5.13 over 2.39–2.84 MeV showing unresolved prompt gamma ray peaks from bismuth and nitrogen in melamine, urea, caffeine, and disperse orange superimposed upon background spectrum. Since all samples have different matrices material, it was difficult to find a common background sample material.

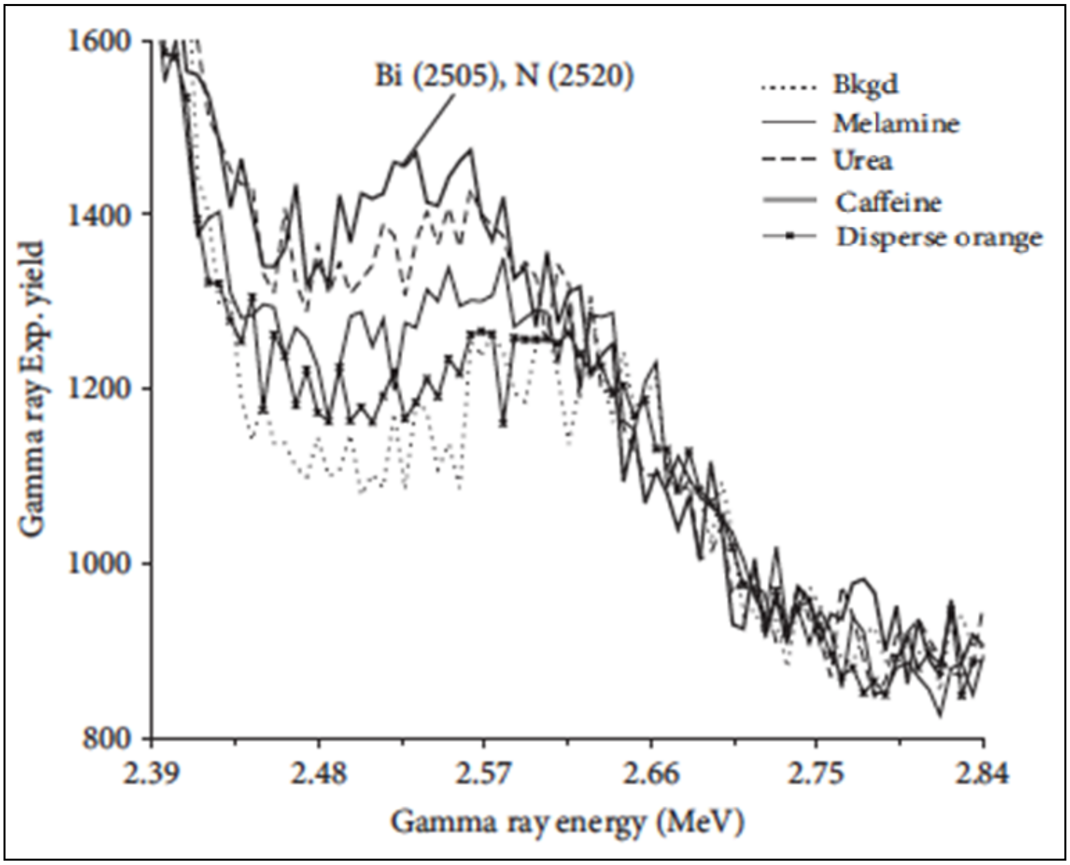

Figure 5.14 Enlarged unresolved 2.50 and 2.52 MeV bismuth and nitrogen prompt gamma ray experimental pulse height spectra of BGO detector from caffeine, disperse orange, melamine, and urea samples over 2.39–2.84MeV.

Therefore, the background spectrum was taken with the empty plastic container. Furthermore, water or polyethylene background samples are not suitable in this case because hydrogen contents of water or polyethylene background samples are higher than those of the actual samples and the resulting background level around 2223 keV hydrogen capture peak in the background sample will be higher than in the actual spectrum. This will therefore suppress the sample effects in the background subtracted spectra. The nitrogen peaks have increasing trends depending upon their nitrogen concentration.

The lowest nitrogen peak intensity has been measured for disperse orange with 17.6 wt.% nitrogen and the highest nitrogen peak intensity has been observed for melamine with 66.7 wt.% nitrogen concentration, as expected from data shown in Table 5.1. Finally, the area under the normalized nitrogen peaks of melamine, urea, caffeine, and disperse orange samples was integrated and background was subtracted. The integrated yield of 2.52 MeV prompt gamma rays peak of nitrogen as a function of nitrogen concentration is plotted in Figure 5.15. The solid line in Figure 5.15 represents the calculated yield of prompt gamma rays obtained from Monte Carlo calculations following the procedure described in [28, 43].

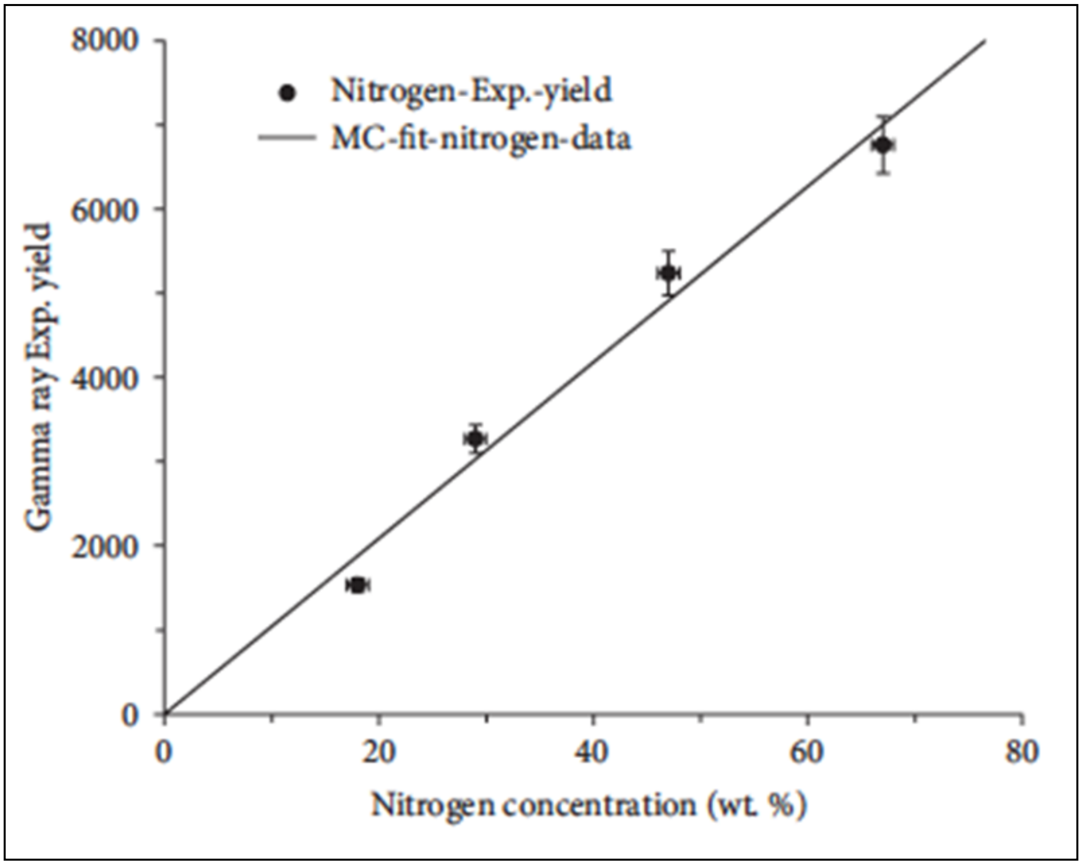

Figure 5.15 Experimental integrated yields of 2.52MeV prompt gamma rays from nitrogen plotted as a function of nitrogen concentration in caffeine, disperse orange, melamine, and urea samples. The solid line represents the results of Monte Carlo simulations.

There is an excellent agreement between the theoretical yield and the experimental yield of nitrogen prompt gamma rays measured from melamine, urea, caffeine and disperse orange bulk samples using a portable neutron generator-based PGNAA setup utilizing a 100 mm × 100 mm (diameter × height) BGO detector.

Minimum detectable concentration of nitrogen in bulk samples

Finally, the minimum detectable concentration of nitrogen in proxy material samples (MDC) was calculated for the portable neutron-based PGNAA setup using equations (3.3) & (3.4) described earlier in section 3.3.1.

The MDC of nitrogen in proxy material samples for the MP320 portable neutron generator was calculated to be 8.2 ± 2.5 wt%. In spite of the low thermal neutron flux of the portable neutron generator and the low thermal capture cross section of nitrogen; the MDC for nitrogen is reasonable. The study has provided useful data for application of a portable D-D neutron generator in detection of nitrogen in bulk material samples.

CHAPTER 6

CONCLUSION

In this study, Prompt Gamma Neutron Activation Analysis (PGNAA) technique was used to measure Nitrogen (N), Carbon (C), Oxygen (O) and Hydrogen (H) elements concentration in bulk samples. Carbon (C) and Oxygen (O) were determined through prompt gamma rays excited in neutron inelastic reactions (NIS) while nitrogen was determined through thermal neutron capture (TNC). NIS- and TNC-based PGNAA setups were designed utilizing 14 MeV and 2.5 MeV neutron beams respectively. The optimum design of the setups was obtained using Monte Carlo simulations. For both setups different gamma ray detectors ($LaBr_3$:Ce, $LaCl_3$:Ce and BGO) were tested for gamma ray detection. The calibration of the NIS and TNC based PGNAA setups were carried out using calibration samples with known elemental composition.

NIS based PGNAA setup was built around zero-degree degree beam line of the KFUPM 350 keV accelerator. 14 MeV neutrons were produced via T(d,n) reaction. 4.4 and 6.1 MeV Prompt gamma ray from carbon and oxygen from benzene, water, ethanol, propanol…etc, calibration sample were detected using $LaBr_3$:Ce and $LaCl_3$:Ce detectors. Due to the interference of chlorine gamma rays and oxygen gamma ray, $LaCl_3$:Ce detector was not used in oxygen measurements. Therefore, $LaBr_3$:Ce detector was used to measure C and O from proxy material of explosives and narcotics (caffeine, urea, anthranillic acid, melamine..etc.). Good agreement was achieved between the experimental results and results of Monte Carlo simulation.

Nitrogen in bulk samples was determined using thermal neutron capture (TNC)-based PGNAA setup built around 45-degree beam line of the KFUPM 350 keV accelerator. 2.5 MeV neutrons were produced via D(d,n) reaction. High-density polyethylene cylindrical moderator was used to thermalize 2.5 MeV neutrons prior to its capture in bulk samples. The sample was placed in a cavity drilled through the center of the moderator. Nitrogen prompt gamma rays from proxy material of explosives and narcotics (caffeine, urea, anthranillic acid, melamine..etc.) were detected using BGO detector. Good agreement was achieved between the experimental results and results of Monte Carlo simulation.

Moreover, nitrogen concentration in bulk samples was also measured using a thermal neutron capture (TNC)-based PGNAA setup built around the KFUPM portable neutron generator model MP320. 2.5 MeV neutrons were produced via D(d,n) reaction. High-density polyethylene cylindrical moderator was used to thermalize 2.5 MeV neutrons prior to its capture in bulk samples. The sample was placed in a cavity drilled through the canter of the moderator. Nitrogen prompt gamma rays from proxy material of explosives and narcotics (caffeine, urea, anthranillic acid, melamine..etc.) were detected using BGO detector. Good agreement was achieved between the experimental results and result of Monte Carlo simulation. A patent application has been filed in US patent office for this portable neutron generator-based PGNAA setup.

REFERENCES

[1] Csikai, J., 1987. "CRC Handbook of Fast Neutron Generators", Vol.I and II.CRC Press, Boca Raton, Florida.

[2] Hussein, E.M.A., 2003. "Handbook on Radiation Probing, Gauging, Imaging and Analysis", Vols.I and II.Kluwer Academic Publishers, Dordrecht.

[3] Seabury E. H. and A. J. Caffery, "Explosive Detection and Identification by PGNAA". Report # INL/EXT-06-01210 (April-2006). *Idaho National Laboratory*, Idaho Falls, Idaho 83415, USA.

[4] Naqvi, A. A., Zameer Kalakada, **Faris A. Al-Matouq**, M. Maslehuddin and O.S.B. Al-Amoudi. "Prompt Gamma-Ray Analysis of Chlorine in Superpozz Cement Concrete". *Nuclear Inst. and Methods in Physics Research*, A Vol. 693 (November 2012), pp. 67-73

[5] Naqvi, A. A., Zameer Kalakada, **Faris A. Al-Matouq**, M. Maslehuddin and O.S.B. Al-Amoudi. "Chlorine Detection in Fly Ash Concrete using a Portable Neutron Generator". *Applied Radiation and Isotopes* Vol. 70 (2012) pp.1671-4.

[6] Buffler, "A Contraband detection with fast neutrons"; *Radiation Physics And Chemistry,* Vol. 71(2004) pp.853-861

[7] Lee, W.C., Mahood, D.B., Ryge, P., Shea, P. and Gozani, T., 1995. "Thermal neutron analysis (TNA) explosive detection based on electronic neutron generators".*Nucl.Instrum. Methods B* 99, pp. 739–742.

[8] Brown, D.R., Gozani, T., Loveman, R., Bendahan, J., Ryge, P., Stevenson, J., Liu, F. and Sivakumar, M., 1994. "Application of pulsed fast neutrons analysis to cargo inspection".*Nucl.Instrum.Methods. A* 353, pp. 684–688.

[9] Overley, J.C., 1995. "Explosives detection through fast-neutron time-of-flight attenuation measurements". *Nucl.Instrum. Methods B* 99, pp. 728–732.

[10] Overley, J.C., Chmelik, M.S., Rasmussen, R.J., Sieger, G.E., Schofield, R.M.S. and Lefevre, H.W., 1997. "Results of tests for explosives in luggage from fast-neutron time-of-flight transmission measurements". *Proc. Int. Soc. Opt. Eng.* 2867, pp. 219–222.

[11] Buffler, A., Brooks, F.D., Allie, M.S., Bharuth-Ram, K. and Nchodu, M.R., 2001. “Material classification by fast neutron scattering analysis”. *Nucl.Instrum. Methods B* 173/4, pp. 483–502

[12] Gozani, T., 2003. “The role of neutron based inspection techniques in the post 9/11/01 era”. *Nucl.Instrum. Methods B* 213, pp. 460–463.

[13] Julie C. Patrick, Grazyna E. Orzechowska, and Edward J. Poziomek; “Use of methylene blue as a simulant for the physical properties of cocaine HCl and heroin HCl”, *Proc. SPIE*, Vol. 2937, 258 (1997)

[14] Harding, G., 2004, “Explosives detection with X-ray scatter tomography”. *Radiation Phys. Chem*., Vol. 71(2004) pp. 750-756

[15] Appleby, R. Wallace, HB; “Standoff detection of weapons and contraband in the 100 GHz to 1 THz region”. *IEEE Transactions On Antennas And Propagation* Vol. 55 (2007) pp**.** 2944-2956

[16] Volkov, L.V., Voronko, A. I., Volkova, NL, et al.; “Active MMW Imaging technique for contraband detection” *33RD European Microwave Conference, Vols 1-3, Conference Proceedings* (2004) pp. 531-534.

[17] Newman, DE; Barrall, GA; “Detection of contraband in pelvic body cavities”. *Applied Magnetic Resonance*, Volume: 25, Issue: 3-4, Pages: 577-584, Published: 2004

[18] D.C. Seward, “Explosive detection using dielectrometry”, *Proceedings of the First International Symposium on Explosive Detection Technology*, 1991, pp. 441-443

[19] Hee-Jung Ima, Hyun-Je Chob, Byoung Chul Songa, Yong Joon Parka, Yong-Sam Chungc, Won-Ho Kima, Analytical capability of an explosives detection by a prompt gamma-ray neutron activation analysis, *Nucl.Instrum.Methods. A* 566 (2006) pp. 442‑447

[20] http://nmi3.eu/neutron-research/techniques-for-/chemical-analysis.html

[21] http://www.thermoscientific.com/ecomm/servlet/productsdetail_11152_L10611_82242_11962780_-1

[22] Briesmeister J. F. (Ed). 1997. “MCNP4B2 –A General Monte Carlo N-Particles Transport Code”. *Los Alamos National Laboratory Report* LA-12625-M, Version 4A.

[23] Choi H.D., Firestone R.B., Lindstrom R.M., Molnar G.L., Mughabghab S.F., Paviotti-Corcuera R., Revay Zs., Trkov A. and Zhou C.M., 2006. “Database of Prompt Gamma-Rays from Slow Neutron Capture for Elemental Analysis”. Compiled by. *International Atomic Energy Agency*, VIENNA.

[24] Naqvi A. A., Maslehuddin M., Garwan M. A., Nagadi M. M., Al-Amoudi O.S. B., Raashid M., and Khateeb-ur-Rehman, 2010. “Effect of Silica Fume Addition on the PGNAA Measurement of Chlorine in Concrete”. *Applied Radiation Isotopes*, 68, 412-417.

[25] Naqvi A.A., Maslehuddin M., Garwan M.A., Nagadi M.M., Al-Amoudi O.S.B., Khateeb ur-Rehman and Raashid M., 2011. “Estimation of minimum detectable concentration of chlorine in the blast furnace slag cement concrete”. *Nuclear Instruments and Methods in Physics Research B*, 269, 1–6.

[26] Vincke H., Gschwendtner E., Fabjan C.W. and Otto T., 2002. “Response of a BGO detector to photon and neutron sources: simulations and measurements”. *Nuclear Instruments and Methods in Physics Research A,* 484, 102–110.

[27] A.A. Naqvi, M.S. Al-Anezi, Zameer Kalakada, A.A. Isab, M.Raashid, Khateeb-ur-Rehman, F.Z. Khiari, M.A. Garwan, O.S.B. Al-Amoudi, M. Maslehuddin. “Detection efficiency of low levels of boron and cadmium with a LaBr3:Ce scintillation detector”. *Nuclear Instruments and Methods in Physics Research, section A* 665 (2011) 74-79.

[28] A.A. Naqvi, Zameer Kalakada, M.S. Al-Anezi, **Faris. A. Al-Matouq**, M.Raashid, Khateeb-ur-Rehman, M. Maslehuddin. “Response tests of a $LaCl_3$:Ce scintillation detector with Low energy prompt Gamma Rays from Boron and Cadmium”. *Applied Radiation and Isotopes* 70 (2012) 882–887

[29] Gerhart C. Lowenthal,P. L. Airey. “Practical applications of radioactivity and nuclear radiations an introductory text for engineers, scientists, teachers and students”. *Cambridge university press*, 2001.

[30] D. Alexiev, L. Mo, D.A. Prokopovich, M.L. Smith, M. Matuchova, IEEE Transactions on Nuclear Sciences NS55 (3) (2008) 1174.

[31] A.A. Naqvi, M. Maslehuddin, M.A. Garwan, M.M. Nagadi, O.S.B. Al-Amoudi, M. Khateeb-ur-Rehman, Nuclear Instruments and Methods in Physics Research B 269 (2011) 1.

[32] Gedcke D.A., 2001. “How counting statistics controls detection limits and peak precession”. In: ORTEC Application Notes AN59. Website: /www.ortec-online.com.

[33] Z. Idiri, H. Mazrou, A. Amokrane, S. Bedek, Section B: "Beam Interactions with Materials and Atoms" 268 (2010) 213.

[34] Aksoy, A. A. Naqvi, F.Z. Khiari, M. Raashid, A. Coban, R.E. Abdel-Aal and H. Al-Juwair. (1993) "KFUPM fast neutron activation analysis facility". *Nuclear Instruments and Methods in Physics Research*, Section A: Accelerators, Spectrometers, Detectors and Associated Equipment, Vol. 332, pp. 506

[35] Briesmeister J. F. (Ed), 1997. "MCNP4C –A General Monte Carlo N-Particles Transport Code". *Los Alamos National Laboratory Report*, LA-12625.

[36] M. Balcerzyk, M.Moszyński, M.Kapusta, "Comparison of $LaCl_3$:Ce and NaI(TI) scintillators in gamma-ray spectrometry", *Nuclear Instruments and Methods in Physics Research* A 537 (2005) 50.

[37] A.Owens, A.J.J.Bos, S.Brandenburg, C.Dathy, P.Dorenbos, S.Kraft, R.W. Ostendorf, V. Ouspenski, F. Quarati, "Gamma-ray performance of a 1242 cm^3 $LaCl_3$:Ce scintillation spectrometer", *Nuclear Instruments and Methods in Physics Research* A574 (2007) 110.

[38] K.S. Shah, J. Glodo, M. Klugerman, L. Cirignano, W. W. Moses, S. E. Derenzo, M. J. Weber, "$LaCl_3$:Ce scintillator for gamma-ray detection", *Nuclear Instruments and Methods in Physics Research* A505 (2003) 76.

[39] S. Davorin, S. Pesente, G. Nebbia, G. Viesti, V. Valkovic, "Identification of materials hidden inside a container by using the 14 MeV tagged neutron beam", *Nuclear Instruments and Methods in Physics Research* B 261 (2007) 321.

[40] C. Eleon, B. Perot, C. Carasco, D. Sudac, J. Obhodas, V. Valkovic, "Experimental and MCNP simulated gamma-ray spectra for the UNCOSS neutron-based explosive detector", *Nuclear Instruments and Methods in Physics Research* A 629 (2011) 220.

[41] M. Ciema, D. Balabanski, M. Csatlo, J. M. Daugas, G. Georgiev, J. Gulya, M. Kmiecik, A. Krasznahorkay, S. Lalkovski, A. Lefebvre-Schuhl, R.Lozeva, A.Maj, A.Vitez, "Measurements of high-energy gamma-rays with $LaBr_3$:Ce detectors", *Nuclear Instruments and Methods in Physics Research* A 608 (2009) 76.

[42] A. Favalli, H. C Mehner, V. Ciriello, B. Pedersen, "Investigation of the PGNAA using the $LaBr_3$ scintillation detector", *Applied Radiation and Isotopes* 68 (2010) 901.

[43] A. A Naqvi, **Faris A. Al-Matouq**, F. Z. Khiari, A. A. Isab, Khateeb-ur-Rehman, M. Raashid, "Prompt gamma tests of LaBr3:Ce and BGO detectors for detection

of hydrogen, carbon and oxygen in bulk samples", *Nuclear Instruments and Methods in Physics Research* A 684 (2012) 82.

[44] F. C. Engesser, W. E. Thompson, "Gamma Rays Resulting From Interaction of 14.7 MeV Neutrons With Various Elements", *Journal of Nuclear Energy* 21 (1967) 487.

[45] Defense Nuclear Agency Report # DNA 2716 (29 February 1972). "Neutron Scattering and gamma ray production cross sections for N, O, Al, Si, Ca and Fe". *Defense Nuclear Agency*, Washington, D.C. 20305, USA.

[46] Simakov, S.P., Pavlik, A., Vonach, H., Hlavac, S.(1998). "Status of experimental and evaluated discrete gamma-ray production at En = 14.5 MeV". *IAEA Nuclear Data Section*, Final Report of Research Contract 7809/RB.

[47] Farsoni A. Tavakkoli, S. A. Mireshghi. "Design and evaluation of a TNA explosive-detection system to screen carry-on luggage", *Journal of Radio analytical and Nuclear Chemistry*, 248 (2001) 695.

[48] A. A., Naqvi Zameer Kalakada, M.S. Al-Anezi, M. Raashid, Khateeb-ur-Rehman, M. Maslehuddin and M. A. Garwan, "Low Energy Prompt Gamma-Ray Tests of a Large Volume BGO Detector", *Applied Radiation and Isotopes* 70, (2012) 222.

Vitae

Name : Faris Ahmed Al-Matouq

Nationality : Saudi

Date of Birth :12/20/1986

Email : faris@kfupm.edu.sa

Academic Background : B.S. degree in Physics & Geophysics (double major), 2010 (Second Distinguished Honor) from King Fahd University of Petroleum and Minerals.

Publications

Refereed Journals

[1] A.A. Naqvi, **Faris A. Al-Matouq**, F.Z. Khiari, M.A. Gondal, Khateeb-ur Rehman, A.A. Isab, M. Raashid, M.A. Dastageer. “350 keV accelerator based PGNAA setup to detect nitrogen in bulk samples”, Nuclear Instruments and Methods in Physics Research Section A Volume 729, 21 November 2013, Pages 8-13.

[2] Naqvi, A.A, **Al-Matouq, F.A.**, Khiari, F.Z., Isab, A.A., Raashid, M., Khateeb-ur-Rehman. “Hydrogen, carbon and oxygen determination in proxy material samples using a LaBr:Ce detector”, Applied Radiation and Isotopes, Volume 78, August 2013, Pages 145-150

[3] Naqvi A. A**., Faris A. Al-Matouq**, F. Z. Khiari , Khateeb-ur-Rehman , M. A. Gondal and A. A. Isab. “Optimization of a Prompt Gamma Setup for Analysis of Environmental Samples”. Journal of Radioanalytical and Nuclear Chemistry (2013), Vol. 296, pp.215-221.

[4] Naqvi A. A., Zameer Kalakada, M.S. Al-Anezi, **Faris Al-Matouq** , M. Maslehuddin, O.S.B. Al-Amoudi. “Performance Evaluation of a Portable Neutron Generator for Prompt Gamma-ray Application”. The Arabian Journal for Science and Engineering, 10.1007/s13369-013-0880-y

[5] Naqvi, A. A. **Faris A. Al-Matouq**, F.Z. Khiari, Khateeb-ur-Rehman and A. A. Isab. "Sample Dependent Response of a $LaCl_3$:Ce Detector in Prompt Gamma Analysis of Bulk Hydrocarbon Samples"**.** Nuclear Inst. and Methods in Physics Research, A 719 (2013) 39-43.

[6] Naqvi A. A., **Faris A. Al-Matouq**, F. Z. Khiari, Khateeb-ur-Rehman , A. A. Isab and M. Raashid http://dx.doi.org/10.1155/2013/486192. "Nitrogen Detection in Bulk Samples using a Portable Neutron Generator Based PGNAA setup". Journal of Spectroscopy, Volume 2013 (2013), Article ID 486192.

[7] Naqvi A. A., **Faris A. Al-Matouq**, F. Z. Khiari, A. A. Isab. Khateeb-ur-Rehman, M. Raashid. "Prompt gamma tests $LaBr_3$:Ce and BGO detectors for detection of hydrogen, carbon oxygen in bulk samples". Nuclear Inst. and Methods in Physics Research, A 684 (2012) 82-87.

[8] Naqvi, A. A., Zameer Kalakada, **Faris A. Al-Matouq**, M. Maslehuddin and O.S.B. Al-Amoudi. "Prompt Gamma-Ray Analysis of Chlorine in Superpozz Cement Concrete". Nuclear Inst. and Methods in Physics Research, A Vol. 693 (November 2012), pp. 67-73

[9] Naqvi, A. A., Zameer Kalakada, **Faris A. Al-Matouq**, M. Maslehuddin and O.S.B. Al-Amoudi. "Chlorine Detection in Fly Ash Concrete using a Portable Neutron Generator". Applied Radiation and Isotopes Vol 70 (2012) pp.1671-4.

[10] Naqvi A. A., M.S. Al-Anezi, Zameer Kalakada, **Faris A. Al Matouq**, M. Maslehuddin , M. A. Gondal, A. A. Isab, Khateeb-ur-Rehman and M. Dastageer, "Response Tests of a $LaCl_3$:Ce Scintillation Detector With Low Energy Prompt Gamma Rays From Boron and Cadmium". Applied Radiation and Isotopes, Vol.70 (2012) pp. 882-887.

[11] A.A. Naqvi, M.S. Al-Anezi, Zameer Kalakada, **Faris A. Al-Matouq**, et. al.**, "**Detection of low levels of boron and cadimium with $LaBr_3$:Ce scintillation detector", Nuclear instruments and methods in physics research A 665 (2011) 74-79

Conference Publications

[12] Naqvi, A. A., Zameer Kalakada, **Faris A. Al-Matouq**, O.S. B. Al-Amoudi, M. Maslehuddin, M. Raashid and Khateeb-ur-Rehman. "Monitoring of Chloride in Concrete using a Portable Neutron Generator". Presented in Fifth Saudi Science Conference SSC5, held on April 13-15, 2012 at Umm-ul-Qura University, Makah, Saudi Arabia.

[13] Naqvi A. A., **Faris A. Al-Matouq** , Khateeb-ur-Rehman , M. A. Gondal, A. A. Isab , F. Z. Khiari and M. Raashid. "Optimization of a Prompt Gamma Analysis Setup for Analysis of Environmental Samples". Paper log. #167: presented by **Faris A. Al-Matouq** in METHODS

AND APPLICATIONS OF RADIOANALYTICAL CHEMISTRY- IX (MARC IX) held on March 25-30, 2012 at Kailua-Kona, Hawaii, USA.

[14] Naqvi A. A., **Faris A. Al-Matouq**, A. A. Isab , M Raashid , Khateeb-ur-Rehman and F. Z. Khiari. “Carbon and Oxygen detection in Bulk Samples using Prompt Gamma Rays”. Paper log. #169: presented by **Faris A. Al-Matouq** in METHODS AND APPLICATIONS OF RADIOANALYTICAL CHEMISTRY- IX (MARC IX) held on March 25 30, 2012 at Kailua-Kona, Hawaii, USA.

[15] **Faris A. Al-Matouq**, Mohammad S. Alanazi and A. A. Naqvi**, “**Water Salinity Measurement using PGNAA Technique”**.** Presented in Fourth Saudi Science Conference-Contribution of Science Faculties in the Development of KSA March 21-24, 2010 held at Taybah University, Al-Madina, Saudi Arabia